Degree Course in Biomedical Engineering

Master's Degree Thesis

"Development of a 3D finite element model of trabecular bone: quantitative validation against 3D full-field strain measurements"

Internal Tutor

Dr.ssa Mara Terzini

Supervisors

Dr. Lorenzo Grassi

Dr.ssa Anna Gustafsson

Prof.ssa Hanna Isaksson

Candidate

Federica Incatasciato

Academic Year 2021/2022

Ad Alessio,

esempio di amicizia autentica.

A Teresa, mia nonna,

per aver vegliato su di me

durante questa fantastica esperienza in Svezia.

Acknowledgements

These last six months have been a wonderful and amazing journey where I knew a lot of interesting people who became special to me.

The first people I would like to thank are my supervisors Lorenzo Grassi, Anna Gustafsson and Hanna Isaksson. Thank you for having accepted me in the team and for having guided me through all the steps of this project. You supported me constantly with patience and kindness, especially at the beginning when everything was new for me. I have learnt a lot from this thesis project but also working in Biomechanics group, taking part in meetings.

I also would like to thank all the Biomechanics group in Lund: Isabella, Giulia, Gustavo, Hector, Joeri, Elin, Maria, and Tobias. You were very kind and available. You always asked me about my progress showing interest. Especially, I want to offer my sincere thanks to Gustavo who helped me in the last months.

A sincere thanks goes to Giulia, who supported me during the most difficult moments of the project. Your words were very helpful to me even though a bit hard. You gave me hope and force to go on.

I would like to thank my Italian supervisor Mara Terzini for having accepted the proposed thesis request and for supporting and trusting me during the months abroad.

My sincere acknowledgements go to my parents, Aldo and Marinella, for their unwavering support and belief in me and without whom this experience would not have been possible. I would also like to thank my brother, Giuseppe, my grandparents and all my family for always being there.

A super big thanks goes to all my corridor mates in Lund without whom I could not have succeeded in this experience: Eda, Evelyn, Zhu Ye, Sudipta, Clara, Sabrina, Yuxiang and Elham. You were a very important reference point there, you gave me a constant support, you made the so cold Sweden warm and full of love. Thanks to you, I learnt that real friends exist, I learnt that real and authentic love and friendship exist. I will be grateful to you forever.

I would like to thank my Italian friends Bernadette, Giordano and Antonino for supporting me during the months abroad and also Nicole for constantly giving me advice and support to overcome difficulties.

A special thanks goes to three of the most important friends that I have: Saro, Fabio and Alessio.

Saro, you helped me a lot especially in the last months, you supported me, and you always were there to pick me up.

Fabio, you are always there for me even at distance, I shared with you a lot of moments which demonstrated to me that you are a true and reliable friend.

Alessio, I can’t explain so easily how much I am grateful to you, you know. You supported me in the worst moments of this work, even when I felt completely lost and without a solution. You gave me the hope, you let me see the light. I can clearly say that I could not have survived there without your support, without your beautiful soul, always by my side. Thank you from the bottom of my heart.

Abstract

Osteoporosis is the most common chronic metabolic bone disease related to various factors including menopause and aging. Since bone turnover is increased, the metabolic activity changes. These alterations lead to net-loss of bone tissue, with decreased structural connectivity and apparent density, which subsequently results in a weaker structure. Fragility fractures are the clinical outcome of osteoporosis.

Bone mineral density (BMD) measurement or the development of algorithms such as Fracture Risk Assessment Tool Model are two ways to estimate the fracture risk, but their predictive capabilities are still limited. Hence, a more detailed evaluation of pathological risk of fracture is needed.

In the present thesis, I aimed to improve predictions of bone damage and fracture. This was done by the development of a subject-specific microstructural finite element (μFE) model based on high-resolution images from micro-computed tomography (μCT). Moreover, a procedure to validate the model by using experimental measurements from Digital Volume Correlation (DVC) was implemented.

Homogenous, isotropic, and linear elastic μFE model was generated with two different sets of boundary conditions (BCs). DVC experimental measurements at three different levels of resolution were analysed by a procedure based on interpolation and directly compared to predicted values by μFE model.

The implemented method could take the first step towards validating the μFE models. The analysis showed that volumetric strain maps from DVC are more influenced by noise effects than are displacement maps. This influence was more visible at high-resolution level with respect to downscaled data. Comparisons between μFE and DVC showed that strain fields differ significantly between the two methods and that the μFE model can detect only high volumetric strain regions where cracks are about to occur. With regards to the displacement field, μFE model can be accurate in two directions.

The results suggest further development in methods for both the DVC and the μFE model, for instance adding element specific material properties based on BMD values to the model or improving the DVC scanning techniques could represent some possibilities.

List of acronyms & abbreviations

ε – strain

u – displacement

ν - Poisson's ratio

E – Young's modulus

ROI – Region of interest

BC – Boundary condition

BMD – Bone mineral density

CT - Computed tomography

DIC – Digital Image Correlation

DVC – Digital Volume Correlation

DXA – Dual-energy X-ray absorptiometry

FE – Finite element

FEA – Finite element analysis

FEM – Finite element method

FFT – Fast Fourier Transform

FRAX – Fracture Risk Assessment Tool Model

micro-CT – Micro- computed tomography

micro-FE – Microstructural finite element

SR-μCT- Synchrotron radiation micro-Computed Tomography

WHO – World Health Organization

List of Figures & Tables

Contents

Chapter 1

Introduction

Osteoporosis is established and well-defined as the most common chronic metabolic bone disease that affects more than 75 million people in Europe, Japan and USA and causes more than 2.3 million fractures annually in Europe and the USA alone [2].

Fractures are the result of the increased bone fragility, deterioration of bone tissue and disruption of bone microarchitecture due to osteoporosis and may cause chronic pain, disability and death. Especially, hip fractures, which are the most common, are associated with 15-20% increased mortality rate within 1 year followed by a 2.5-fold increased risk of future fractures [3].

Since fractures account for both a decrease in life quality for the people affected but also a major socio-economic effect in terms of big financial burden to health insurance, prevention and prediction of the disease and its associated fractures is needed and essential to decrease its level of severity.

To evaluate pathological risk of fracture one of the most common methods is the areal measurement of BMD or other tools such as FRAX. However, they are not enough to provide an objective and accurate prediction of bone strength [4] because they do not consider individual bone geometry, or path for a fracture etc. In this scenario, FE- models play an important role as a beneficial tool in engineering research since they account for the complex structure and local variations in bone mineral density. In addition, compared with histological methods, the FE method is a non-invasive approach of obtaining the bone strength [5]. At microscale level, μFE models based on high-resolution imaging can resolve bone structural heterogeneities and can be used to better understand bone deformation under complex loading. The accuracy of FE-models has motivated their application to clinical studies of osteoporotic fractures. Nevertheless, such models have demonstrated heterogeneous results which find their explanation in the lack of an uniform strategy with respect to FE modelling of the human femur [5]. At the current state, how to establish a model which is closer to the real situation has been the focus and difficulty of the study of human body's finite element.

Chapter 2

Aim and design of the study

2.1 Aim of the study

The aim of this project is to improve predictions of bone damage and fracture on the microscale by creating a subject-specific micro-FE model based on micro-CT images. Furthermore, the project aims to implement a working method to validate the model using experimental data from Digital Volume Correlation analysis.

2.2 Design of the study

The design of the study is as follows: micro-CT images were obtained from a previous study [1] and used to develop a subject-specific 3D-Finite element model for a sub-volume isolated from a cylindrical trabecular bone plug of human femoral head. In the mentioned work [1], bone plugs were compressed in displacement control, with steps until failure to investigate strain distribution and its evolution during loading. Hence, boundary conditions were obtained from the experimental study and applied to the computational model. The subject-specific finite element model was used to predict displacement and strain distributions in the trabecular bone before and at failure. The results were compared to the experimental data [1].

Figure 2.1. Design of the study

Chapter 3

Background

This section is briefly reviewing the topics constituting the basis of this thesis.

3.1 Trabecular bone

Trabecular bone tissue is a highly porous, heterogeneous, and anisotropic material found at the epiphyses of long bones and within flat and irregular bones such as sternum, pelvis, and spine. At the macro scale trabecular bone is composed of trabecular struts and plates differently oriented to form a stiff and ductile structure of soft intertrabecular spaces where blood vessels and bone marrow are. At microscale, trabecular architecture is organized to optimize load transfer: trabeculae are aligned towards the mechanical load distribution that a bone experiences within long bones such as the femur.

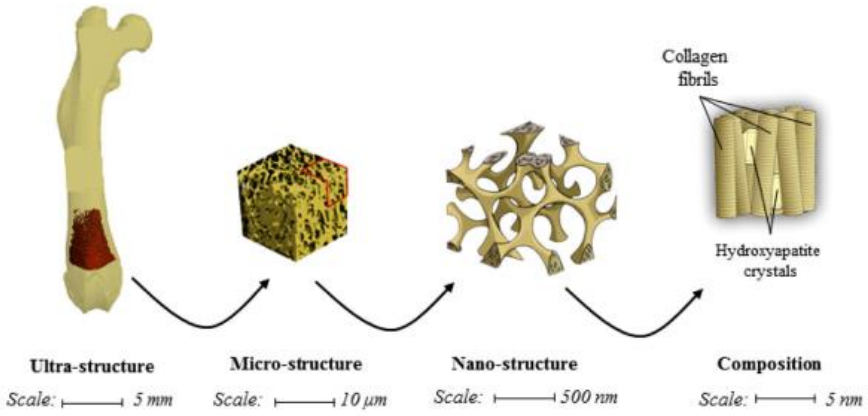

Figure 3. 1. An illustration of the hierarchical nature of trabecular bone. Image reprinted from Oftadeh et al.,2015 [6].

As mentioned before, trabecular bone is heterogeneous, and this is a critical issue that distinguishes it from many other biological tissues. Heterogeneity leads to wide variations in volume fraction, architecture (i.e., three-dimensional arrangement of the individual trabeculae) and tissue properties. Furthermore, trabecular bone is anisotropic which means that its mechanical properties depend on which direction loading is applied, more specifically on the orientation of trabeculae. According to the concepts set forth in Wolff's law[7], anisotropy develops as a form of adaptive response to functional loading, bone is placed where it most needs to be. As an example of anisotropy, it is known that mean values of strength and modulus of human vertebral bone in the superior-inferior direction are higher than those in the transverse direction by factors of 2.8 and 3.4 respectively [8].Trabecular bone possesses orthotropic symmetry, in some cases it displays transverse isotropy: there is a clear evidence that the principal material directions of trabecular bone are aligned with the principal structural directions of the trabecular architecture [8]. In this scenario, mechanical testing should be performed along the principal directions otherwise resulting measurements are difficult to interpret.

3.1.2 Mechanical behaviour of trabecular bone

Trabecular bone is the main load bearing bone in vertebral bodies and transfers the load from joints to the compact bone of the cortex of long bones. It has a better behaviour in compression rather than in tension or in shear because its strength is higher. An example of a stress-strain curve is shown in fig.3.2: the initial region of the curve is linear, where the individual trabeculae compress and bend as the bulk tissue is compressed, the second part is also linear, and extends up to yield point. This is the region from which Young's modulus of the bone is calculated. At the yield point, bonds between trabecula start to break and the compression force decreases until the final phase corresponding to the ultimate point where fracture occurs.

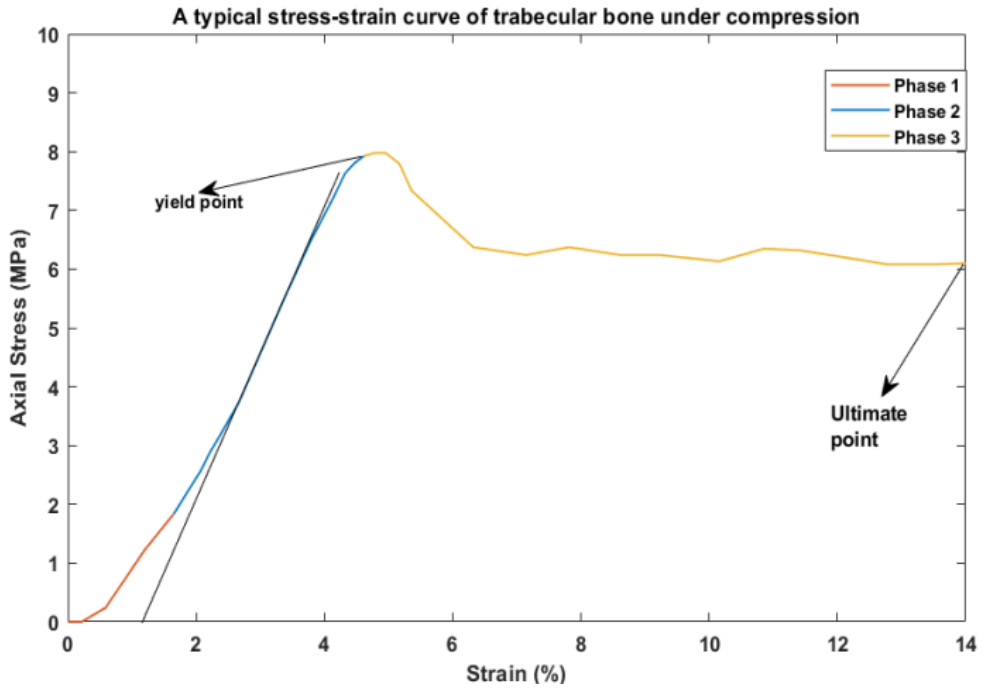

Figure 3.2. Three phases of stress-strain evolution in the trabecular bone under axial compression. The straight line on the second region in blue is used to calculate Young's modulus of the trabecular bone[9] .

The stiffness is substantially lower for trabecular bone and its tensile yield strain is higher than that of cortical bone tissue [10]. Also, trabeculae can sustain some bending deformations without losing load-carrying capacity in a catastrophic way.

3.2 Anatomy of the proximal femur

The femur is the longest bone in the human body, and it is situated in the upper leg. The main function of the femur is weight bearing and stability of gait and it is an essential component of the lower kinetic chain. Indeed, its internal structure is highly optimized to bear the loads that are transmitted from the hip joint. Furthermore, the femur acts as the site of origin and attachment of many muscles and ligaments.

It can be divided into three regions: proximal region, shaft, and distal region. In particular, the proximal femur consists of the femoral head, neck, and two bony processes – the greater and lesser trochanters (fig.3.3):

- The head articulates with acetabulum of the pelvis to form the hip joint. It has a smooth surface covered with articular cartilage.
- The neck connects the head of the femur with the shaft, it is cylindrical and set at an angle of approximately 135 degrees to the shaft.
- The greater trochanter is the site of attachment for many of the muscles in the gluteal region.
- The lesser trochanter is smaller than the greater and is the site of attachment for iliopsoas.

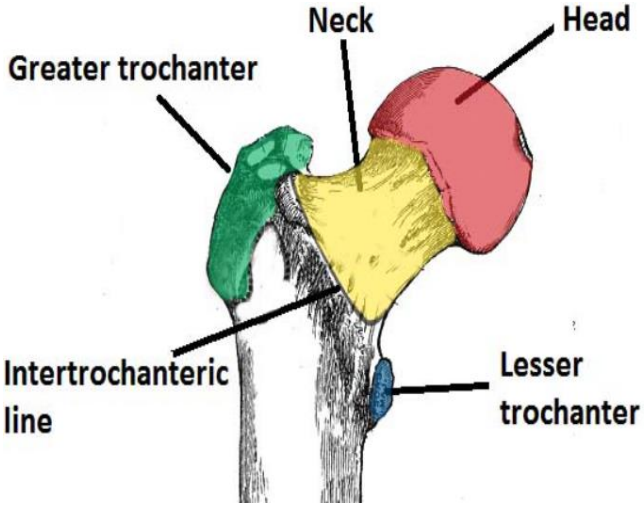

Figure 3. 3. Anatomy of proximal femur

3.3 Osteoporosis and hip fractures

Metabolic activity of trabecular bone is very high: bone cell production, mineral exchange, damage, and repair of individual trabeculae are all physiologic processes that act as a stimulus for remodeling. Bone remodeling allows to repair microfractures so that they don't become macrofractures. However, during aging, or when affected by diseases such as osteoporosis, an imbalance between resorption and formation of new bone occurs. Consequently, architecture of trabecular bone as well as its metabolic activity changes: the trabeculae become thinner, connectivity and volume fraction decrease and anisotropy increases [11].

Osteoporosis is a metabolic disease of the skeleton, which is characterized by low bone mass, micro-architectural deterioration of bone tissue leading to bone fragility and consequent increase in fracture risk. Currently, it has been estimated that more than 200 million people are suffering from osteoporosis. According to recent statistics from the International Osteoporosis Foundation, osteoporosis causes more than 8.9 million fractures annually, resulting in an osteoporosis fracture every 3 seconds [12]. Using the World Health Organization (WHO) definition of osteoporosis, the disease affects approximately 6.3% of men over the age of 50 and 21.2% of women over the same age range globally[13]. Worldwide, 1 in 3 women over

age 50 will experience osteoporosis fractures as will 1 in 5 men aged over 50 in their lifetime [13], [14].

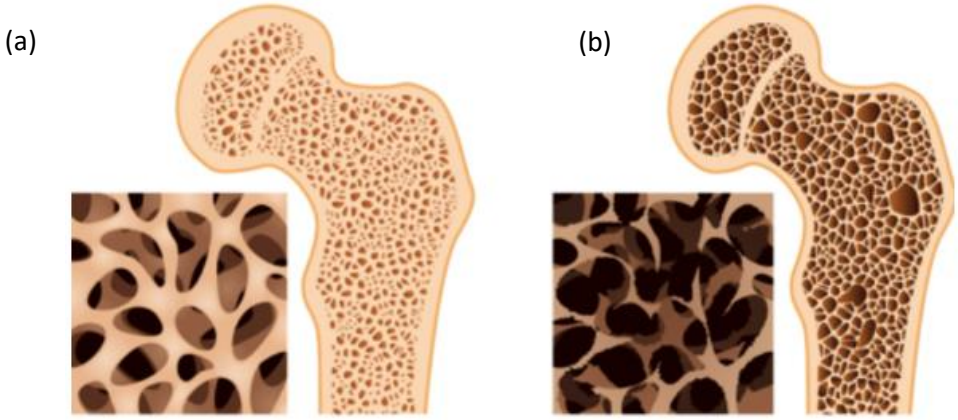

Figure 3.4. Healthy bone (a) and osteoporotic bone (b)

This disease remains widely undertreated and underdiagnosed because it has no clinical manifestations until the patient experiences a fracture. Indeed, fractures and their complications are the relevant clinical sequelae of osteoporosis. The proximal femur is one of the major skeletal sites where fracture occurs. When the bone breaks in this region, it is classified as a hip fracture. Hip fractures cause an increasing of 15-20% in mortality rate within one year and it is higher in men than in women [15]. The most common types of hip fracture are the femoral neck fracture and the intertrochanteric hip fracture.

The diagnosis of osteoporosis is established by the measurement of bone mineral density (BMD). BMD is measured by means of dual X-ray absorptiometry (DXA) which uses a very small dose of ionizing radiation to produce images of the inside of the body to measure bone loss density. This measure is the actual expression of the bone in absolute terms of grams of mineral (primarily, as g/cm2 of calcium) per square centimetre of the scanned bone [3]. Fracture risk is correlated with bone strength and increases exponentially as the BMD decreases.

Since definition of fracture risk by BMD alone is not enough to capture the majority of people at risk for breaking a bone, algorithms have been developed. One of them was approved by WHO and is called Fracture Risk Assessment Tool Model (FRAX). It combines the BMD with other risk fractures such as age, sex, alcohol intake etc. Although these algorithms lead to an improvement, the predictive capabilities are still limited probably because they don’t account for factors such as the shape of bones, or patient-

specific risk of falling which are also heavily associated with increased fracture risk [16]. In this scenario FE-models represent a beneficial tool in engineering research for more accurate predictions of fracture risk.

3.4 Finite element models for prediction of bone fracture

In biomechanics FE-models can be used to describe numerically problems which often involve complex geometries, inhomogeneous material properties, and/or complex boundary conditions. In addition, by patient-specific models, it is possible to calculate fracture strength of the femur which is another strong predictor for fracture risk [17].

The basic idea of the Finite Element Method (FEM) is to discretize a complex structure into small elements with simple shapes. The size and the shape of the element must be chosen according to the length scale of interest and to the geometry of the discretized object. The elements are interconnected through nodes situated at a specific locations within the elements and at the elements boundaries [18]. For each element its own material properties can be assigned and an approximate solution to the partial differential equations can be found. Then, these equations are assembled into a larger system of equations that cover the entire finite element mesh and by solving them stress and strain fields can be calculated.

To analyse human bone, finite element modelling has three major stages: pre-processor, solution, and the post process stage (fig.3.5):

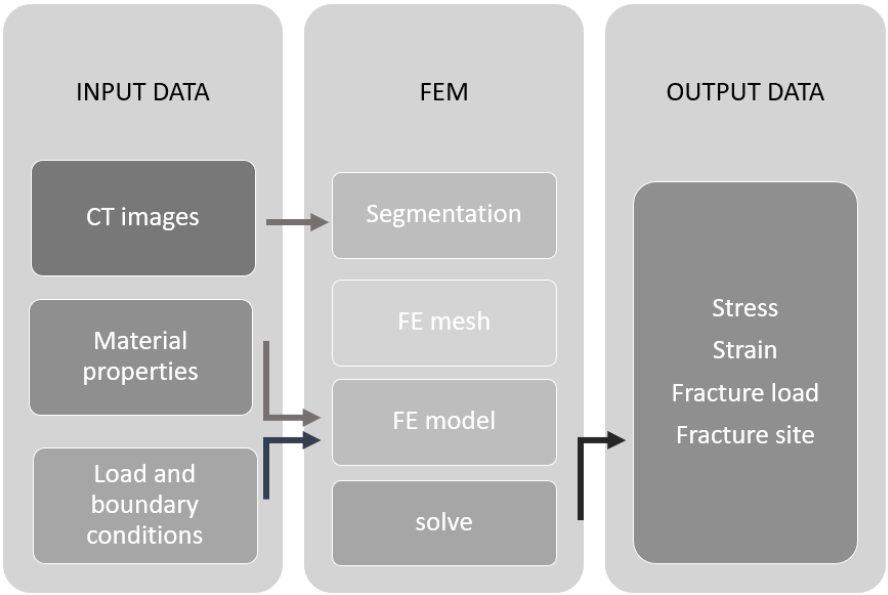

Figure 3. 5. Finite element modelling of bone based on CT images

In the pre-process stage a CAD model is required to be generated. The most common way to create it is to use clinical CT images for the segmentation of the analysed bone site. CT images proved to be a powerful tool to get subject-specific FE models [19]. Once the model is developed, the mesh generation is carried out, the material properties are assigned, and the boundary conditions are applied.

In FE model a typical drawback must be mentioned. Since equilibrium is computed and ensured only at nodes but not inside elements where equilibrium requirements are often violated, the solution obtained with these models is approximate. Therefore, accuracy and validity of the model should be considered [18]. Accuracy is evaluated by convergence test which quantifies how close the model output is to the real solution. Actually, the real solution is not known a priori, indeed we should correctly define it as "the converged solution" which can be ideally reached by decreasing elements size. Instead, validation is performed by comparing model predictions with experimental results.

3.4.1 Microstructural FE (μFE)

In this work the approach of microstructural FE is used. It deals with a novel approach because this takes into account bone microarchitecture to investigate its mechanical properties. It combines three-dimensional imaging with Finite element analysis (FEA) and is referred to as microstructural FE analysis. Image processing algorithms are adopted to generate smoother meshes of tetrahedral elements, but this procedure results in a μFE model made up of a very large number of elements. Recently special solving strategies have been developed for such large systems: for instance, the element-by-element method or the use of preconditioners have been introduced for a very efficient use of the memory. Two advantages of this approach should be emphasized: first, the tissue properties adopted in μFE can be fairly simple because studies have shown that isotropic and linear elastic material models give accurate predictions (for small deformations) of the mechanical behaviour, if compared to biomechanical testing [20]. Then, it is possible to calculate stress and strain locally within individual trabeculae in order to understand bone adaption in healthy and osteoporotic conditions [18].

3.5 X-ray tomography imaging techniques

Diagnostic imaging techniques help narrow the causes of an injury or illness and ensure that the diagnosis is accurate. These techniques include computer tomography (CT) scans which are briefly described in the section below.

3.5.1 Clinical CT

In clinical setting, CT is used to support patient diagnostics. During this imaging procedure, a beam of X rays is aimed at a patient and rotated around the body. As the x-rays leave the patient, they are picked up by detectors and transmitted to a computer which uses mathematical techniques to construct a 2D image slice of the patient. Once a number of successive slices are collected by the machine's computer, they can be digitally "stacked" together to form a three-dimensional image of the patient that allows for easier identification and location of basic structures as well as possible tumours or abnormalities. Since long exposure to high energy X-rays can lead to tissue damage, the X-ray energy and scanning time are kept low and obviously this leads to images that have a low resolution (around 1 mm) and low contrast [19].

3.5.2 Micro-CT (μCT)

Compared to clinical CT, μCT scanners are used to obtain images at a higher resolution. It allows to see the inside of something without having to destroy the object itself. In this procedure, the sample rotates instead of the X-ray source and the detector, and the resolution can reach down to 1 μm. Trabecular structures can be resolved, and more detailed FE models can be built.

3.5.3 Synchrotron CT

Synchrotron radiation micro-computed tomography is an imaging technique which has become increasingly popular in bone research, and it possesses significant advantages over standard micro-CT. A synchrotron source provides a high-flux, high-intensity, and monochromatic X-ray beam, allowing acquisition of quantitative high-resolution 3D images (<0.1 μm) with a high signal-to-noise ratio [21]. This technique has recently been used to study trabecular bone architecture and microcracks propagation when applying mechanical loading. Although the several advantages of this

procedure, a critical aspect, which is common to all X-ray devices, has to be mentioned. Utilization of SR-μCT exposes the samples to a large radiation dose, which can be detrimental to the sample constituents, especially the collagen, and may affect the mechanical properties of the samples. For instance, as reported by Fernandez et al. [10], DVC successfully correlated the presence of microcracks in the highly-irradiated sample as well as the progressive strain accumulation in the tissue. Many studies tried to define a safe exposure that would not compromise the mechanical stability of the tissues: Barth et al. [22] defined a "safe" radiation level of 35 kGy and since then this has been considered as a reference in several works using SR radiation for imaging bone tissue.

3.6 Image correlation methods

Image correlations methods have been used increasingly to analyse tissue strains during in situ loading. These methods can be divided into surface and volumetric image correlations. The surface scenario is usually referred to as digital image correlation (DIC), whereas the volumetric scenario, an extension of DIC, is generally referred to as digital volume correlation (DVC). DVC is the procedure used by Turunen et al. [1] to determine the strains inside the trabeculae and is described in this section.

3.6.1 Digital volume correlation (DVC)

Digital Volume Correlation (DVC) is currently the only experimental measurement technique to calculate the 3D distribution of strain magnitudes inside a biological structure, which makes it suitable to validate fracture criteria in computational models. Conducting in situ loading experiments together with high resolution X-ray computed tomography (CT) enables acquisition of sequences of 3D images of a sample during loading. DVC can then be applied to 3D sub-regions of two image volumes from different stages of deformation, and internal displacements can be calculated by tracking the structures from one load step to another [1]. This procedure allows to predict damage location before gross failure occurs.

The DVC methods are based on two approaches: a local approach (fig.3.6b), which is the most commonly used, consists of dividing the reference and the deformed image volumes into smaller interrogation windows that are then individually correlated [23]. In the second approach called global (fig.3.6a), the registration is performed on the whole volume of interest, and

simultaneously extracts information from all elements in an iterative manner. This leads to continuous displacement fields. Although improvement have been performed for the two methods, some differences emerge. For instance, the global approach has shown lower systematic errors and better accuracy when compared to local approach where Fast Fourier Transform (FFT) generates numerical artefacts [23],[24]. Moreover, the obvious advantage of the global approach is that the displacement field is continuous and smooth because of the imposed continuity at nodes, but an advantage is that the quality of the speckle pattern is difficult to control and this leads to some errors in the displacements [25]. The differences between Global and Local approach are depicted in fig.3.6.

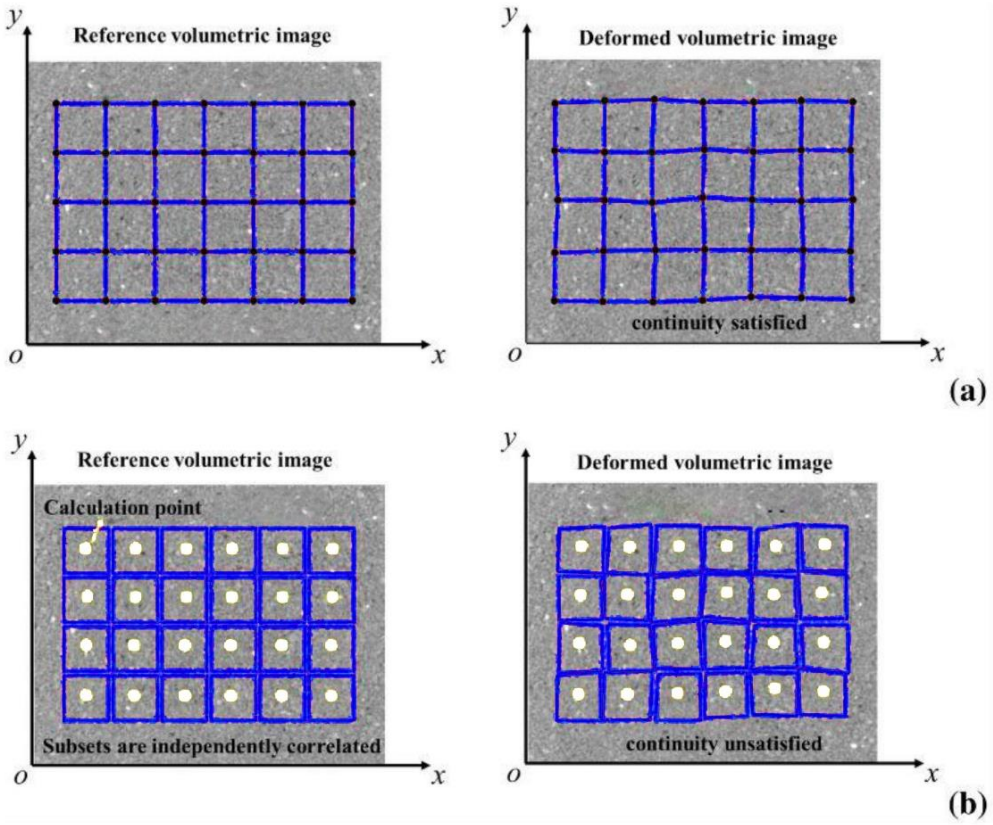

Figure 3.6. Differences between the two approaches: a) Global DVC and b) Local DVC

3.6.2 Local Approach

The method utilizes a sequence of consecutive 3D image data and begins with the 3D volume being subdivided into several sub-volumes which represent the process of the object displacement and deformation.

The essential DVC parameters are shown in a 2D case for simplicity (fig. 3.7), and they are:

- ✓ Search window which defines the range of possible displacements values in pixels.
- ✓ Correlation window (CW) which defines the sub-volume extension from the central node in pixels.
- ✓ Node spacing (NS) which is the spacing between the points of the output grid where the displacements will be calculated.

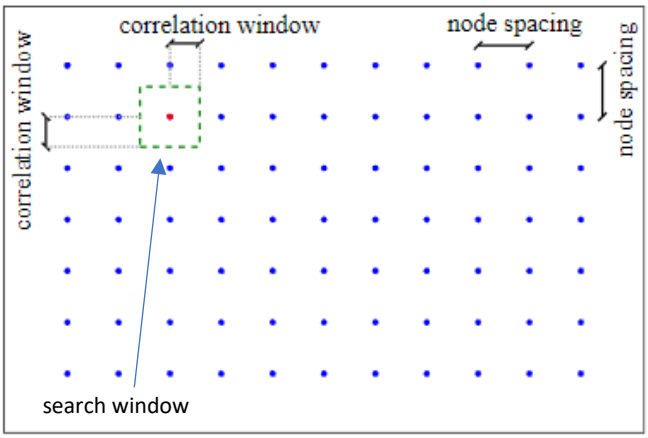

Figure 3.7. Essential DVC parameters

DVC local approach works by comparing consecutive digital volume images taken during the loading of the sample, the reference image and the deformed one. A region of interest is selected, and a grid of regularly spaced nodes is placed inside the region. For each node, a correlation window is defined in which a unique speckle pattern is found. In the subsequent image, a search window is defined in a region of the image that roughly matches the region of interest in the first image. A grid of nodes is placed also in this window. The correlation window from the first image is compared to equally sized selections around the nodes in the second image. The size of the search window should be as small as possible, but larger than the maximum local displacement between two images [19]. The DVC procedure provides the displacement fields by tracking the translation of small sub-volumes (i.e., correlation windows, CW) between two subsets of subsequent images. To obtain strain fields, the grid of nodes can be turned into triangles and

consequently a strain tensor (i.e., Green-Lagrange strain tensor) can be calculated from the deformation gradient tensor.

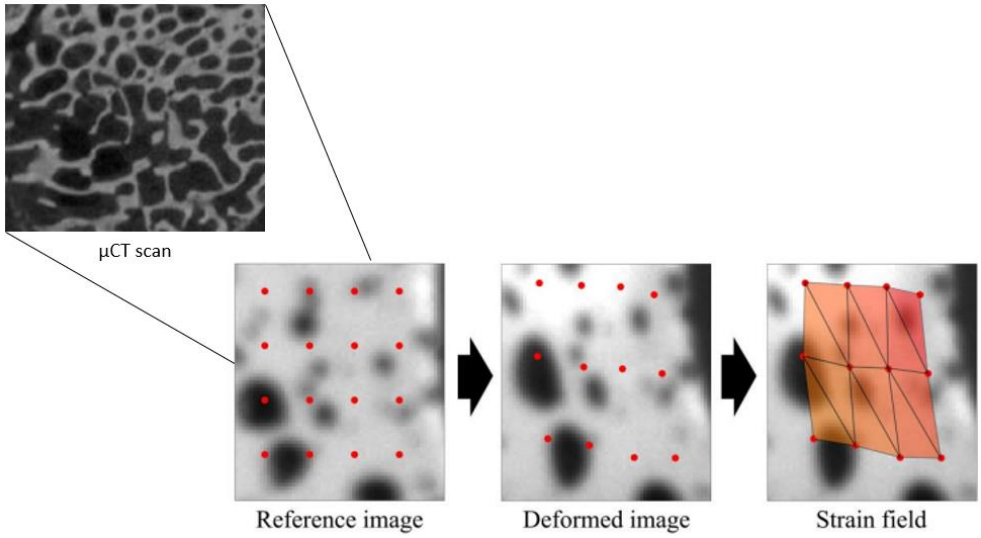

Figure 3.8. Local DVC approach applied on µCT scan. Image adapted from Kok 2021 [19]

3.6.3 Incremental DVC approach

When severe decorrelation effect occurs to the deformed volume image undergoing large deformation/rotation, routine DVC analysis using a fixed reference volume image cannot yield reliable displacement measurement or even fails [26]. To address this challenge and to realize large deformation measurement, incremental DVC analysis is developed (fig.3.9).

In this technique, the deformed volume image in the previous correlation is selected as a new reference volume image in current correlation. In this way, the reference volume image is updated constantly in each correlation step so that the deformation between two neighbouring states of deformation is sufficiently small to ensure correlation. These intermediate displacements are then summed up to determine the total displacement vector.

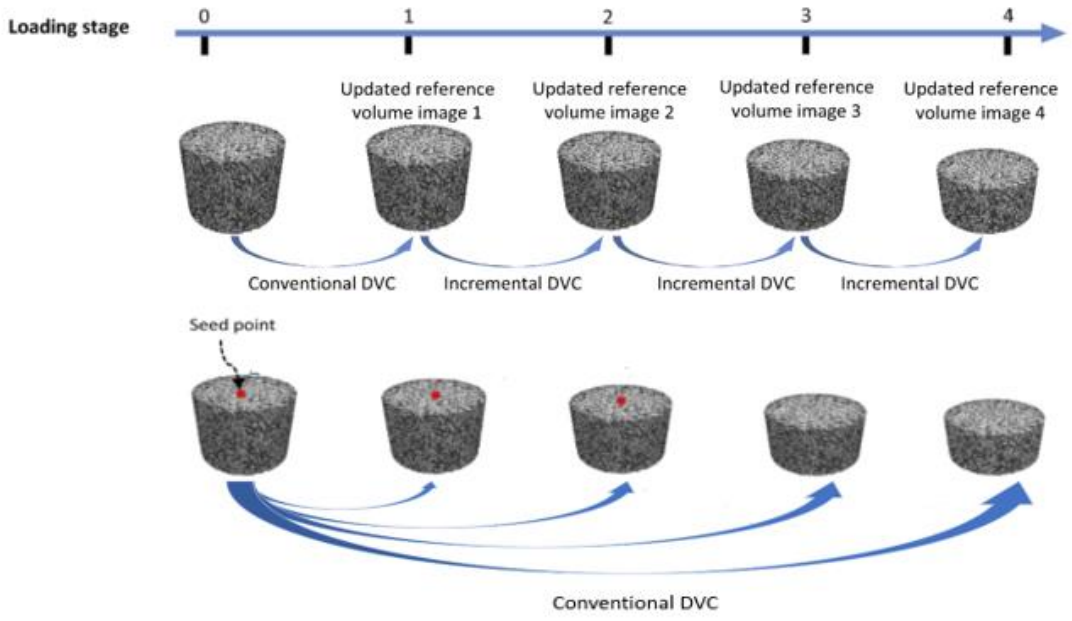

Figure 3.9. Scheme incremental DVC vs conventional DVC. Image adapted from Wang et al., 2017 [26].

Chapter 4

Material & Methods

This section describes the methodologies adopted in the studies conducted during this thesis work. First, a list of the material used for the studies is provided. Then, the methodology used to build subject-specific FE model of a sub-volume of trabecular bone from human cadavers and the techniques to combine FE modelling with experimental data from DVC are described.

4.1 Material

In this master's thesis, DVC measurements previously collected and whose outcome has been reported in Turunen et al. work [1] are used. Their work will be summarized below.

Trabecular bone plugs from femoral head of human cadavers were extracted and placed inside the container of a custom-made loading rig. The size of the plugs is 6.3 mm in height and 7.1 mm in width. They were compressed in 7 displacements rate-controlled steps and each step was ~ 0.85% of strain with ~ 0.85%/min loading rate. A small portion (2.7x2.7x7.1 mm^3) of the entire plug was imaged under zero-load and during the following loading steps. Between two consecutive steps, the loading was stopped to scan the sample in steady-state conditions minimizing movement artefact during image acquisition. Imaging was performed with high-resolution synchrotron radiation X-ray tomography (SR-μCT).

A scheme of the experiment is shown in fig.4.1 reprinted from Turunen et al. article[1].

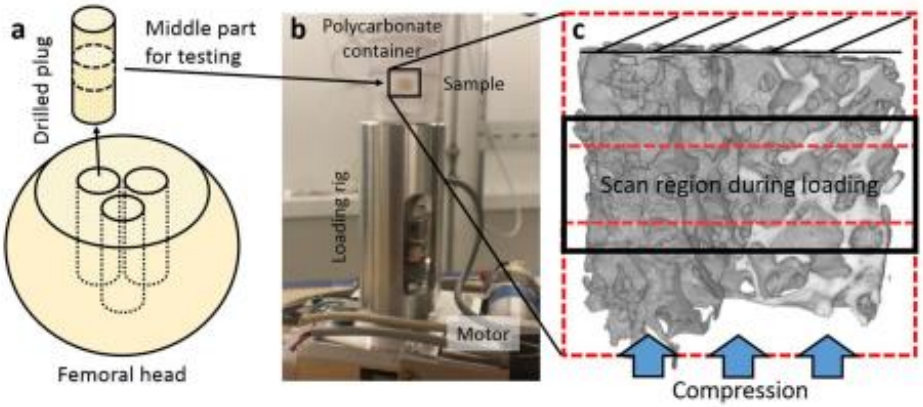

Figure 4.1. Set up of the experiment: (a) Collection of trabecular bone plugs. (b) Compression in a custom-made loading rig. (c) Middle part of FOV imaged during loading. Image reprinted from Turunen et al [1].

Digital volume correlation was used to determine the strains inside the trabeculae. To perform DVC analysis, image stacks between consecutive loading steps were pre-processed (aligning the images for rigid deformation, filtering using a 3D median filter to reduce noise and masking of voids/background). DVC analysis was performed on high-resolution data (voxel size= 3.6×3.6×3.6 μm^3) as well as on downscaled SR- µCT scans to evaluate the effect of image voxel size on strain magnitudes. The filtered scans were downscaled by a factor of 4 and 8 resulting in an isotropic voxel size of 14.44 µm and 28.88 µm, respectively.

µCT images of the whole middle part of the sample and of the isolated sub-volume were used in this thesis project. They were obtained from Turunen et al[1].

DVC images in .tif format of the high-resolution, downscaled by factor of 4 and downscaled by a factor of 8 data were used in this thesis project. They were obtained from Turunen et al[1].

The provided data for the project can be summarized in Fig.4.2.

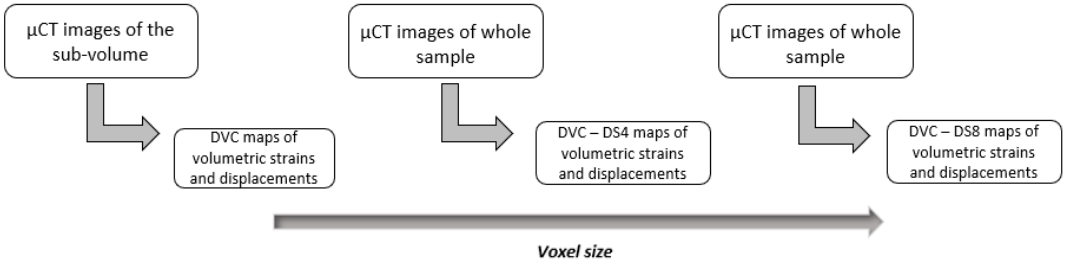

Figure 4.2. Sketch of the provided material

4.2 µCT- based FE model

In this section the meshing methodology is explained. Three different levels of meshing are carried out. First, a sub-volume extracted from the black box in fig.4.1 was meshed, then analysis included the black box itself. The idea was to compare different FE models at different level of resolution.

4.2.1 Segmentation of CT images

To build the models, µCT bone mineral density images of the high-resolution data and the ones downscaled by a factor of 4 and 8 were used. These images were used as input for the segmentation which was performed on MATLAB (Version R2021b, Math Works, Natick, NA, USA). A greyscale threshold value of range 155-255 was assigned to the mineralized bone tissue to differentiate between bone and surrounding tissue.

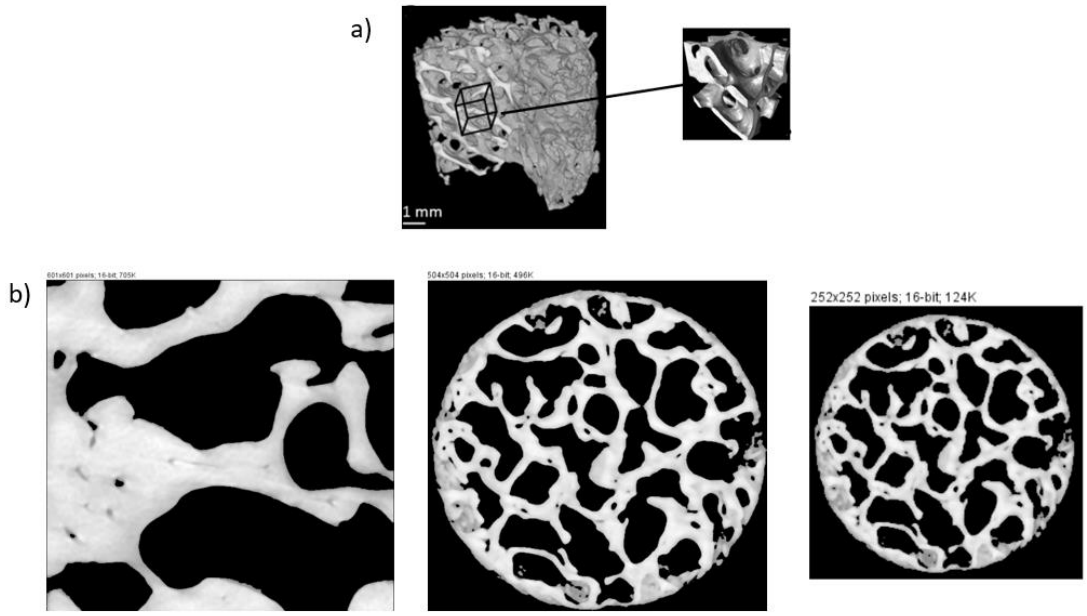

Figure 4.3. Sub-volume from trabecular bone sample a) and µCT images of high-resolution, downscaled by 4 and downscaled by 8 data b). Image a) is reprinted from Turunen et al.

4.2.2 Mesh Generation

After segmentation, model generation was done in MATLAB using the toolbox iso2mesh (Qianqian Fang & Boas, 2009). The mesh generation algorithm is a Delaunay refinement process followed by an optimization phase. Tetrahedral elements with four nodes are used and the mesh parameters are controlled by the MATLAB function. For semplicity, the following considerations about the set of parameters chosen will be referred to the sub-volume model.

The Delaunay refinement process is driven by criteria concerning either the mesh cells or the surface facets. The refinement process terminates when there are no more mesh cells or surface facets violating the user-specified criteria. The Delaunay refinement eliminates all kind of quasi degenerate tetrahedra except slivers. At the end of the refinement process, some sliver shaped tetrahedra may occur in the mesh. The optimization phase aims at eliminating slivers.

The criteria can be tuned by the need to realize a model with an adequate size of mesh elements and to ensure accuracy of boundary approximation and topological conditions. The default criteria for surface facets are governed by the three following parameters:

- *the angular bound:* This parameter controls the shape of surface facets. Actually, it is a lower bound for the angle (in degree) of surface mesh facets. The termination of the meshing process is granted if the angular bound is at most 30 degrees.
- *the radius bound:* This parameter controls the size (edge length) of surface facets. Actually, each surface facet has a surface Delaunay ball which is a ball circumscribing the surface facet and centered on the surface patch. The radius bound is an upper bound on the radii of surface Delaunay balls.
- *the distance bound:* This parameter controls the approximation error of the surface. Actually, it is an upper bound for the distance between the circumcenter of a surface facet and the center of a surface Delaunay ball of this facet.

The default criteria for mesh cells are governed by two parameters:

- *the radius-edge bound:* This parameter controls the shape of mesh cells (but can't filter slivers, as we discuss earlier). Actually, it is an upper bound for the ratio between the circumradius of a mesh tetrahedron and its shortest edge.
- *the radius bound:* This parameter controls the size (edge length) of mesh cells. Actually, it is an upper bound on the circumradii of the mesh tetrahedra.

Figure 4.4 shows how the mesh generation process behaves with respect to these parameters.

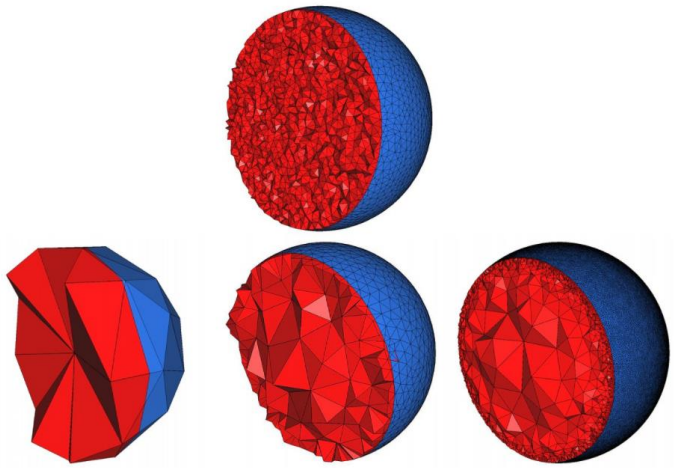

Figure 4.4. Top: the mesh is obtained using the parameters (25,0.15,0.05) for the angular bound, radius bound, and distance bound of surface facets and (4,0.2) for the radius-edge bound and radius bound of mesh cells. With these parameters, a uniform mesh which contain tetrahedra of about the same size is obtained. Bottom left: the mesh is obtained by relaxing the size bound of tetrahedra and facets. The result is a small coarse mesh. Bottom middle: the mesh is obtained from the previous one by tightening the distance bound of surface facets. In this case 3D mesh has a dense surface mesh achieving a precise approximation. Bottom right: the mesh is obtained from the previous one by fixing radius bound of surface facets to 0.01. The surface mesh is then denser. Image reprinted by CGAL user and reference manual [27].

In the high-resolution based FE-model, the radius bound is set to 3.5 pixel (0.93 mm) and the distance bound is set to 0. Other set parameters are maximum volume, which controls the maximum volume an element can have in the mesh and is set to 4.5 voxel (0.0162 mm^3).

These values are chosen to obtain a high-quality mesh with minimum variation in the volume of elements throughout the model. Mesh quality plays a significant influence on the accuracy of the model since mesh is an approximation of the actual geometry. A mesh is usually considered to be of higher quality compared to another mesh if it improves at least one of the most important simulation properties: time to convergence, stability or accuracy without affecting the others negatively. Mesh quality can be measured by using a set of quality metrics which determine how far we are from an ideal cell shape. In this thesis work, the Joe-Liu mesh quality metric was used as the parameter to measure tetrahedron shape. Liu and Joe in their work [28] described three different tetrahedron shape measures (solid angle, aspect ratio and mean ratio) and they derived a relationship between a pair of the three mentioned parameters demonstrating that, with the maximum reached value of 1, these three shape measures are equivalent. Briefly the radius ratio is the ratio of inradius to circumradius of a tetrahedron scaled by 3. The aspect ratio is a measure of the stretching of a cell, and it is computed as the ratio of a cell's longest length to the shortest length (fig.4.5). The calculation method of this parameter varies according to the cell type. We are using tetrahedral cells, so aspect ratio is correlated between the maximum edge length and radius of the cell's internal sphere.

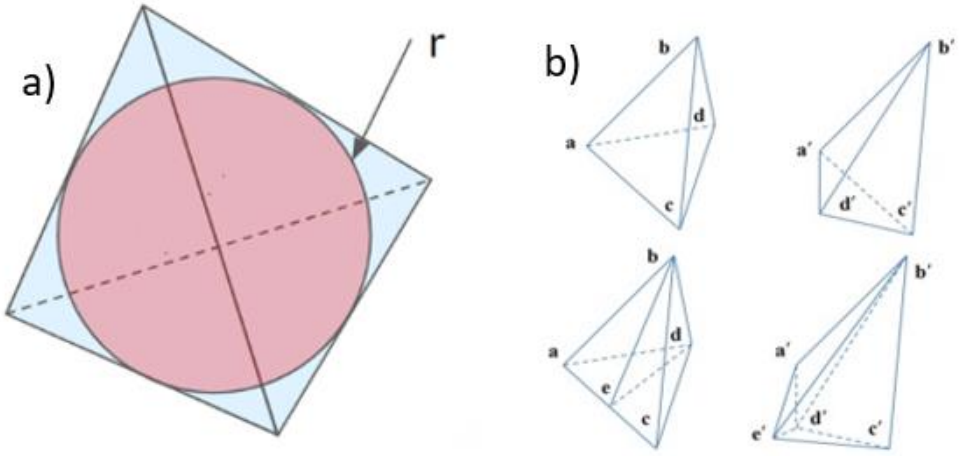

Figure 4.5. Tetrahedral cell with aspect ratio of 1 (a) and a tetrahedron (**a**,**b**,**c**,**d**) (top left) is deformed such that (**a**,**b**,**c**) are fixed and **d** is moved to **d′** so the resulting tetrahedron (**a′**,**b′**,**c′**,**d′**) (top right) is inverted (b).

In the mentioned above work [28], the authors stated that larger measure value for a tetrahedron means that the tetrahedron is well-shaped (i.e., a value close to 1 represents equilateral tetrahedron). If one of the shape measures is close to zero, this indicates a poorly-shaped tetrahedron (i.e., a degenerated tetrahedron with a zero volume).

To refine the model, elements should have a similar and small volume to obtain a uniform mesh. As these elements are made smaller and smaller and with a similar volume, as the mesh is refined, the computed solution over each element will approach the true solution.

The meshed model is originally in voxels, and the size is 601x601x401 voxels. A conversion to the true physical size in millimetres is needed. For high resolution data the voxel size is 3.6x3.6x3.6 μm^3 and is used to scale the image to millimetre units. So, the dimension of the sub-volume is $2.17 \times 2.17 \times 1.45$ mm^3.

4.2.3 Material properties

The material properties for the FE model were assumed to be linear, elastic and isotropic with a uniform Young's modulus (E) of 13 GPa [6] and a Poisson's ratio (ν) of 0.3.

4.2.4 Boundary conditions

To simulate the experiment presented in Turunen et al., boundary conditions were applied to the model. Node sets were created as it follows:

- ✓ $NStop = \{i: zi > ztop\}$; where $ztop$ was chosen such that the elements in $NStop$ have nodal points that have applicate greater than 98% of the height (z-axis) of the model;
- ✓ $NSbottom = \{i: zi < zbot\}$; where $zbot$ was chosen such that the elements in $NSbottom$ have points where the applicate is lesser than 2% of the height (z-axis) of the model;
- ✓ $NSleft = \{i: xi < xleft\}$; where $xleft$ was chosen such that the elements in $NSleft$ have the points where abscissa is greater than 98% of the length (x-axis) of the model;
- ✓ $NSright = \{i: xi > xright\}$; where $xright$ was chosen such that the elements in $NSright$ have the points where abscissa is lesser than 2% of the length (x-axis) of the model;
- ✓ $NSfront = \{i: yi < yfront\}$; where $yright$ was chosen such that the elements in $NSfront$ have the points where ordinate is lesser than 2% of the width (y-axis) of the model;
- ✓ $NSback = \{i: yi > yback\}$; where $yback$ was chosen such that the elements in $NSback$ have the points where ordinate is greater than 98% of the width (y-axis) of the model;

The node-sets created are shown in the following figure 4.6.

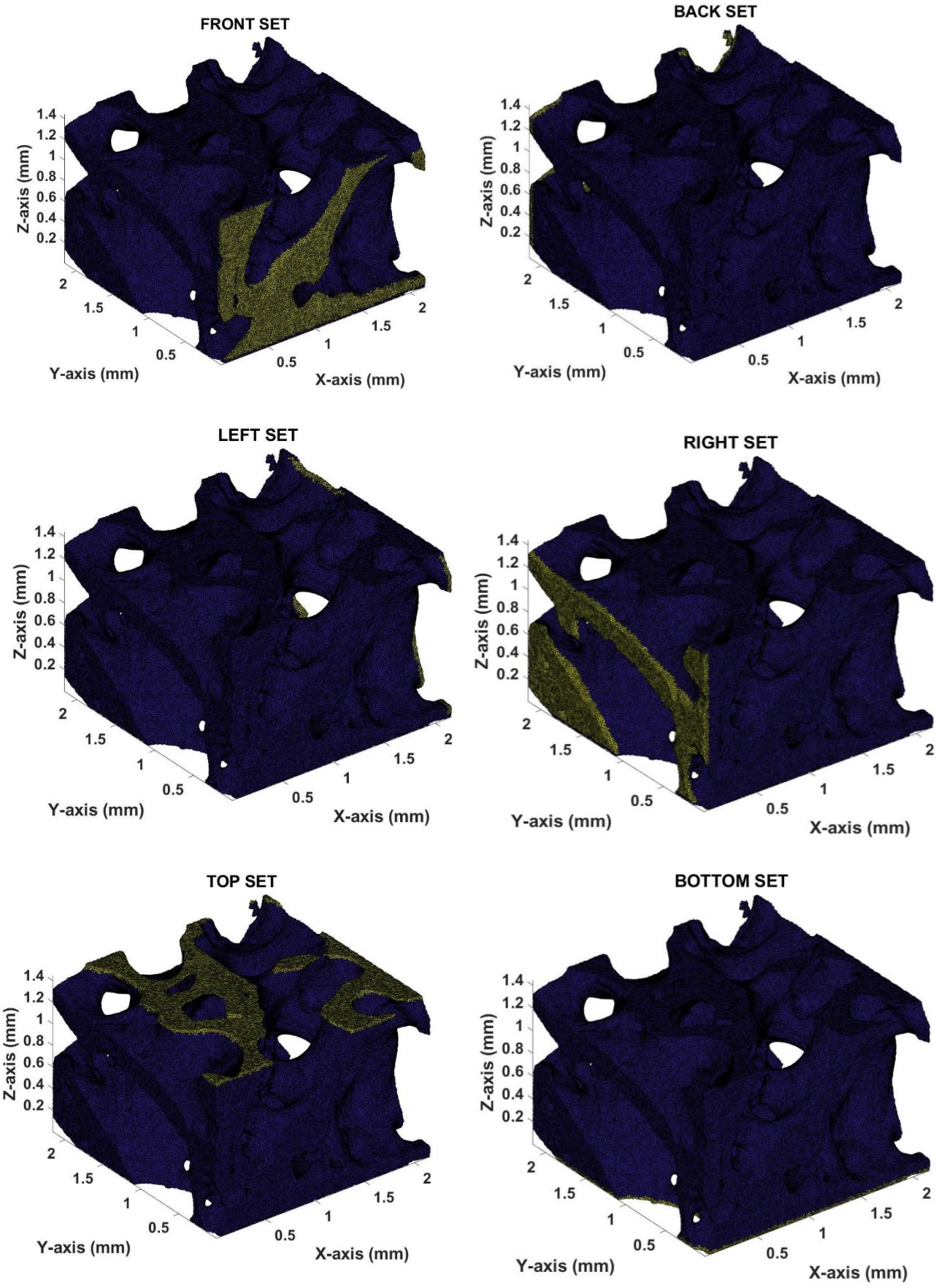

Figure 4.6. Different sets of nodes on the mesh model

Two different types of boundary conditions were applied (fig.4.7):

- ✓ Simple compression: the base of the model, i.e., the bottom nodes set was kept fixed or encastre with a degree of freedom equal to 0. The top nodes set was subjected to a displacement in the z direction to simulate the compression. The displacement varies according to the load step of the experiment, and it was calculated as explained in the section 3.2.3.

$$(x_i, y_i, z_i) = (0,0,0)\ \forall\, i \in NP_{bottom}$$

$$(x_i, y_i, z_i) = (0,0,-\Delta)\ \forall\, i \in NP_{top}$$

- ✓ Confined compression: the base of the model, i.e., the bottom nodes set was kept fixed or encastre with a degree of freedom equal to 0. The top nodes set was subjected to a displacement in the z direction to simulate the compression. The displacement varied according to the load step of the experiment. Two parallel faces ($NPleft$, $NPright$) were constrained in the x direction whereas two were constrained in the y direction ($NPfront$, $NPback$).

$$(x_i, y_i, z_i) = (0,0,0)\ \ \forall\, i \in NP_{bottom}$$

$$(x_i, y_i, z_i) = (0,0,-\Delta) \forall\, i \in NP_{top}$$

$$x_i = 0\ \ \forall\, i \in NP_{left}$$

$$x_i = 0\ \ \forall\, i \in NP_{right}$$

$$y_i = 0\, \forall\, i \in NP_{front}$$

$$y_i = 0\, \forall\, i \in NP_{back}$$

The idea behind this choice was to simulate a condition as close as possible to the experimental boundary conditions, according to the physiological case. First, simple compression is the simplest loading condition which reproduces what is done in the experiment. Then, confined compression simulates the condition where sub-trabecular volume is affected by the pressure of the surrounding bone.

For all the following analyses the Z direction is representative of the axial axis of the sample, X and Y refer to the transverse directions without a precise anatomical reference. For clarity, only the BCs of the high-resolution based model are shown in fig.4.7.

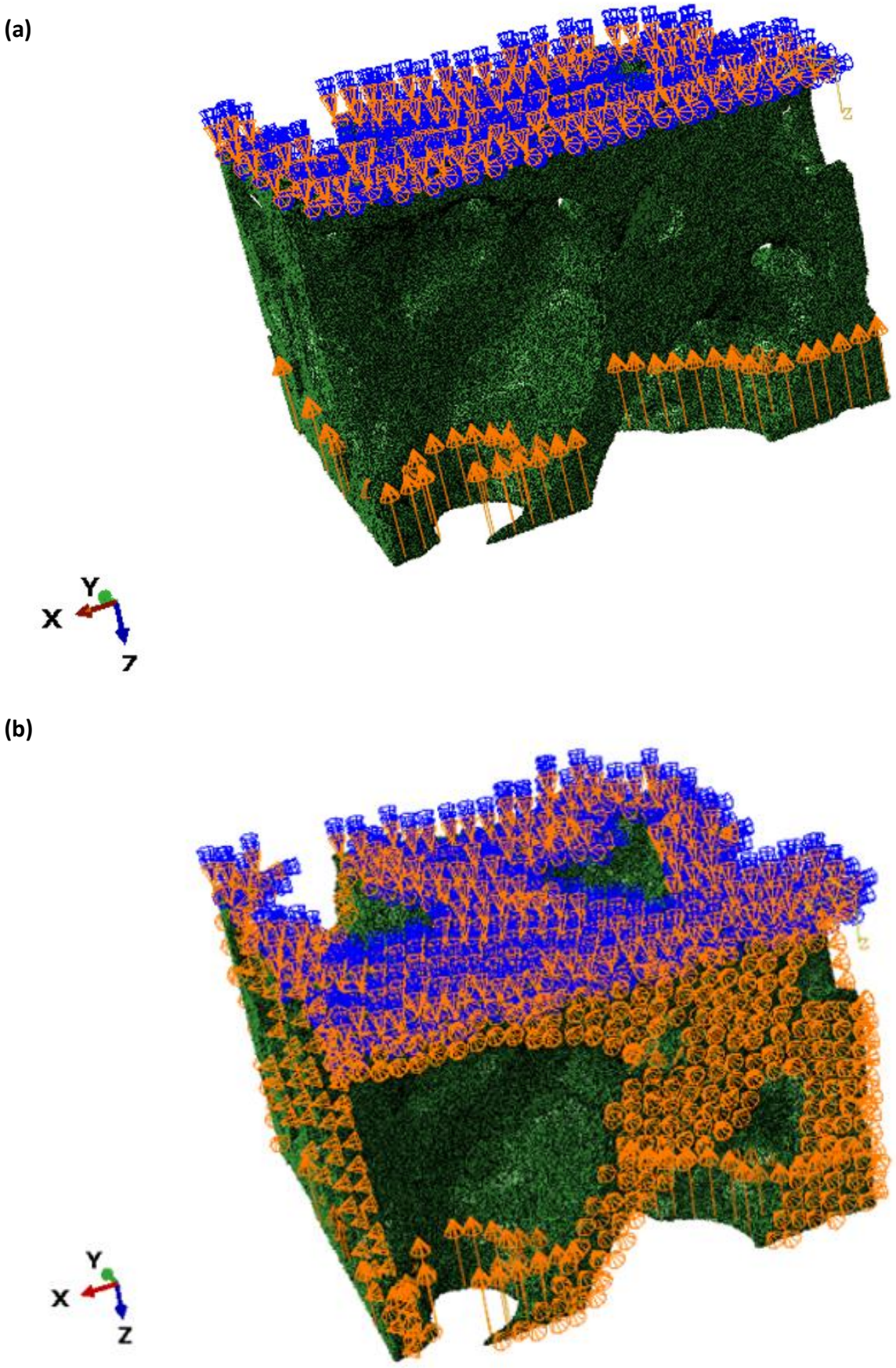

Figure 4.7. Simple compression (a) and confined compression (b) for sub-volume FE model.

4.2.5 Displacement

Since each loading step is ~ 0.85% of strain, the global displacement along z-direction is calculated from the corresponding strain for each loading step accounting for the height of the analysed object. In mathematical terms the following formula is used:

$$\varepsilon_i = -0.0085 \text{ x } a \quad \forall\, a = \{1,2,3,4,5,6,7\}$$

$$u_i = \varepsilon_i \text{ x } H$$

Where H is the height of the bone sample and i is the load step number.

In the project two different cases were analysed: the box included in the scan during the experiment and the sub volume. The applied displacement varies because the height of the two samples is different:

LOAD STEP	DISP. WHOLE SAMPLE (mm)	DISP.SUBVOLUME (mm)
LOAD STEP 0-1	0.019	0.012
LOAD STEP 1-2	0.037	0.024
LOAD STEP 2-3	0.056	0.036
LOAD STEP 3-4	0.074	0.049
LOAD STEP 4-5	0.093	0.063
LOAD STEP 5-6	0.11	0.073
LOAD STEP 6-7	0.13	0.086

Figure 4.8. Displacement values in BCs for both analysed cases

4.2.6 Volumetric strain

Volumetric strain is the parameter used by Turunen et al. in their work [1] to investigate evolution of loading at the sub-trabecular level. This parameter is defined as the unit change in volume, i.e., the change in volume divided by the original volume. In the 3D case, which is our case, we can consider the element undergoing strains ε_{xx} ε_{xy} etc., Fig. 8a. The same deformation ε is viewed along the principal directions in Fig. 4.9b, for which only normal strains arise.

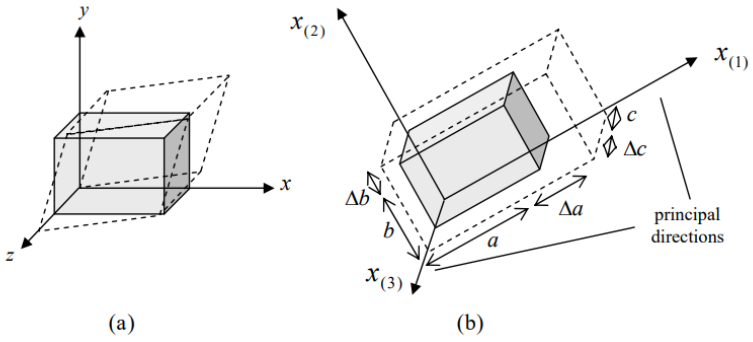

Figure 4.9. A block of deforming material; (a) subjected to an arbitrary strain, (b) principal strains

The volumetric strain is:

$$\frac{\Delta V}{V} = \frac{(a+\Delta a)(b+\Delta b)(c+\Delta c)-abc}{abc} \dots (1)$$

$$\frac{\Delta V}{V} = (1+\varepsilon_{xx})(1+\varepsilon_{yy})(1+\varepsilon_{zz}) - 1 \dots (2)$$

$$\frac{\Delta V}{V} = \varepsilon_{xx} + \varepsilon_{yy} + \varepsilon_{zz} \dots (3)$$

The squared and cubed terms can be neglected because of the small-strain assumption. The terms εxx, εyy, and εzz are the longitudinal strains in the x, y, and z directions, respectively. Stress and strain invariants are defined as quantities that remain unchanged during coordinate transformation. The first strain invariant is defined as $I = \varepsilon xx + \varepsilon yy + \varepsilon zz$. The compressive volumetric strain is considered the negative of the sum of normal strains and invariant, i.e., the strain remains constant on coordinate transformation (Kelly, 2021).

4.3 Simulations

The simulations on the model for both sets of boundary conditions were performed using the software ABAQUS–SIMULIA 2021 by Dessault Systèmes. Principal strains, volumetric strains and displacements values were extracted by using a URDFIL subroutine which writes out nodal or element results.

4.4 Convergence analysis

To get adequate results from simulations, it is important to use a sufficiently refined mesh. Coarse meshes as well as overly refined meshes can yield inaccurate results in analyses. Too refined mesh implicates higher computational time to solve equations to nodes because the number of elements increases. Therefore, first a mesh convergence analysis was performed. The numerical solution provided by the model will tend toward a unique value once the mesh density increases. The mesh is said to be converged when further mesh refinement produces a negligible change in the solution.

The following convergence study was carried out on the sub-volume model from high-resolution data. The mesh convergence analysis took into consideration eleven meshes and it was performed by varying three different parameters: maximum volume of elements, optimum radius bound, and optimum distance bound whose definitions were explained before. The maximum volume and the optimum radius bound decreased through consecutive steps while the optimum distance bound was set to 0 in order to reduce the approximation error of the surface.

MESH	MAX VOLUME (VOXEL)	OPT. RADIUS BOUND (PIXEL)	OPT. DISTANCE BOUND (PIXEL)	N. ELEMENTS
1	25	22	0	16541
2	20	15	0	36707
3	15.2	13.5	0	73224
4	12.5	9.5	0	141251
5	10	8	0	259606
6	8.3	6.25	0	459697
7	7.5	5.2	0	645690
8	5.8	4.2	0	1332450
9	5.5	4	0	2000000
10	4.5	3.5	0	2500000
11	3.5	2.2	0	2743530

Figure 4.10. Parameters chosen for each mesh and corresponding number of elements.

For each mesh the maximum absolute volumetric strain and the maximum major principal strain were looked to be converged. The percent error between consecutive mesh refinements was computed (see more details in results 5.3). It was assumed that when the current mesh differs less than 2% from the previous one, the convergence criterion is fulfilled.

4.4.1 ROI definition

The analysis was carried out on a specific region of the model (ROI) which corresponds to the region of the fractured elements. The region of interest was defined by Turunen et al. [1]. The authors identified the fracture plane from the fracture line across the trabeculae. Then, they defined a region which extends ± 5 voxels (i.e., ~18 μm) from the crack in all directions [1]. The goal was to quantitatively separate localized strains around fractures from the rest of the strains of bone metrics in order to compare them. Therefore, the elements within the ROI are not only actual fractured elements but also elements close to the fracture. This region is shown in fig. 4.11.

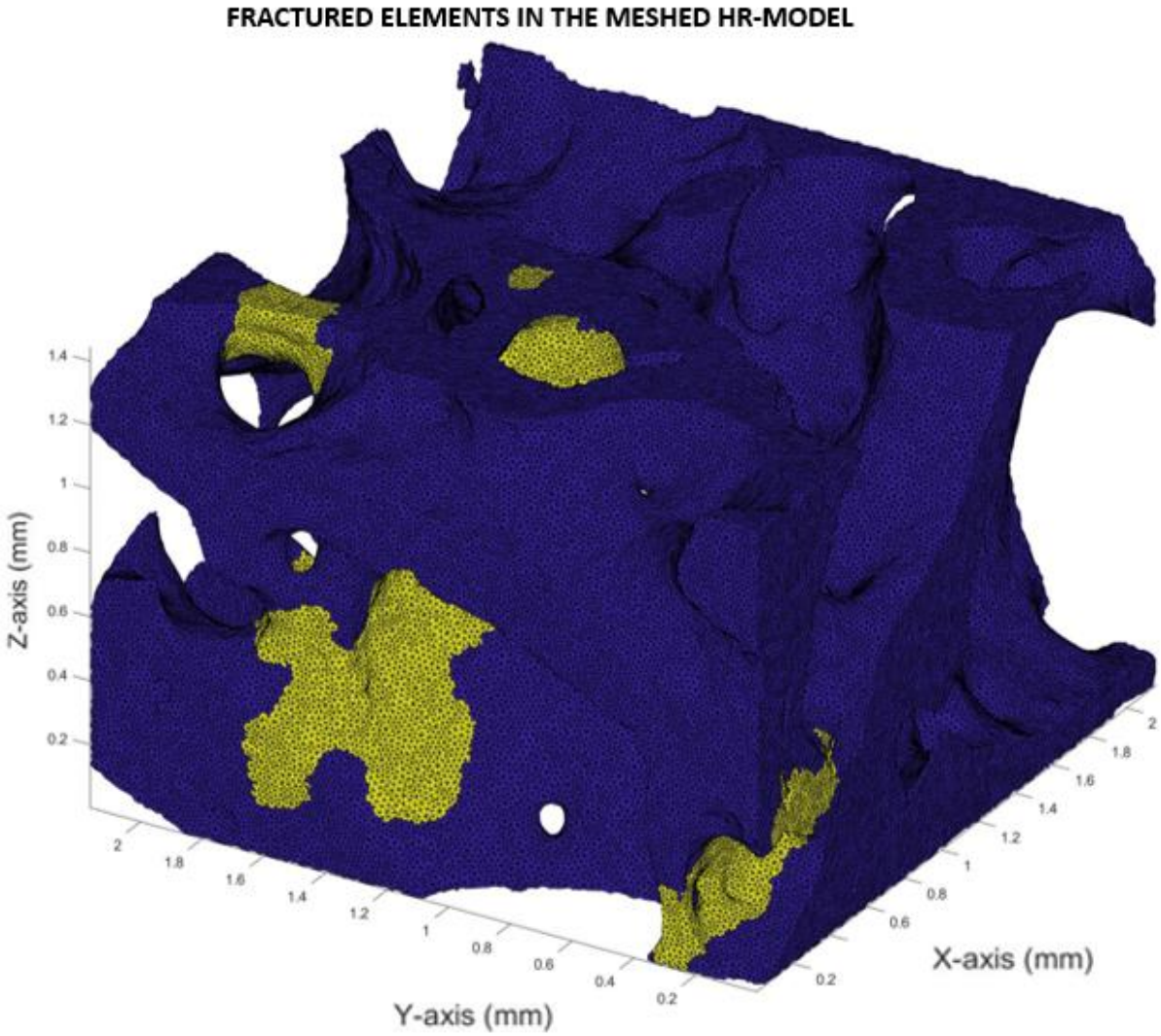

Figure 4.11. Region of interest where cracked trabeculae (yellow parts) were observed by visual inspection.

Computationally, the three-dimensional fracture region was obtained in three different steps. First, the damaged zone was segmented to isolate the fractured elements from within the meshed FE model. Then, the segmented zone was dilated of 10 voxels in all directions. This was done to increase the region and make sure that all the relevant elements of the mesh would fall into the identified ROI. The mesh of this region was built on MATLAB and by the function *inpolyhedron* it was verified which nodes of the entire mesh of the sub volume are inside the triangulated surface of the smaller mesh. Those are the nodes which define the ROI. Finally, the elements attached to the nodes of the ROI were selected.

4.5 DVC data analysis

DVC analysis was performed by Turunen et al. on high-resolution, downscaled by 4 an 8-factor data with the same protocol to evaluate the effect of image voxel size on strain magnitudes. In addition, since the analysis is related to two consecutive loading steps, incremental DVC approach was performed. In this way, the local strains obtained at each loading step represent the total accumulated local strains at the latter acquisition.

In this section methodologies to extract DVC data provided by Turunen et al. are described.

4.5.1 Data extraction from DVC

The DVC procedure provides the displacement fields by tracking the translation of small sub-volumes (i.e., correlation windows, CW) between two subsequent loading steps. Displacements maps were derived over a regular grid with a node spacing (NS) corresponding to 10, 7 and 5 voxels according to the type of data (High resolution, downscaled by 4 and downscaled by 8 data).

For every four close nodes, we have a strain which is calculated ideally in the center of the square represented by those four nodes. Therefore, known displacement coordinates from Turunen et al., the corresponding strain coordinates are calculated as the average between x coordinates of the previous node and the following one for x-coordinate, as the average between y coordinates of the previous node and the following one for y-coordinate and as the average between z coordinates of the previous node and the following one for z-coordinate, accounting for the NS of each type of data. So, this procedure was repeated for all the provided data.

Instead, the displacements are evaluated in the nodes of the grid (red dots in fig. 4.12) and their coordinates were provided by Turunen et al. [1].

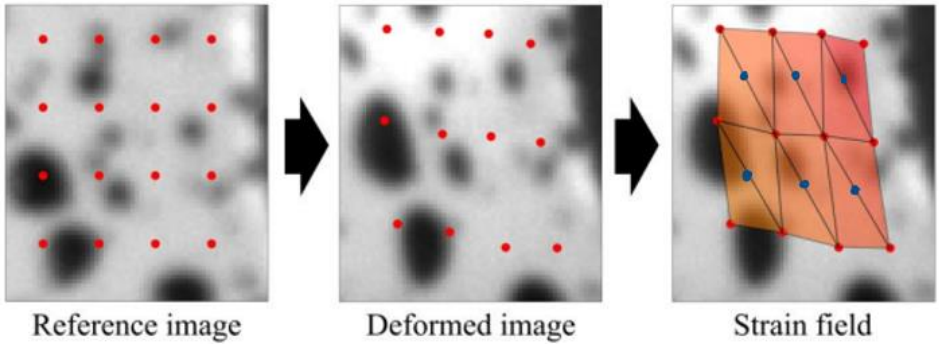

Figure 4.12. Grid of regularly spaced nodes (red dots) where displacements are calculated. To obtain strains from the resulting displacement field, grid of nodes can be turned into triangles. Blue dots are the nodes where strain coordinates are evaluated. Image adapted from Kok 2021.

From the provided data, stacks of DVC displacements and strains for each load step of the experiment were extracted (fig. 4.13). The edges of the images return high values of displacements and strains which are not realistic. So, the analysis was carried out by removing those parts to avoid boundary effects.

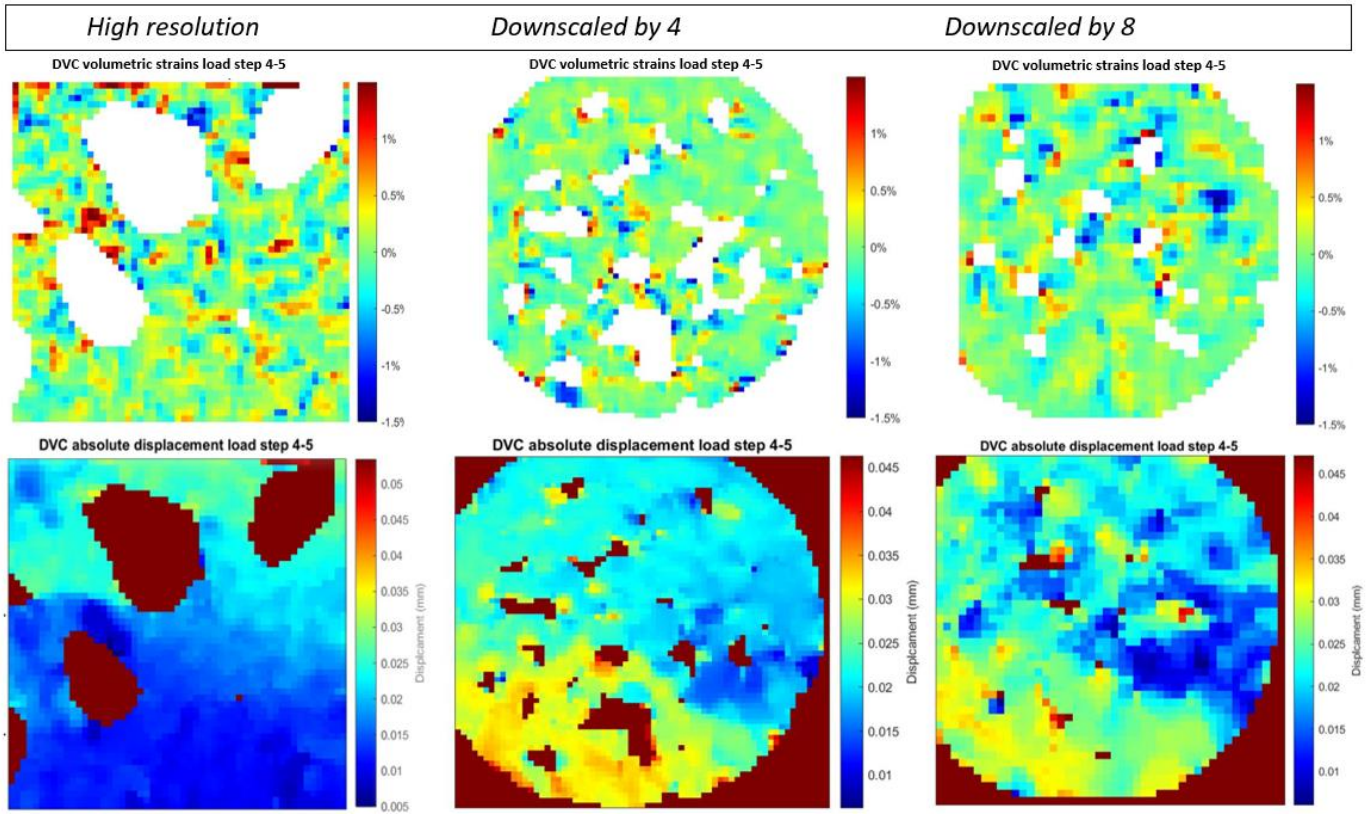

Figure 4.13. Digital volume correlation volumetric strains and absolute displacements for three levels of resolution

4.5.2 Validation procedure

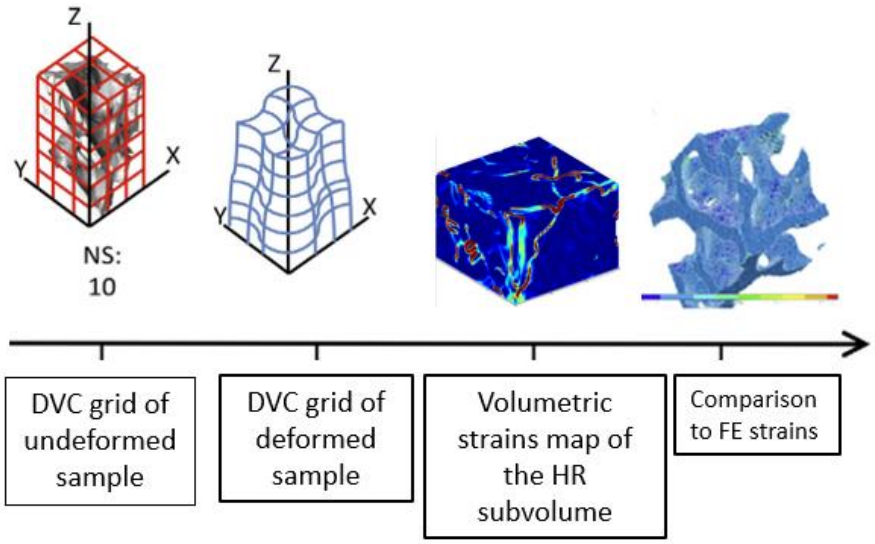

Figure 4.14. Workflow of validation procedure

To compare experimental and numerical data, a quantitative analysis point-by-point is desirable. This means that for each element of the FE model, the corresponding DVC strain value is needed and for each node of the FE model the corresponding DVC displacement value as well. If this happens, experimental and numerical data are in a 1:1 relationship and the comparison is possible.

Since voxel size for each type of provided data is bigger than FE element size and the spatial resolution is lower than the FE model one (i.e., DVC nodes are less than the number of elements of the mesh), direct comparison between the two groups of data is not feasible. Literature reveals a wide use of interpolation methods as approach to validate models [29],[30],[31]. Therefore, a linear interpolation of DVC data to the centroids of the elements of the μFE model and to the nodes of the elements was performed. In this way, a DVC value of strain or displacement is related to the corresponding value predicted by μFE model.

Before applying interpolation method to the FE centroids or nodes, the effective efficacy of the method was verified. Interpolation was performed on a tightened grid of points corresponding to the DVC coordinates. In this case tightening the grid means that an intermediate point between two was added.

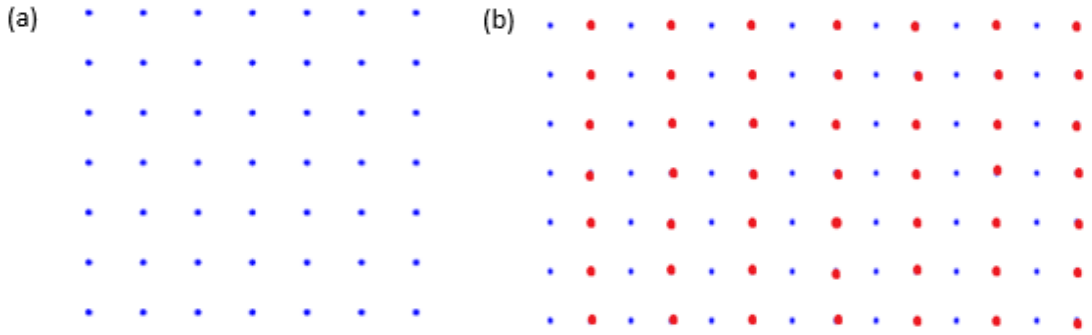

Figure 4.15. Original (a) and tightened (b)

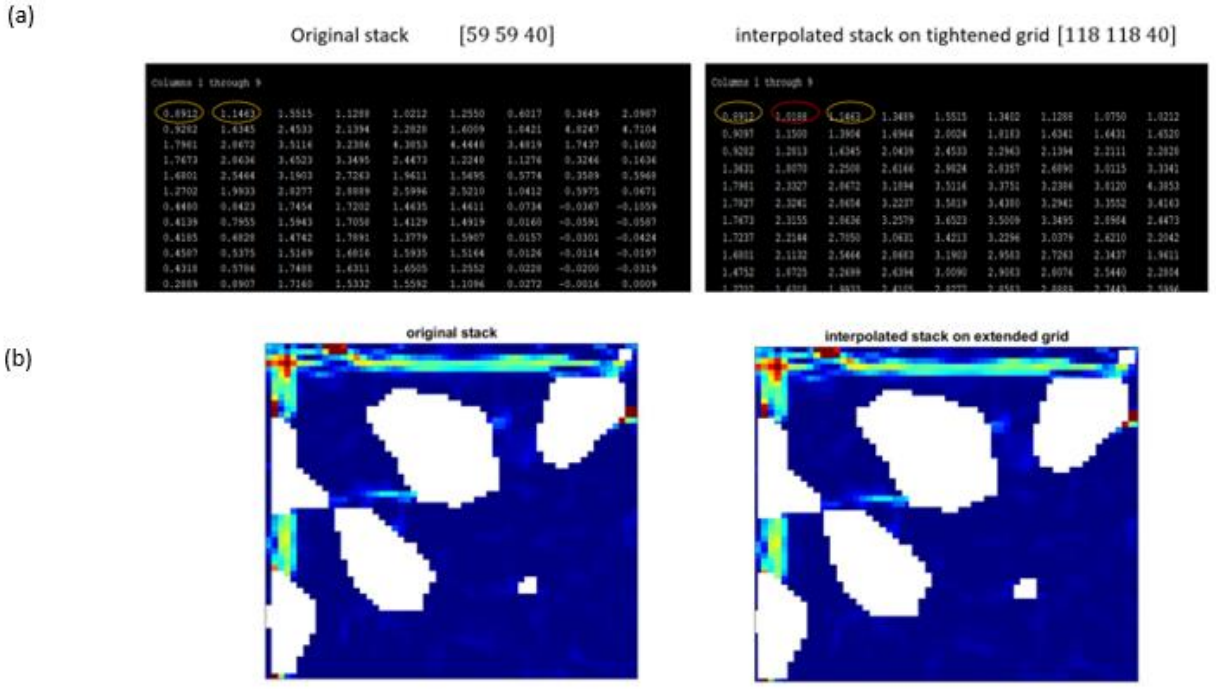

Figure 4.16. Interpolation results in terms of grid (a) and in images (b).

The figure 4.16 shows on the left the original stack of DVC data while on the right the interpolation result on the tightened grid. This confirmed that interpolation method works quite well. In this scenario, interpolation to FE centroids and nodes was performed. To ensure interpolation is applied to the right points, a comparison between the position of the DVC nodes in the grid and the centroids of FE model was carried out (fig. 4.17).

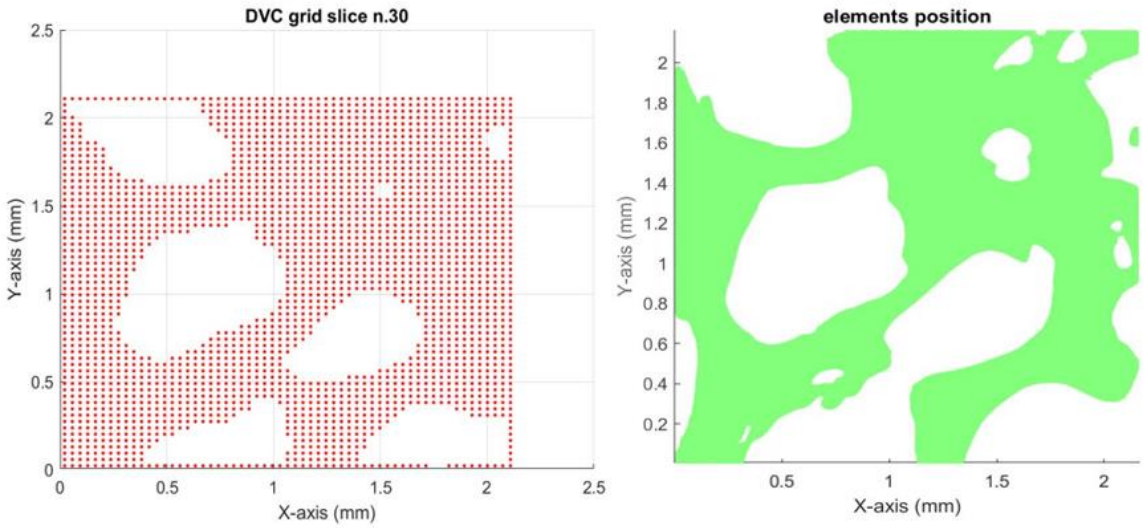

Figure 4.17. DVC nodes grid and corresponding elements on µFE

4.6 Statistics

Comparisons between DVC-measured and FE-predicted displacements and strains were also performed using a linear regression analysis. Determination coefficient (R2), slope and intercept of the regression, the Root mean square error (RMSE), the RMSE divided by the maximum experiment value (RMSE%), the largest difference between microFE prediction and DVC measurements (Max.error) were computed.

Chapter 5

Results

This chapter reports the results obtained during this thesis work using the methodologies described in chapter 4.

5.1 Convergence analysis

The convergence study was performed on a region of interest (ROI) of the sub-volume model from high-resolution data (section 4.4). This was because both Turunen et al. [1] and the present work focused on strain distribution and its evolution during the loading in the regions where cracks were appearing. The maximum absolute volumetric strain and the maximum major principal strain were considered as the parameters to look at for the convergence analysis (Table 5.1-5.2). The maximum value of volumetric and major principal strain among the strains of the selected elements (i.e., the elements of the ROI) was computed for each mesh. In this way percent error between consecutive refinements could be evaluated.

Based on the convergence criterion according to which convergence is reached when two consecutive mesh refinements differ less than 2% (Table 5.1 and 5.2), the tenth mesh was considered to have reached-convergence and was hence used for the remainder of the study. The “converged” mesh was composed by 2’500’000 elements which resulted in a highly refined mesh, but with high computational cost.

MESH	absolute volumetric strain max	error (%)	n.elements
1	0.086		16541
2	0.092	6.02	36707
3	0.089	3.02	73224
4	0.083	6.86	141251
5	0.119	29.79	259606
6	0.134	10.98	459697
7	0.179	25.25	645690
8	0.192	7.13	1332450
9	0.175	9.95	2000000
10	0.172	1.74	2500000
11	0.171	0.66	2743530

Table 5.1. Maximum absolute volumetric strain, percentual error and number of elements for each analysed mesh. Percentual error was obtained by dividing the difference between the maximum absolute volumetric strain between consecutive mesh refinements by the previous mesh refinement.

MESH	major principal strain max	error (%)	n.elements
1	0.078		16541
2	0.090	13.9	36707
3	0.085	6.66	73224
4	0.089	4.82	141251
5	0.098	8.95	259606
6	0.082	18.8	459697
7	0.134	38.9	645690
8	0.141	4.91	1332450
9	0.140	1.01	2000000
10	0.139	0.71	2500000
11	0.139	0.11	2743530

Table 5.2. Maximum major principal strain, percentual error and number of elements for each analysed mesh. Percentual error was obtained by dividing the difference between the maximum major principal strain between consecutive mesh refinements by the previous mesh refinement.

As figure 5.1 shows, increasing the number of elements from a mesh to the next one (i.e., reducing the maximum volume and the optimum radius bound – see section 4.4 for more details), the two parameters tend to converge. This means that further mesh refinement produces a negligible change in the solution. If on the one hand a higher number of elements ensures adequate results from simulations and a greater mesh density, on the other it implies much higher computational times.

(a)

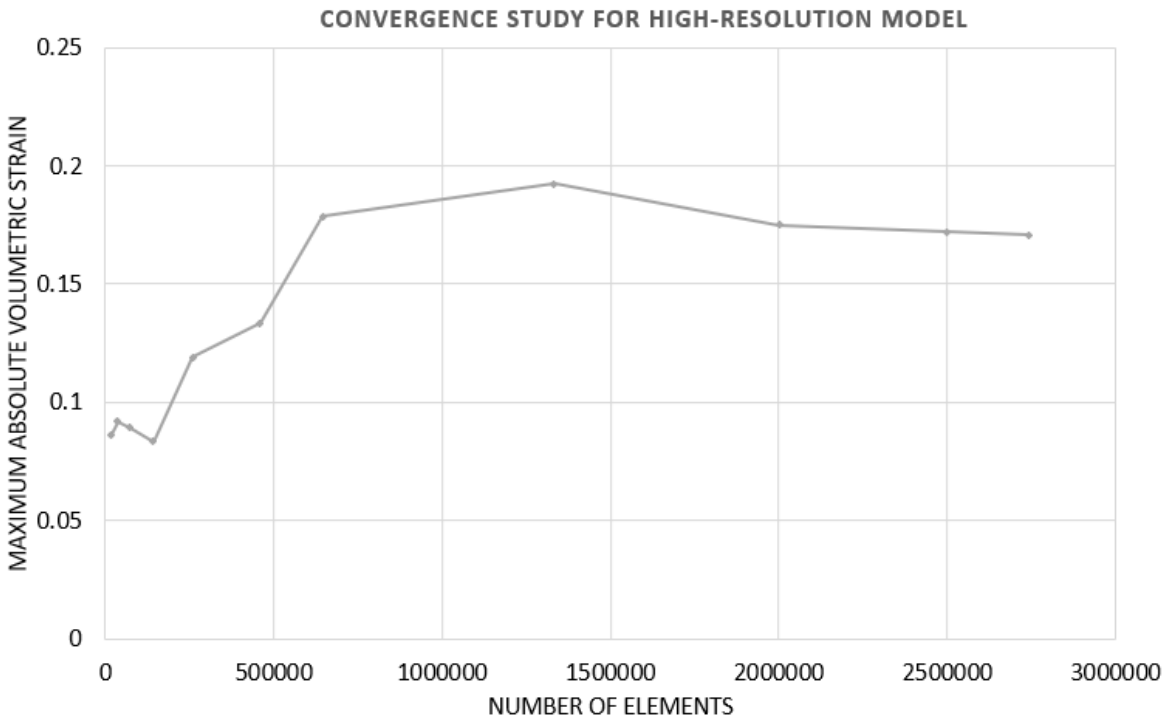

(b)

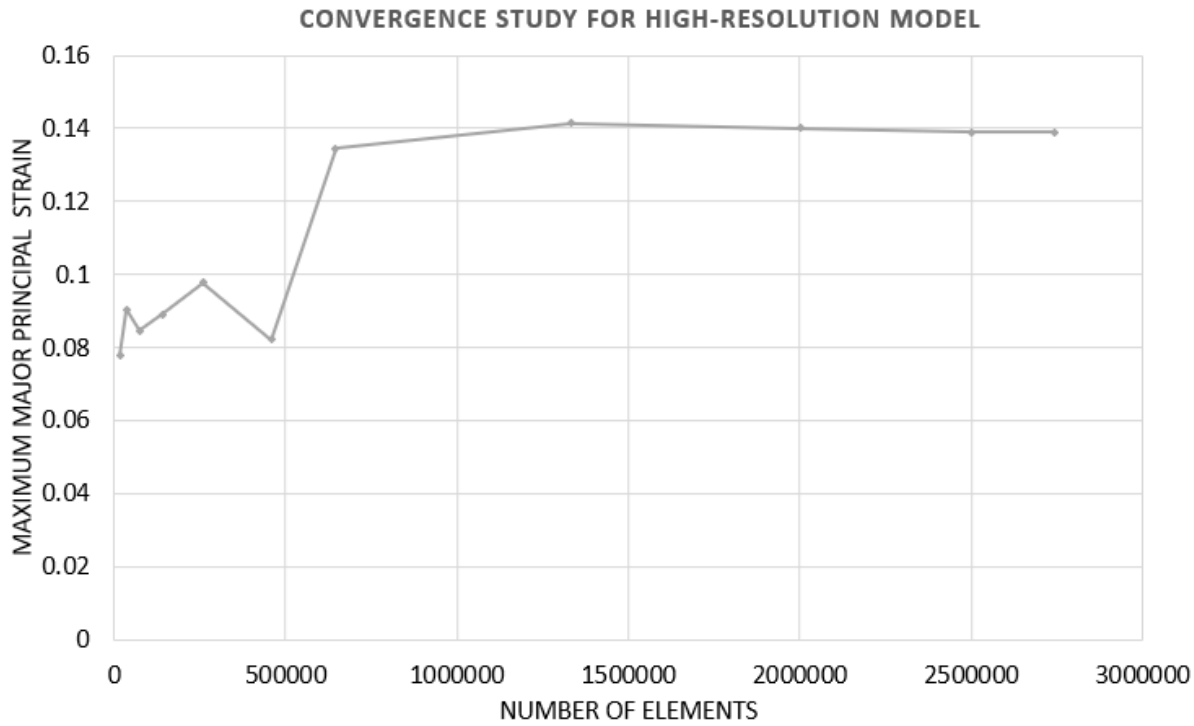

Figure 5.21. Results from convergence study. Maximum major principal (a) and maximum absolute volumetric strain (b) vs. number of elements for high-resolution model.

Once the appropriate mesh was found, considerations about mesh quality and distribution of elements volume were carried out. The results of the analysis of the mesh quality and of the distribution of elements volume are shown in the following histograms (fig. 5.2).

Mesh elements are not distorted or stretched since the aspect ratio was found to be close to 1 (fig. 5.2a). Therefore, a good quality is ensured because a factor close or equal to 1 means that elements keep their shape, and they are not distorted. Moreover, a uniform distribution of elements volume was reached. Most of the elements have a similar volume with a peak around 10^{-6} mm^3 and elements with a volume equal to 0 mm^3 or with a negative volume were not found (fig. 5.2b).

(a)

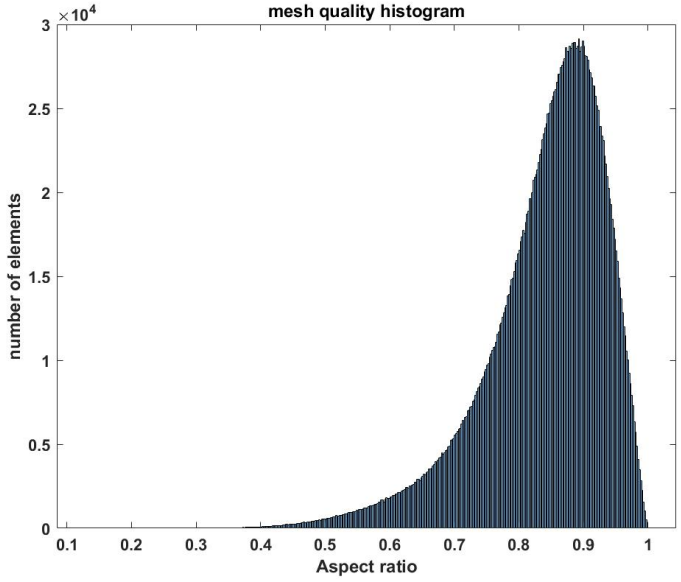

(b)

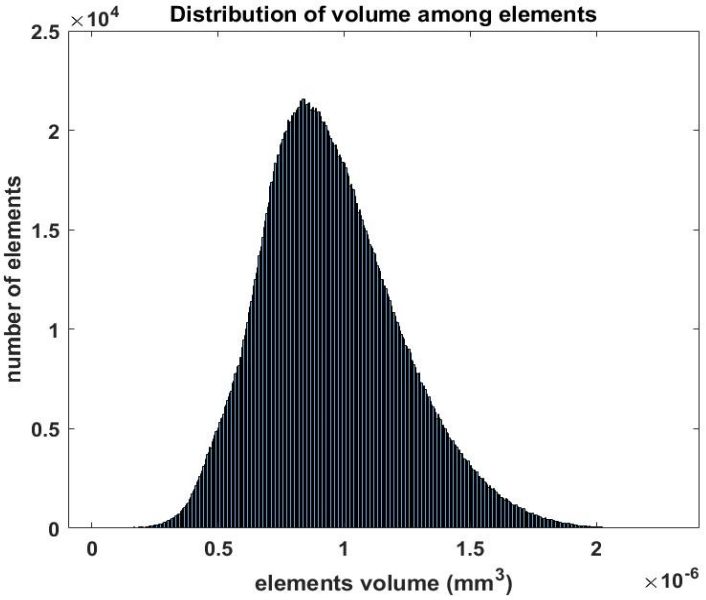

Figure 5.2. Histograms of mesh quality (a) and elements volume distribution (b)

5.2 µFE Models

Mesh models for three different levels of resolution are shown in fig. 5.3. Mesh from downscaled by 4 data results in 771404 elements and the one from downscaled by 8 data in 108201 elements (fig. 5.3).

(a)

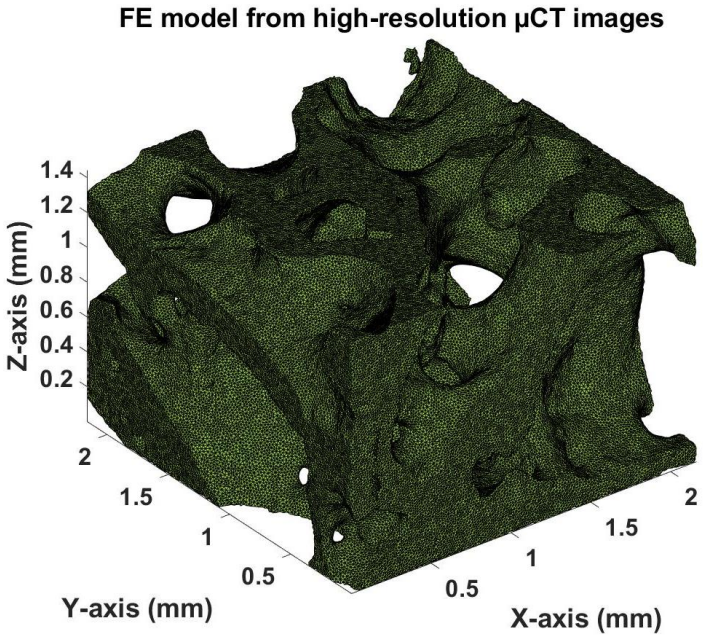

(b)

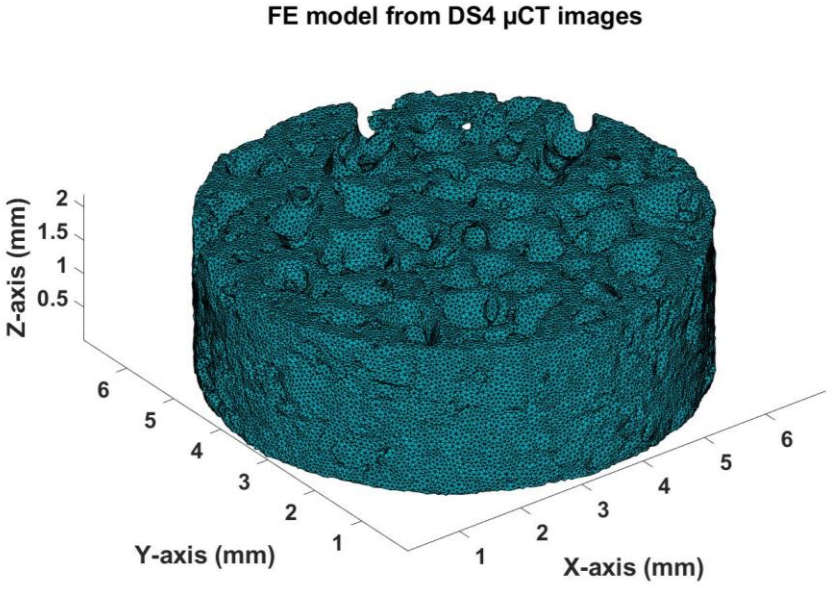

(c)

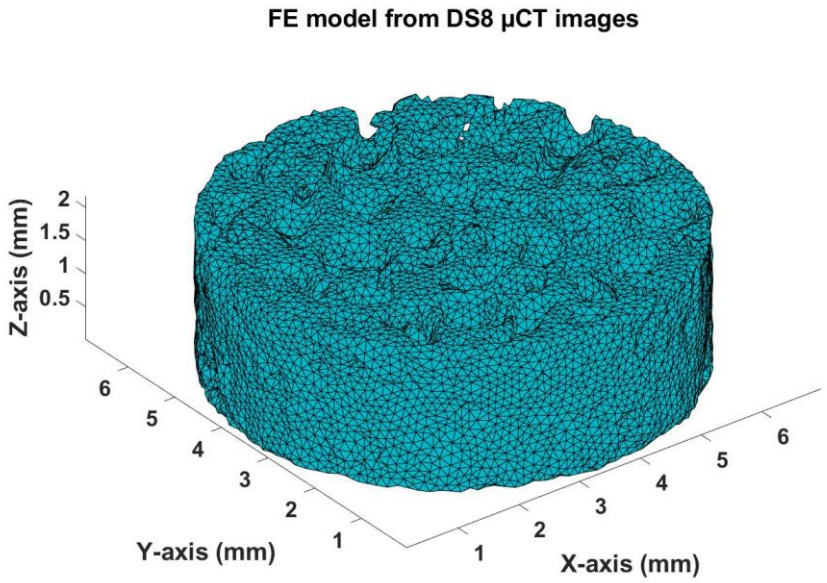

Figure 5.3. µFE models for high-resolution data (a), downscaled by 4 factor data (b) and downscaled by 8 factor data (c). Mesh models from downscaled by 4 and 8 µCT images were created by using the same set of parameters (opt. radius bound, distance bound, maximum volume) chosen for the high-resolution model.

5.3 Simulations

To define the importance of BCs, both simple and confined compression for the high-resolution model were compared. The findings indicate that the two different BCs do not greatly affect strain values (mean difference between major principal strain values from simple and confined compression 0.00086±0.002). Moreover, similar distributions were observed (fig. 5.4) where cracks appear. With regards to displacement fields, same considerations can be done (mean difference 0.00077± 0.00099 mm).

(a)

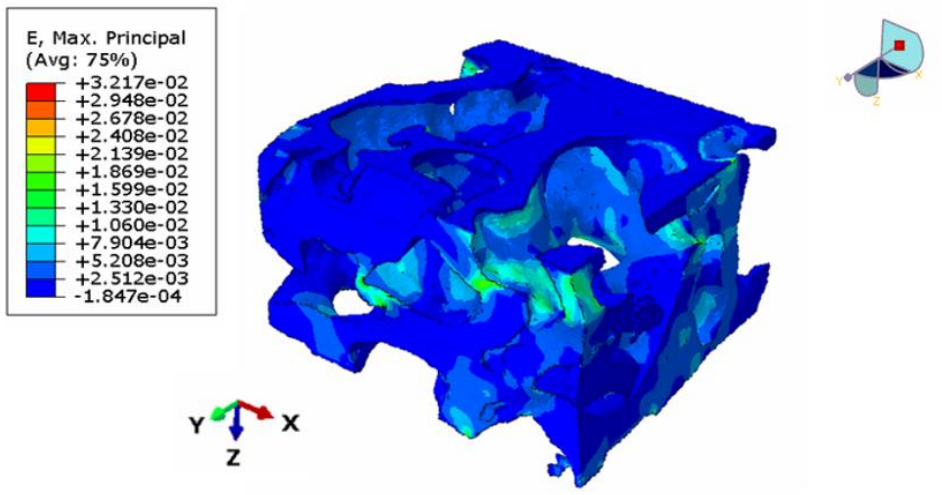

(b)

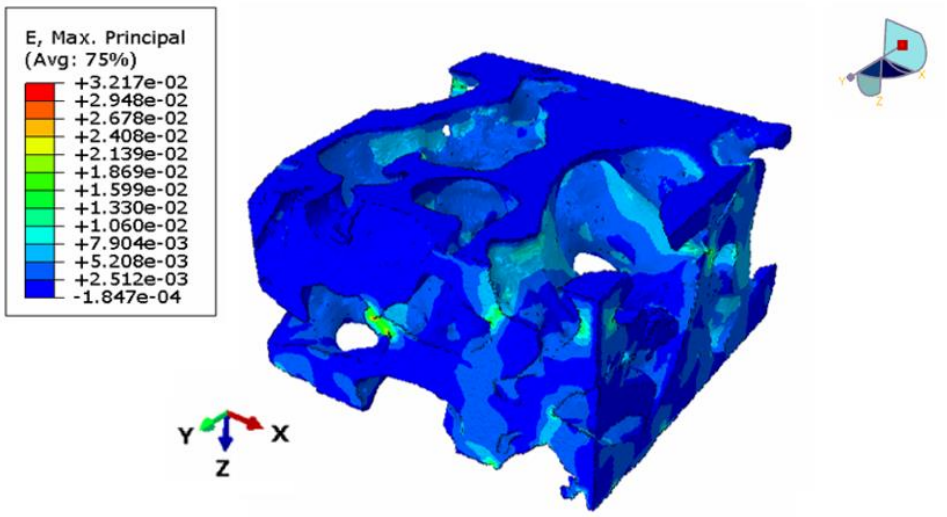

Figure 5.4. Major principal strain distributions in simple (a) and confined (b) compression for load step 5. Deformed configuration is shown.

(a)

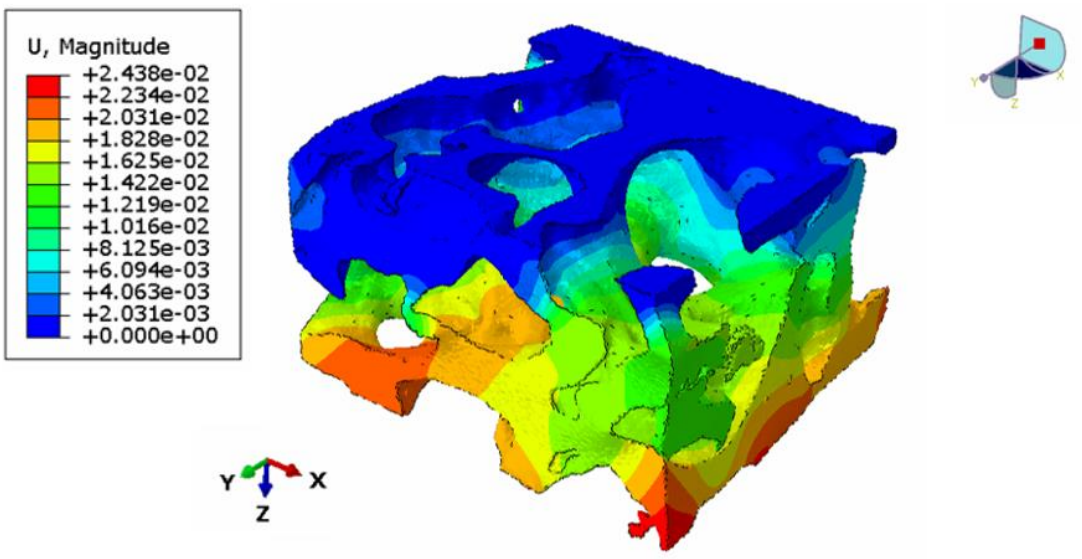

(b)

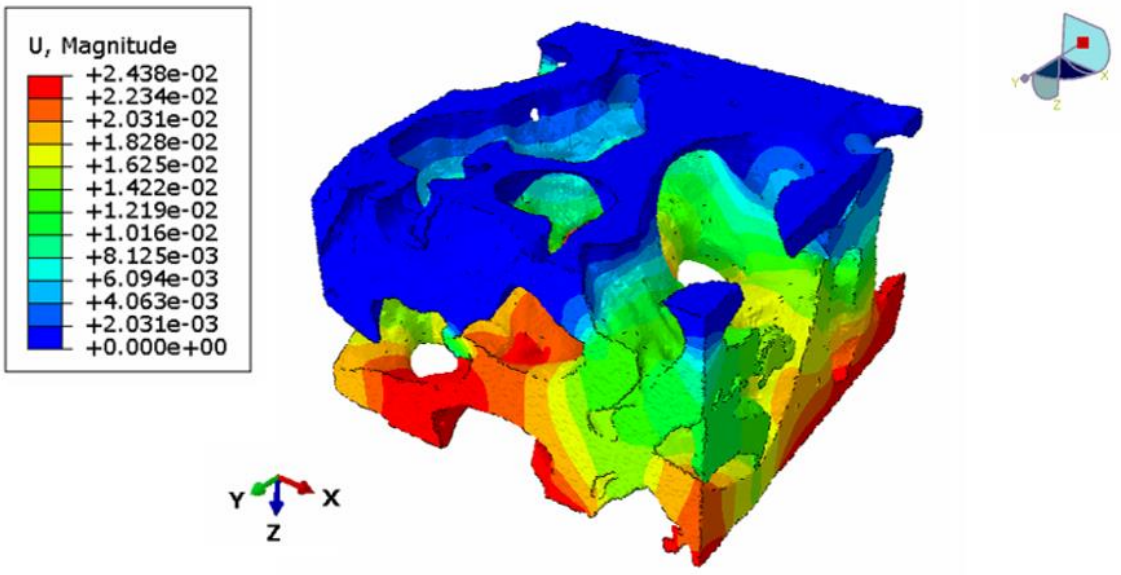

Figure 5.5. Absolute displacement distributions in simple (a) and confined (b) compression for load step 5. Deformed configuration is shown.

(a)

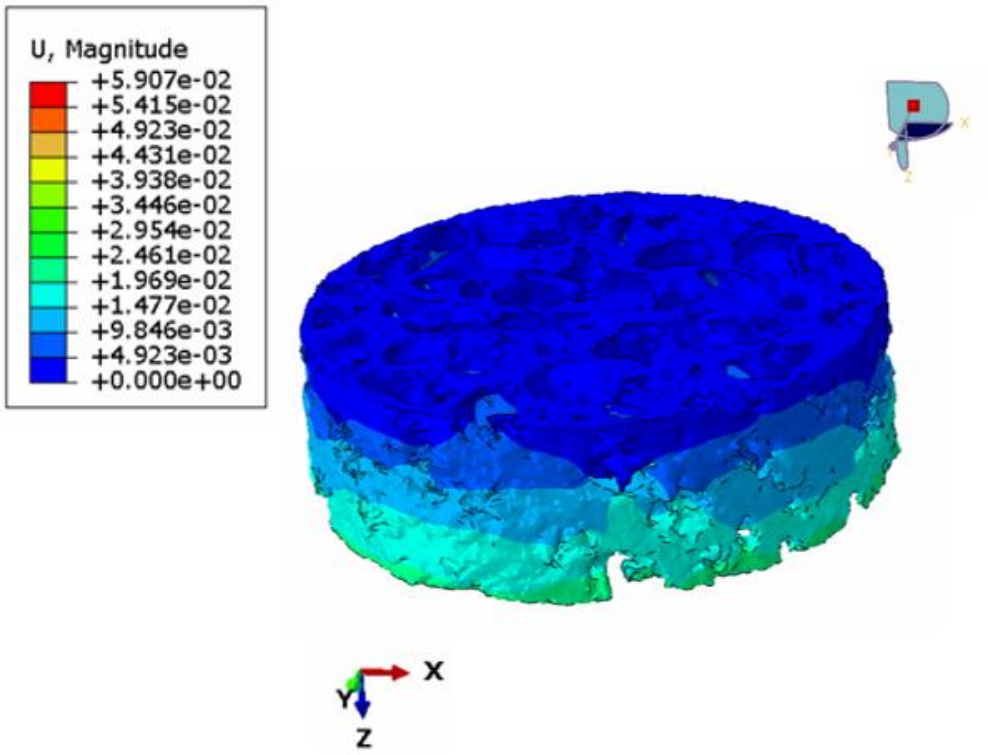

(b)

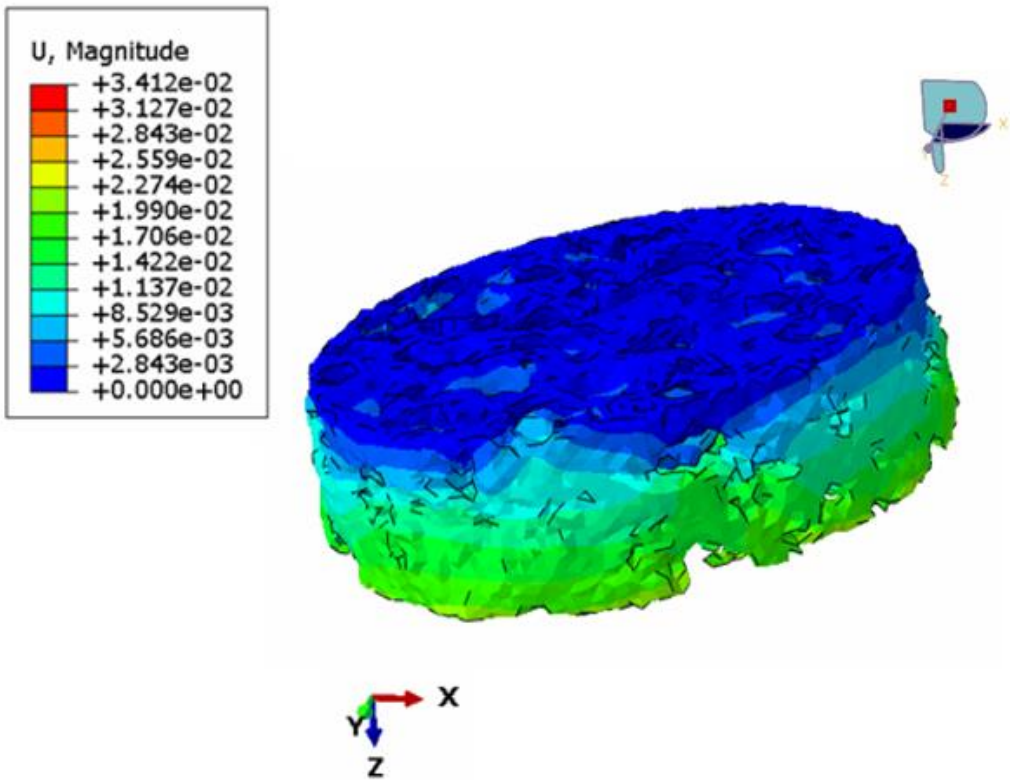

Figure 5.6. Absolute displacement distributions in downscaled by 4 (a) and downscaled by 8 (b) data for load step 5. Deformed configuration is shown.

(a)

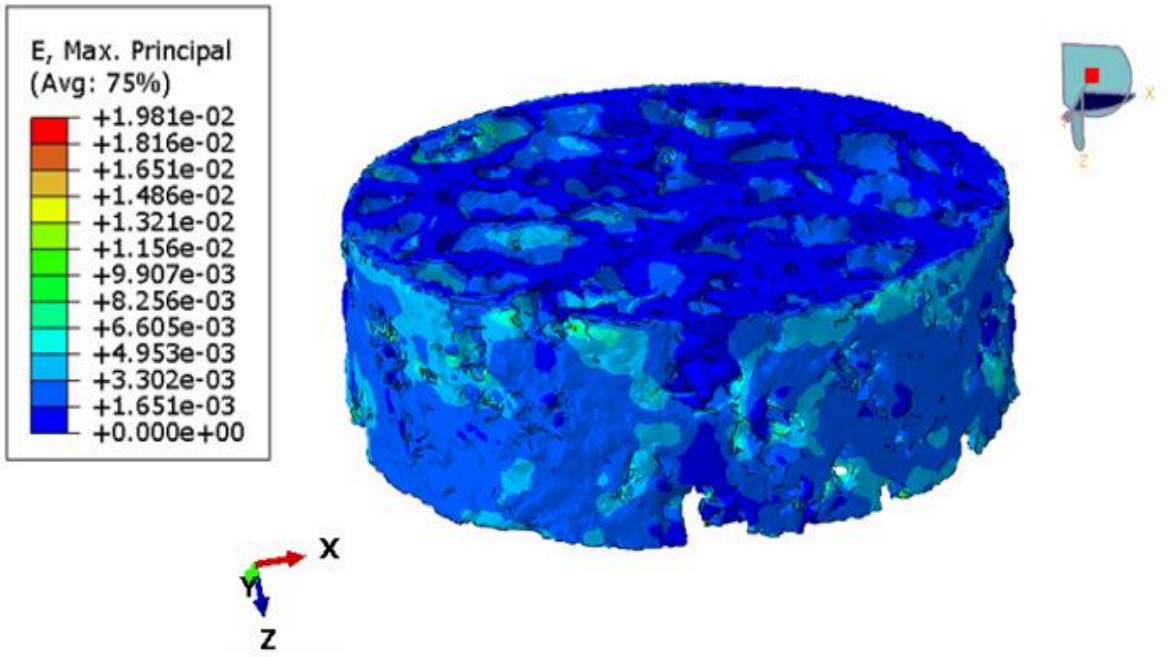

(b)

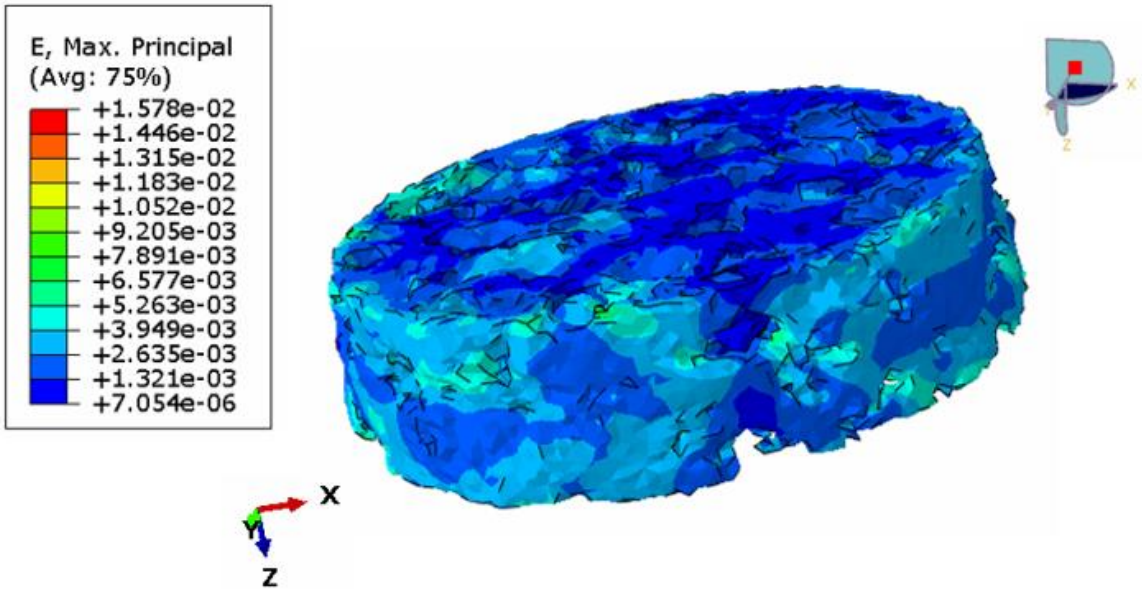

Figure 5.7. Major principal strain distributions in downscaled by 4 (a) and downscaled by 8 (b) data for load step 5. Deformed configuration is shown.

5.4 Validation of the micro-FE model

In this section, the results for the validation of the micro-FE model are presented. The validation included a first qualitative comparison between DVC maps and interpolated values on FE centroids to show how interpolation method works and a comparison with experimental DVC data for high-resolution and downscaled micro-FE predicted values.

5.4.1 Validation procedure

To show that the interpolation procedure worked well, visual comparison between original DVC strain stacks from the provided material and interpolated values is reported (fig.5.9). The comparison for the other levels of resolution can be found in the Appendix.

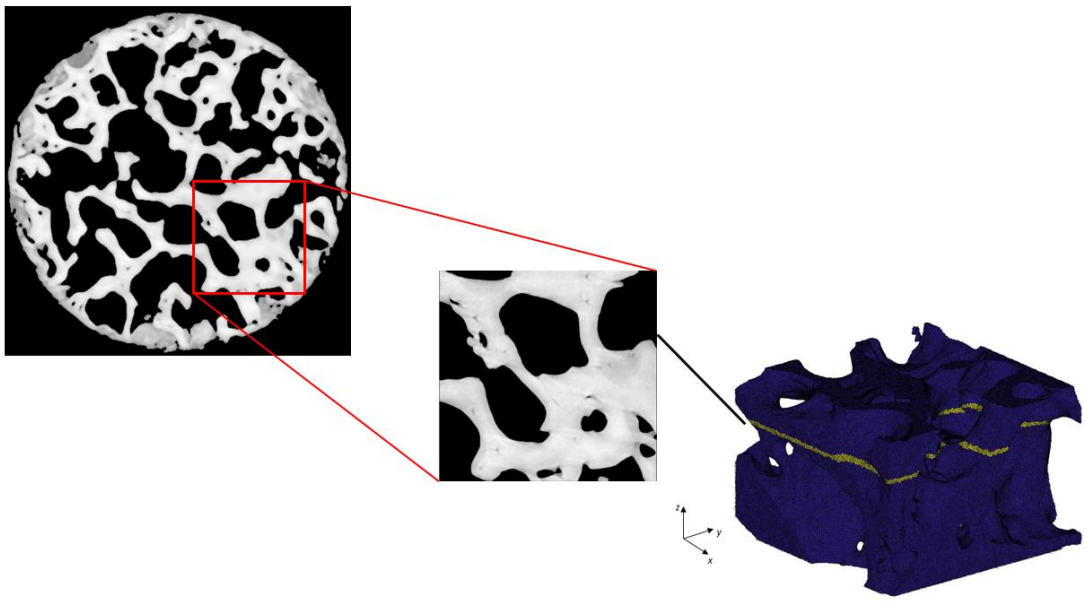

Figure 5.8. The region used for comparison is a section of xy planes at as a specific height along the trabecular bone and FE model. The geometry of the bone is cut out along the 'xy' plane at different height 'z', here z is used to represent the height of the trabecular bone sample. A slice at z=1.08 mm was picked up inside the FE model and it is shown. This value of height was chosen according to the analysed slice in Turunen et al. work [1]. The red square on the μCT image shows the region of interest from the whole sample.

By visual inspection, the mapped volumetric strains showed similar pattern as the original data from DVC. This suggested that the validation procedure could proceed and that a detailed comparison was possible. Nevertheless, noise as well as movement artefacts and other experimental limitations of the bone plug during the experiment are responsible for the spots visible in the maps: red spots, which indicate tensile regions, are immediately close to blue spots, which indicate compressive regions (fig. 5.9). This random distribution is not reasonable, and it might be explained only accounting for the two aspects mentioned above.

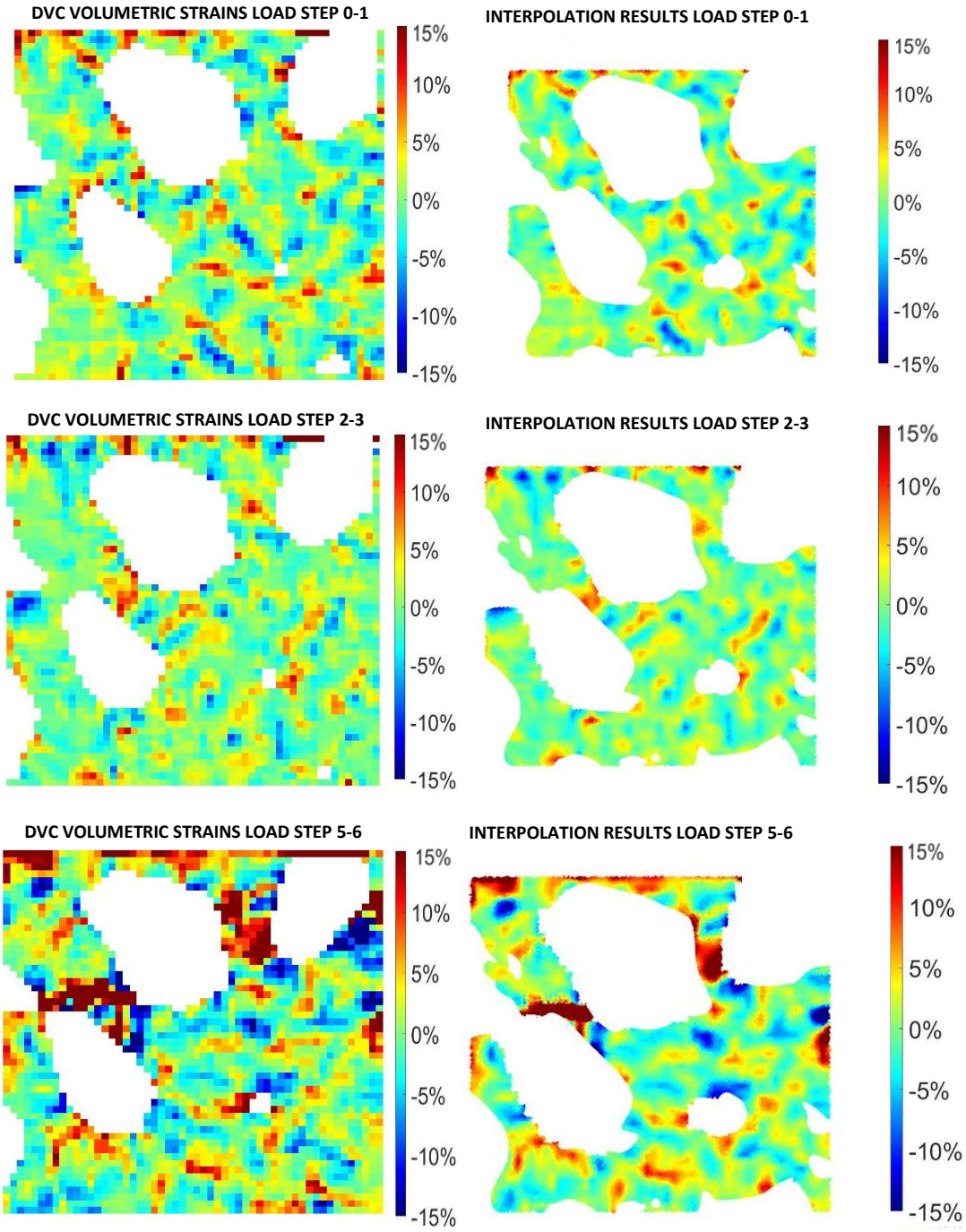

Figure 5.9. Volumetric strain maps from Digital Volume Correlation of high-resolution data (left) compared to the interpolated values to FE centroids (right) for load step 1, 3 and 6 respectively.

The FE predictions for the three levels of resolution were compared in terms of volumetric strain and displacement to the available experimental data. The comparison of the results was performed with the interpolated values in the centroids of the elements of the μFE model and in the nodes of the elements respectively.

In particular, the volumetric strain maps are plotted for two load steps, load step 1-2 and load step 4-5. The load step 4-5 gives the volumetric strains in the bone before global failure, while load step 1-2 is selected after the start of the compression test [1]. Both selected load steps are in the linear elastic region of the stress-strain curve (fig.5.10).

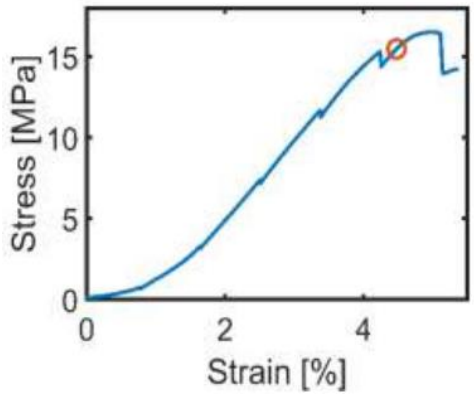

Figure 5.10. Stress-strain compressive loading curve until ultimate stress. The drops observed in the curve are due to the relaxation of the sample while stopping the loading during imaging. Open circle indicates the yield point which corresponds to the bone global failure at load step 6 [1].

The visual inspection for volumetric strain maps for both experimental and computational cases is shown in figure 5.11. Simple and confined compression maps were inspected to see which of the two situations was closer to the real one (i.e., experiment). In all these maps volumetric strains have negative values since some regions of the trabecular sub-volume were compressed during the experiment. Even though the pattern showed by μFE model was quite different from the experimental one, the model detected high strain values in those regions which are classified as *"crack regions"* [1]. Moreover, simple and confined compression provided quite similar results both in load step 1-2 (mean difference between volumetric strain values from simple and confined compression 0.0037±0.003) and load step 4-5 (mean difference 0.009±0.0073) even though volumetric strain values in the confined compression were higher (around 2%), as it can be seen in the colormap.

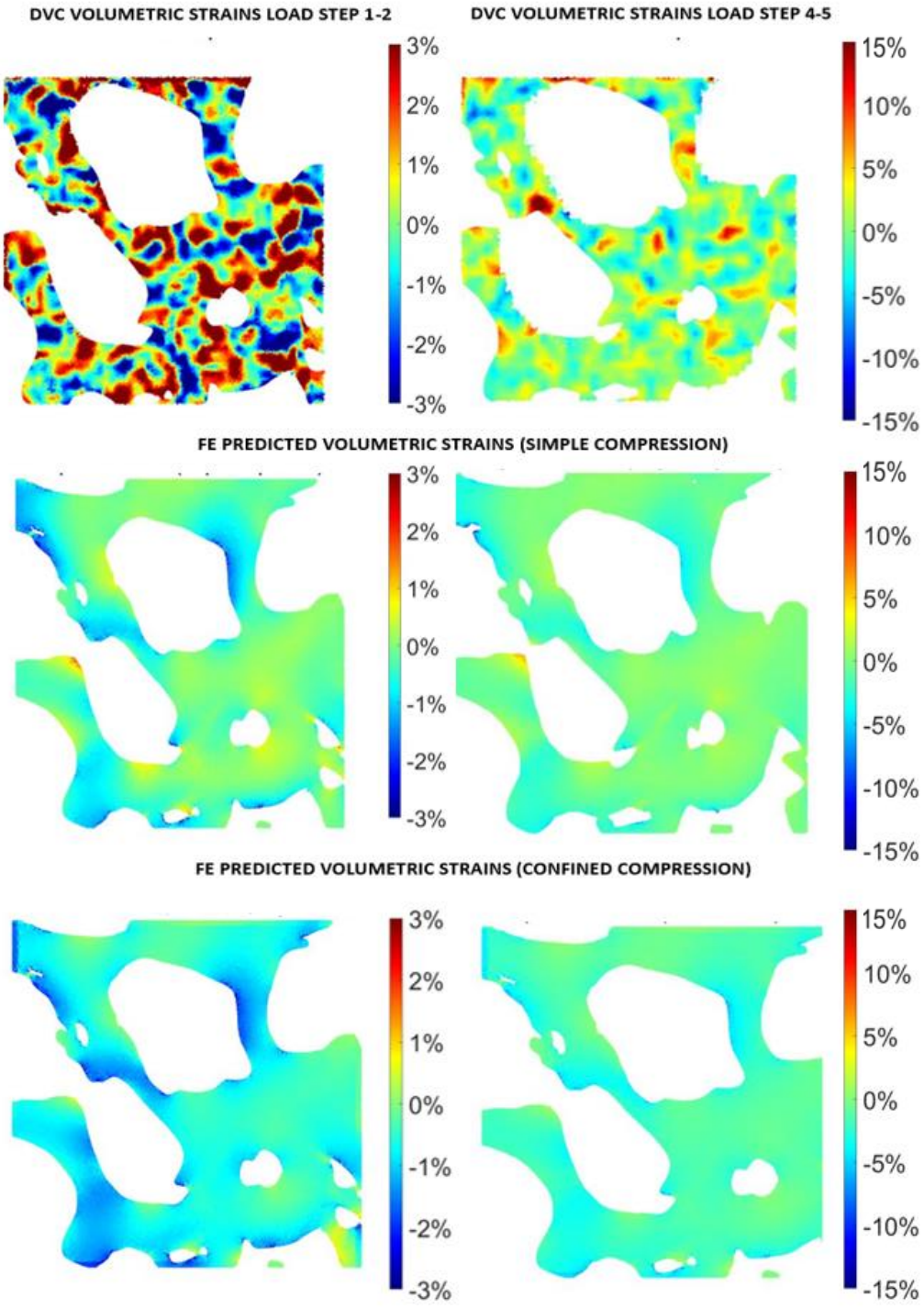

Figure 5.11. DVC volumetric strains interpolated values to FE centroids (top) compared to FE predicted strains in simple (middle) and confined (bottom) compression at z=1.08 mm for load step 1-2 (left column) and load step 4-5 (right column). High-resolution data are shown.

Figure 5.12 and figure 5.13 show the visual inspection and comparison between experimental data from DVC and computational results from μFE model. Downscaled data were analysed and compared to the high-resolution ones. In both downscaled by 4 and 8 cases, noise effects were more visible in load step 2 while decreased in load step 5. Indeed, there was a better visual correspondence between measured and predicted volumetric strains for load step 5 (fig. 5.12, 5.13).

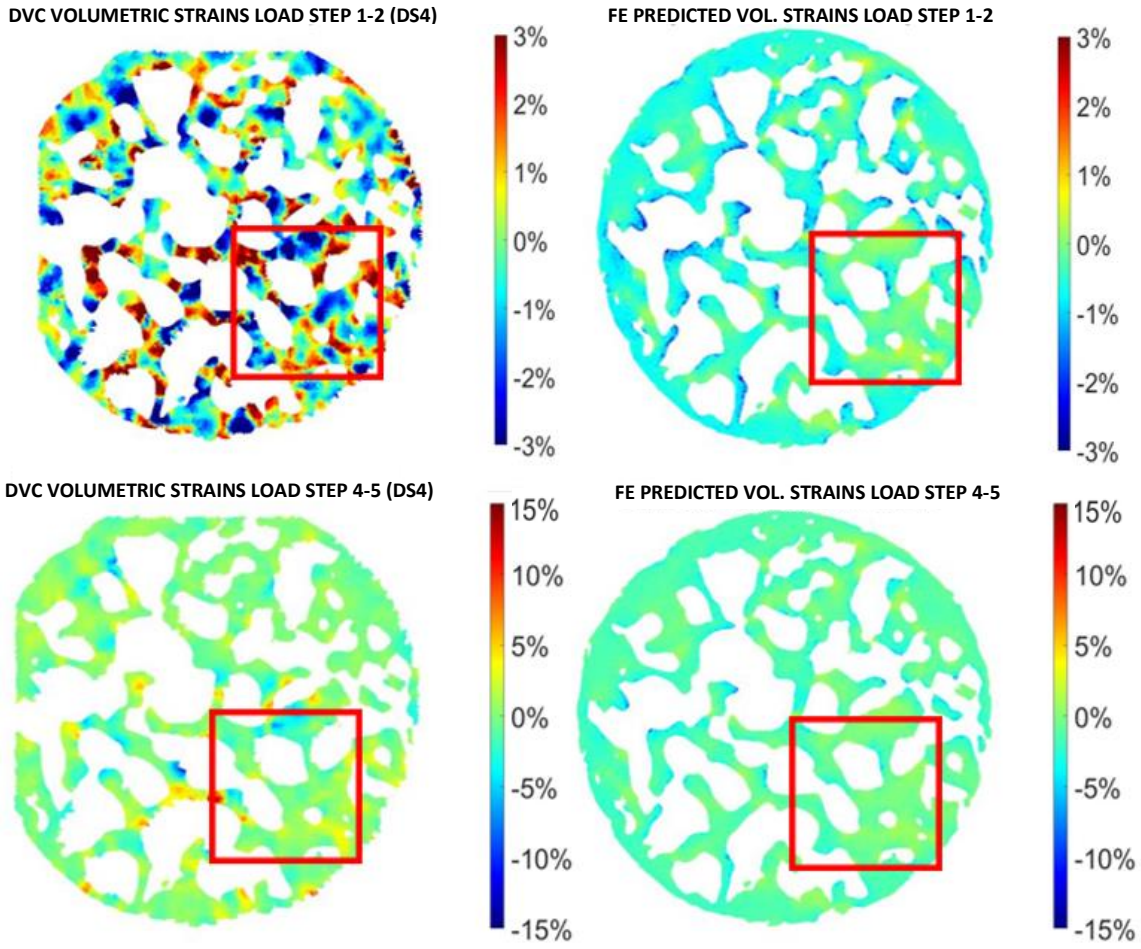

Figure 5.12. DVC volumetric strains interpolated values to FE centroids (left) compared to FE predicted strains (right) for load step 1-2 (top row) and 4-5 (bottom row). Downscaled data by factor 4 at z=1.4 mm is shown. The red square in the whole sample figures shows the sub-volume of the high-resolution DVC.

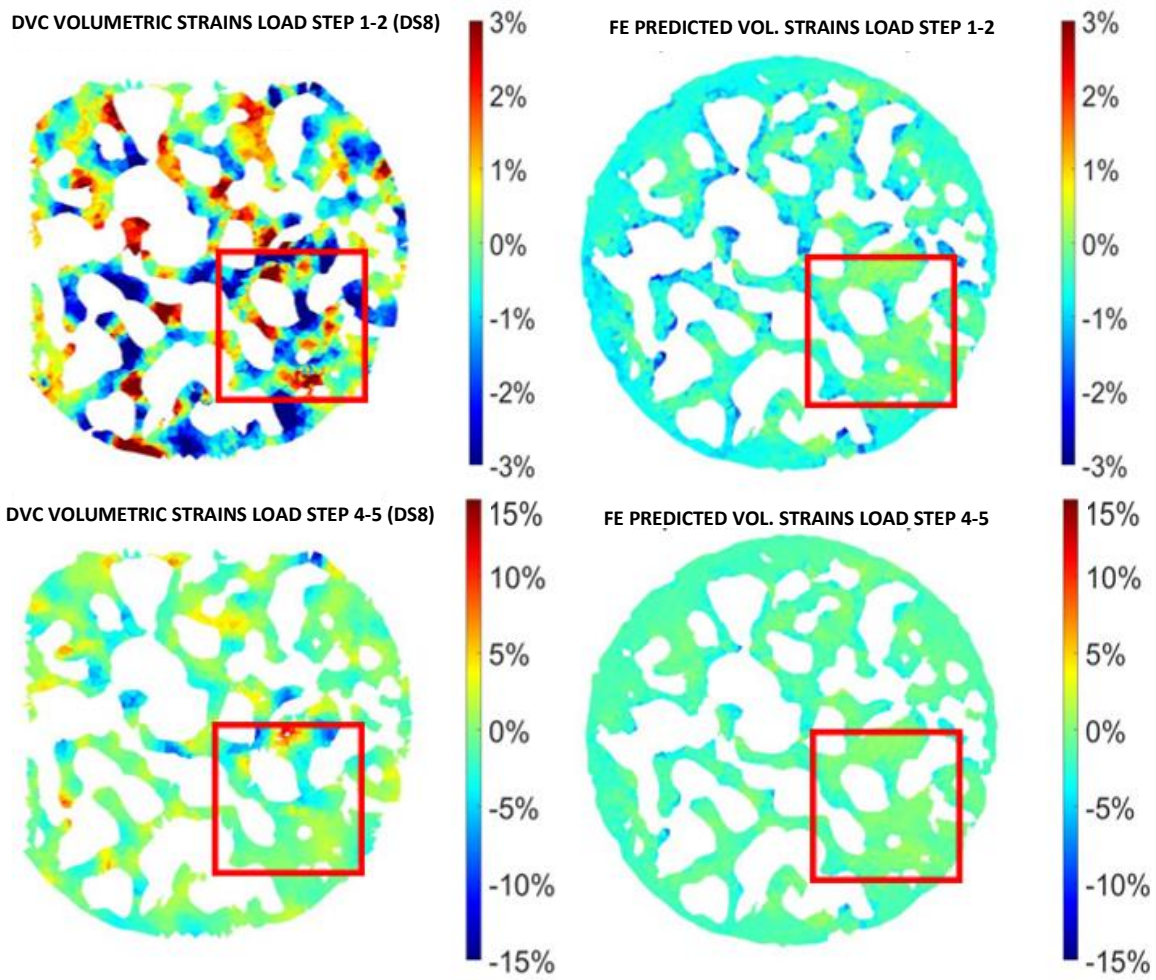

Figure 5.13. DVC volumetric strains interpolated values to FE centroids (left) compared to FE predicted strains (right) for load step 1-2 (top row) and 4-5 (bottom row). Downscaled data by factor 8 is shown. The red square in the whole sample figures shows the sub-volume of the high-resolution DVC.

The same procedure was repeated for displacement maps. Displacement values obtained from μFE model were compared to DVC interpolated values at the nodes of the mesh model so that a 1:1 relationship was obtained. Load steps 1-2 and 4-5 are shown in the figure 5.14. Simple and confined compression maps were inspected to see which of the two situations is closer to the real one (i.e., experiment).

Since comparisons between DVC volumetric strains and FE predicted values did not provide a good visual matching, probably due to the high noise effects, the idea was to validate the μFE model with respect to displacements. Also, this could ensure that BCs were applied properly.

By visual inspection, noise effects seemed to deeply influence volumetric strain maps more than displacement maps since more uniform displacement maps without random spots could be observed (fig. 5.14). This is consistent with strains being the spatial derivative of the displacement.

Nevertheless, by comparing visual results, the predicted pattern did not match properly with the experimental one. Moreover, simple and confined compression showed quite similar maps both in load step 1-2 (mean difference 0.0015± 0.002 mm) and load step 4-5 (mean difference 0.0041 ± 0.0052 mm), so a clear difference between the two sets could not be found.

Similar considerations can be made for absolute displacement maps for downscaled by 4 and 8 data whose images can be found in the Appendix (Fig. A4, A5).

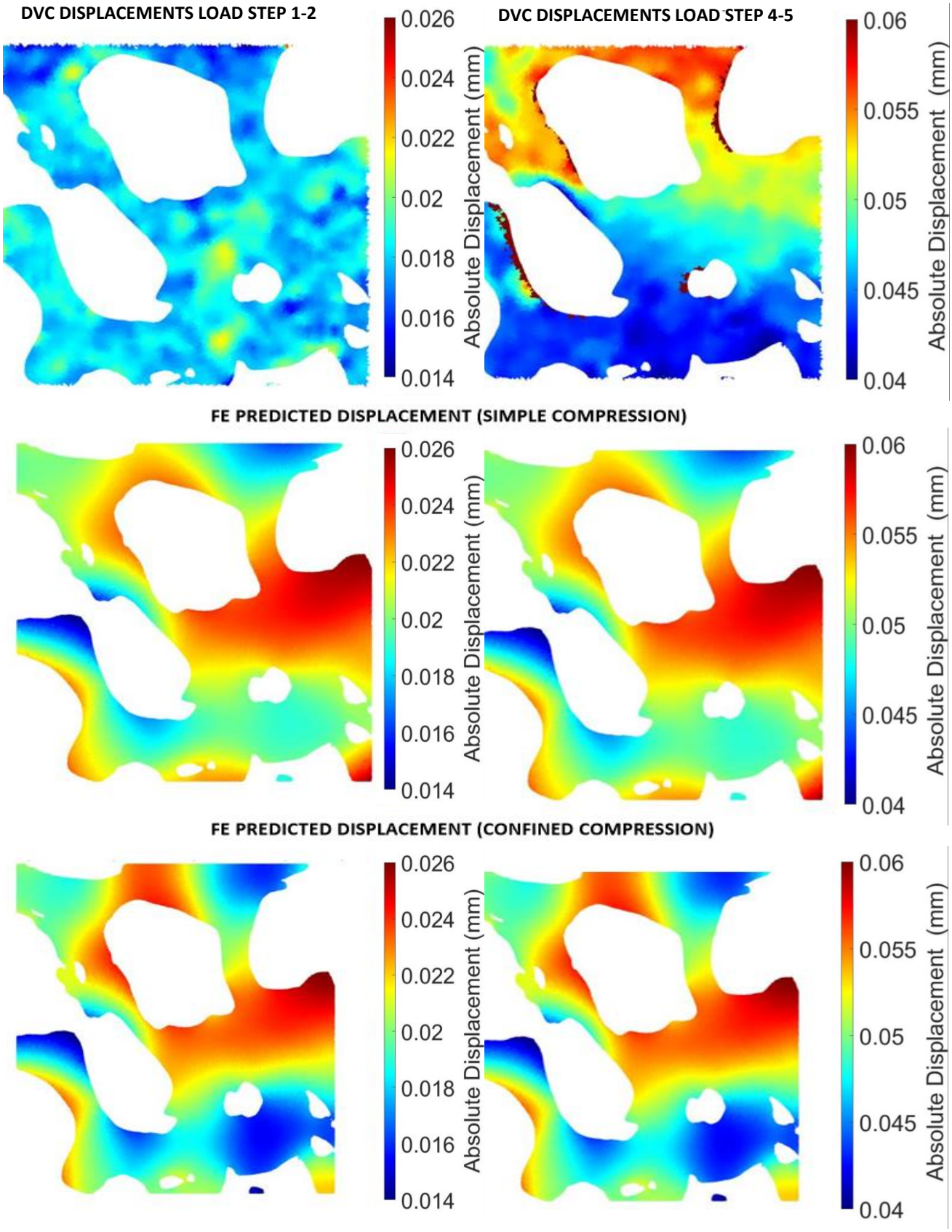

Figure 5.14. DVC absolute displacement interpolated values to FE nodes (top) compared to FE predicted displacements in simple (middle) and confined (bottom) compression at z= 1.08 mm for load step 1-2 (left column) and load step 4-5 (right column).

A further analysis was performed on all displacement components (fig. 5.15).

First, we can observe that noise effects seemed to not influence the displacement maps. Then, a better matching between DVC and μFE was observed for x and z components from high-resolution data in the case of simple compression (fig. 5.15). Simple and confined compression showed similar results along x-direction (mean difference 0.011 ± 0.013 mm), along y-direction (mean difference 0.0055±0.0077 mm) and along z-direction (mean difference 0.00055±0.0022 mm). As can be seen from a visual inspection, both x and z -components from FE model showed a map of displacement in agreement with the experimental one. While a worse matching was observed for y-component: high displacement values predicted by FE model corresponded with low displacement values from DVC maps (fig. 5.15).

Fig. 5.16 and 5.17 show all the displacement components for downscaled data by 4 and 8 respectively. An interesting thing that can be noted is that even in this case a good agreement was found for two displacement components: visually, x and y-components predicted by μFE model in both downscaled by 4 and 8 data showed a similar pattern with respect to DVC maps.

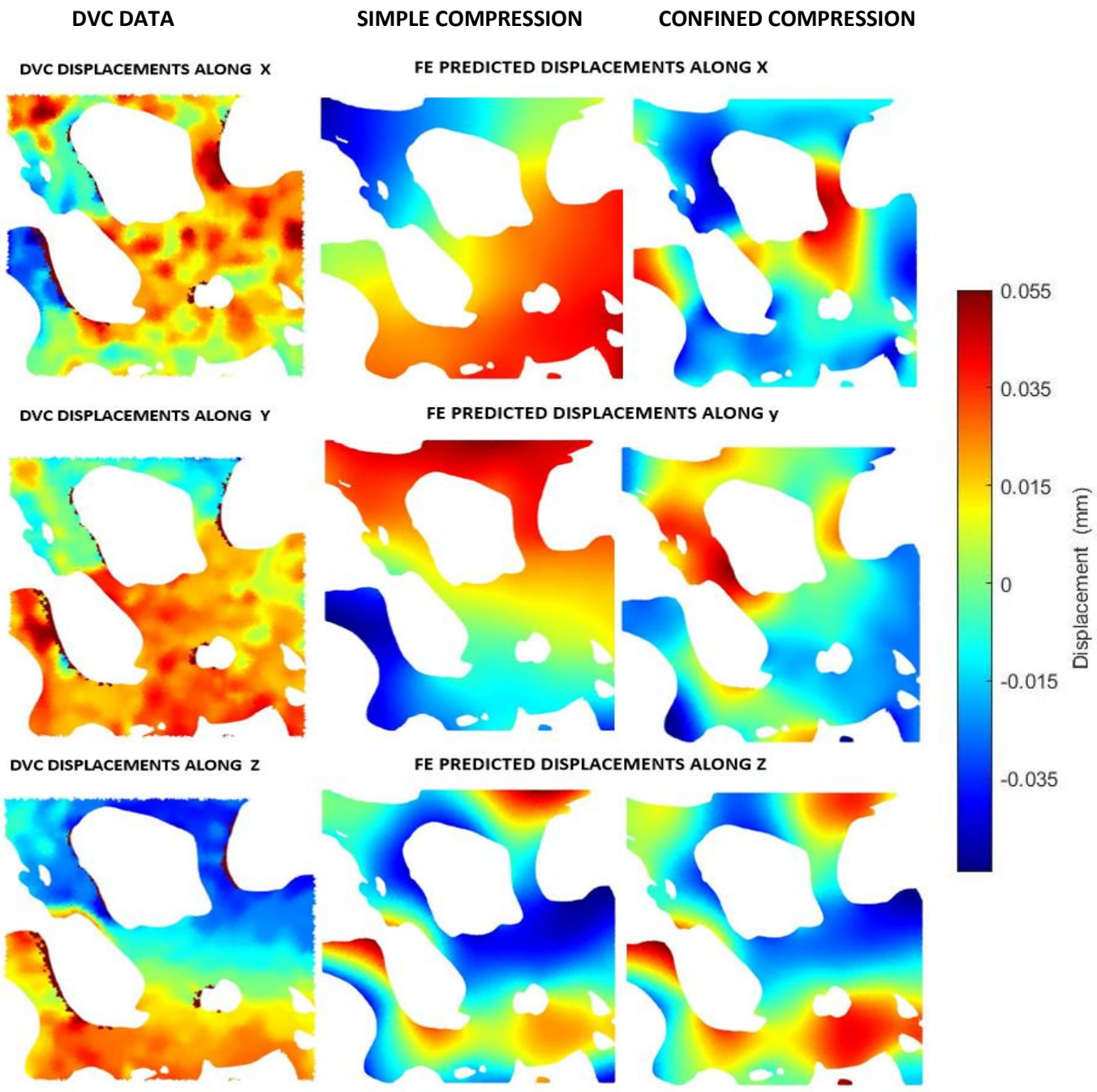

Figure 5.15. Comparisons of displacements from high-resolution DVC data and FE predicted displacements at z=1.08 mm. Row 1, 2, and 3 consists of displacement components x, y and z respectively, while column 1 shows DVC displacements, column 2 and 3 displacements for simple and confined compression respectively predicted by µFE model. Load step 5 is shown.

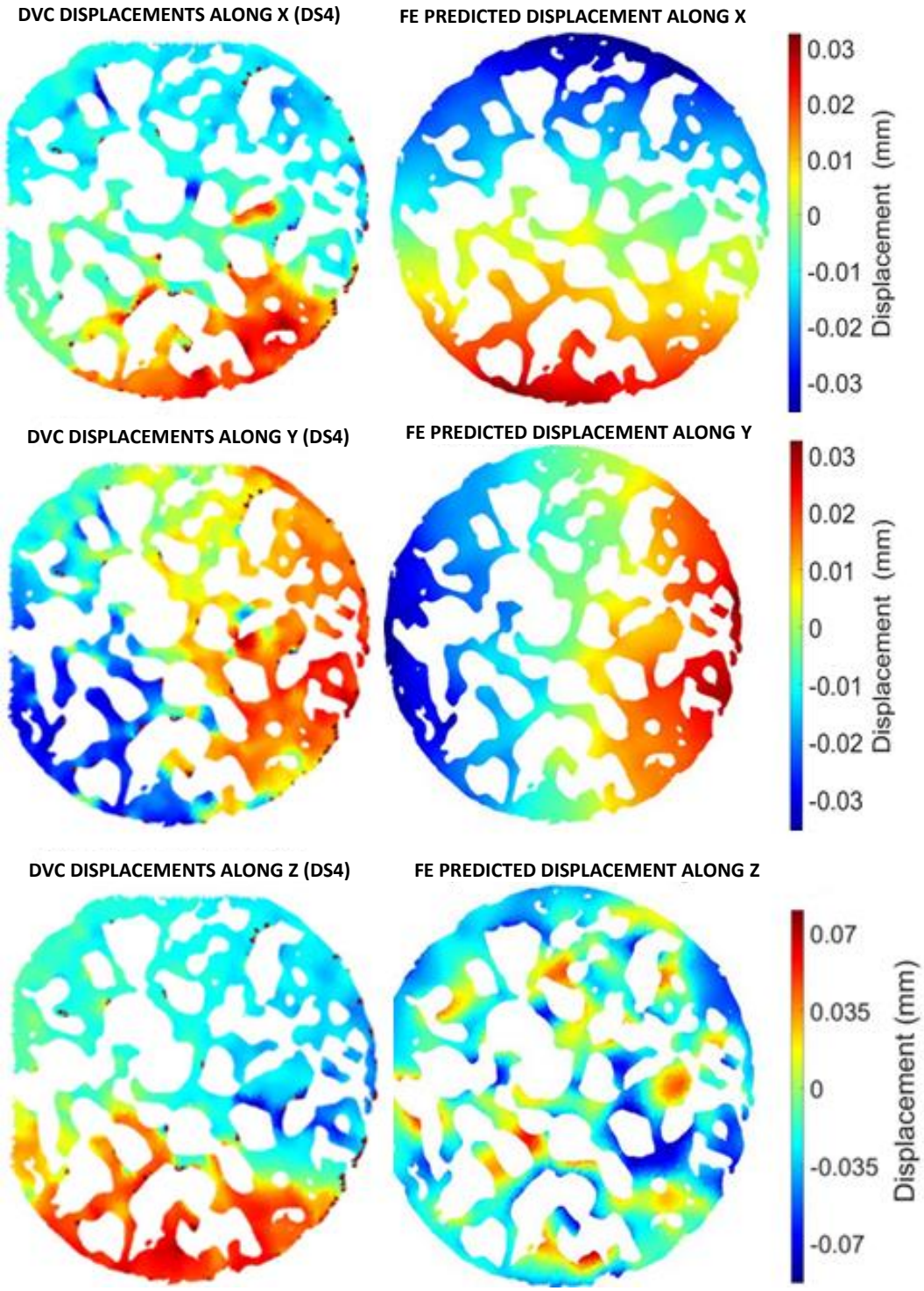

Figure 5.16. Comparisons of displacements from downscaled by 4 DVC data and FE predicted displacements at z=1.08 mm. Row 1, 2, and 3 consists of displacement components x, y and z respectively, while column 1 shows DVC data and column 2 displacements predicted by µFE model. Load step 5 is shown.

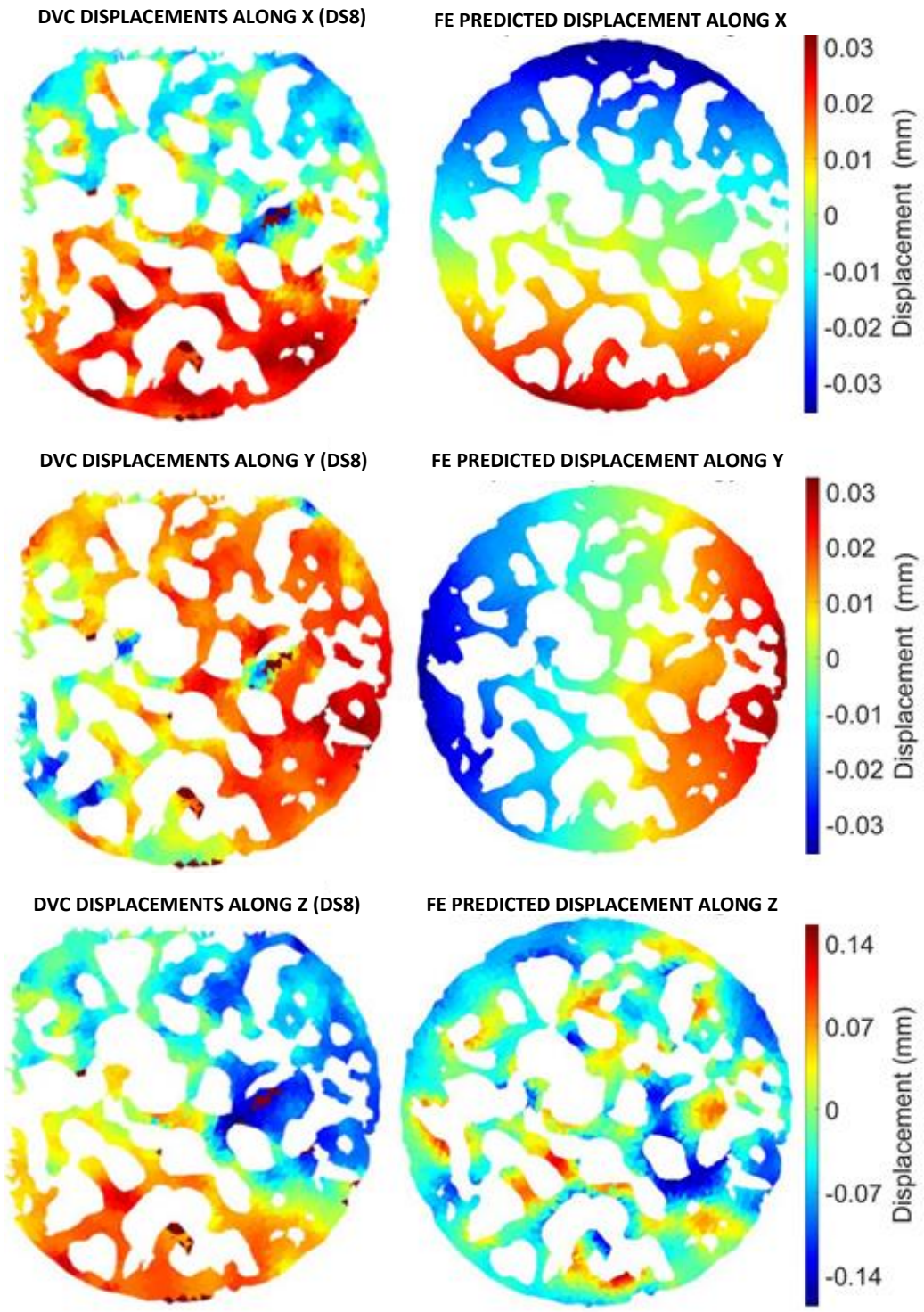

Figure 5.17. Comparisons of displacements from downscaled by 8 DVC data and FE predicted displacements at z=1.08 mm. Row 1, 2, and 3 consists of displacement components x, y and z respectively, while column 1 shows DVC data and column 2 displacements predicted by µFE model. Load step 5 is shown.

The strains and displacements predicted by µFE model, and the corresponding experimental strains and displacements can also be visualized as correlation plots, as shown in Figure 5.18, 5.19 and 5.20, where the correlation of high-resolution and downscaled data is investigated. All coefficients calculated from the correlations between predicted and measured displacements are reported in Table 5.3. Considering high-resolution data, similar correlations were found in simple and confined compression. In both cases, the coefficient of determination was greater than 0.65, but the slope was low (~ 0.20). This suggests that we are far from a 1:1 relationship even though the intercept was close to zero. The RMSE% was around 0.07%.

Considering downscaled by 4 and 8 data, µFE model predictions of volumetric strains were better correlated and more in agreement with the experimental measurements in the case of downscaled by 8 measurements with a coefficient of determination of 0.53 and a slope of 0.46.

	DATA	R^2	slope	intercept (mm)
HIGH-RESOLUTION	vol.strain -simple	0.63	0.25	-0.53
	vol.strain-confined	0.65	0.18	-0.3
	u_x	0.57	0.22	-0.03
	u_y	0.43	-0.21	-0.003
	u_z	0.54	0.32	-0.01
DS4	vol.strain-simple	0.51	0.44	-0.12
	u_x	0.35	-0.23	0.004
	u_y	0.58	0.32	-0.04
	u_z	0.56	0.34	-0.02
DS8	vol.strain-simple	0.53	0.46	-0.11
	u_x	0.71	-0.18	0.016
	u_y	0.68	0.47	-0.063
	u_z	0.54	0.24	0.03

Table 5.3. Predictions of µFE model from DVC results at $p<0.05$. "u" values are displacements along x, y and z directions.

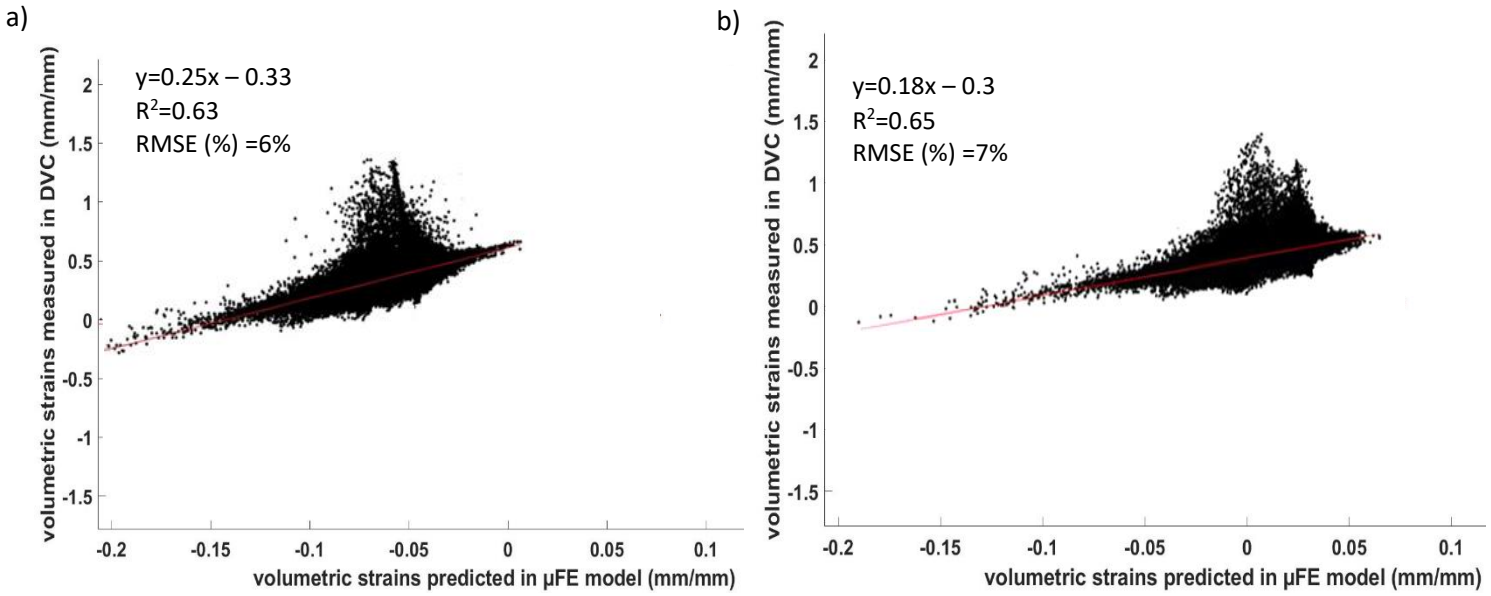

Figure 5.18. Volumetric strains predicted by µFE model plotted against DVC measurements for high-resolution data in simple (a) and confined (b). Load step 5 is shown.

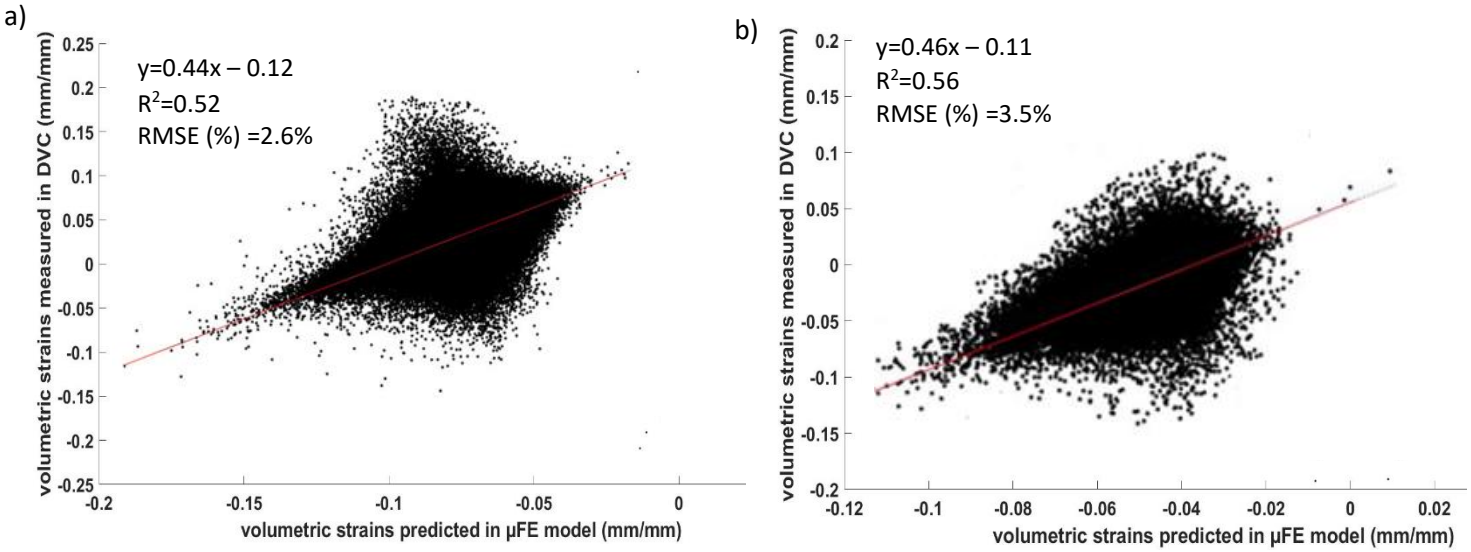

Figure 5.19. Volumetric strains predicted by µFE model plotted against DVC measurements for downscaled by 4 (a) and downscaled by 8 (b) data. Load step 5 is shown.

Figure 5.20 shows correlation plots for displacement components and for the three levels of resolution. Similar trends were found for high-resolution measurements along x-direction and z-direction with a slope between 0.22 and 0.32 and a coefficient of determination around 0.60. A negative correlation was found for y-direction with a coefficient of determination of 0.43.

For downscaled by 4 data, predictions of local displacements along x and y directions were better than z-direction with a coefficient of determination around 0.60. The slope was around 0.30.

For downscaled by 8 data, predictions of local displacements along x and y directions were better than z-direction with a coefficient around 0.70.

However, the best correlation was found for predictions of y-component of displacement for downscaled by 8 data with a slope equal to 0.47 and a coefficient of determination of 0.68.

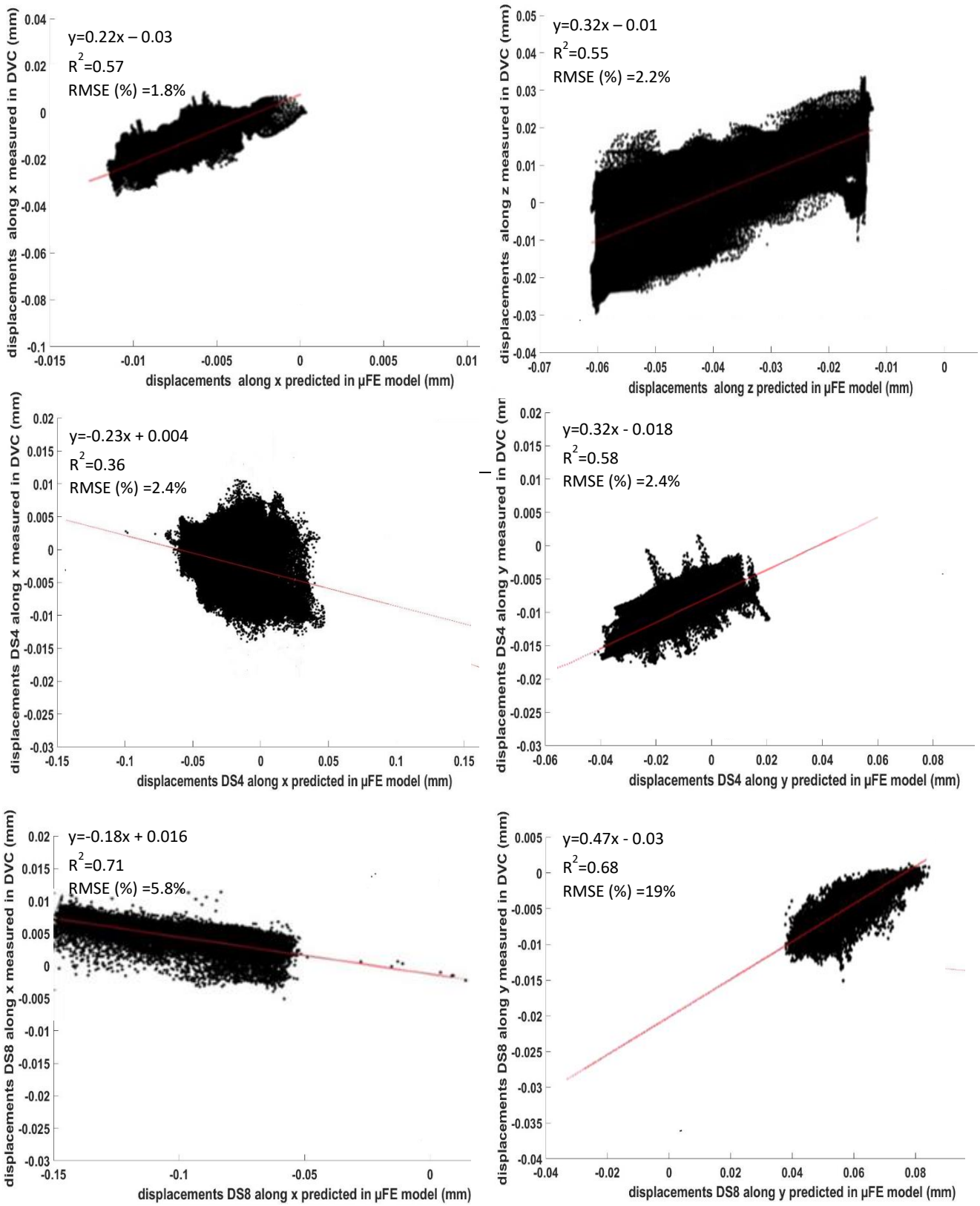

Figure 5.20. Displacements predicted by µFE model plotted against DVC measurements for high-resolution simple compression (Row 1), downscaled by 4 (Row 2) and downscaled by 8 (Row 3) data. In row 1 displacements along x and z – directions are shown, while in row 2 and 3 displacements along x and y – directions are shown. Load step 5 is shown.

Chapter 6

Discussion

The aim of this master's thesis was to improve predictions of bone damage and fracture on the microscale. Towards this aim, a subject-specific FE model of a sub-volume isolated from a cylindrical trabecular bone plug of human femoral head was developed and a procedure to validate the model by using experimental data from Digital Volume Correlation was implemented. The thesis work was divided into two main blocks, namely:

1- Development of a subject-specific micro-FE model from μCT images.
2- Development of a validation procedure based on interpolation of experimental data from Digital Volume Correlation.

The main outcome of this study is the development of a computational method to enable validation of a μFE model against DVC measurements obtained from high-resolution tomographic images.

Moreover, to our knowledge, the current study is one of the first attempts concerning FE-model validation at this scale (i.e., micro-scale) and at such high-resolution level, since a few other studies [10] have carried it out before.

6.1 Development of a subject-specific micro-FE model from µCT images

6.1.1 Convergence study

The purpose of the convergence study was to find the appropriate mesh refinement to be use in the following of the thesis project.

The maximum volumetric strain and the maximum major principal strain were investigated as parameters for the convergence. This was motivated by the fact that Turunen et al. in their work [1] investigated the three-dimensional volumetric strain distribution and its evolution during loading at the sub trabecular level to capture detailed crack-paths.

Turunen et al. reported that *"already from the beginning of the loading, strains start to accumulate more in the regions where the trabeculae will finally break"*. Therefore the convergence study was performed on the crack regions of the sub-volume model from high-resolution data since we know that the analysis of the high-resolution data provides local strain distributions and magnitudes in higher detail than downscaled data [1]. Crack regions were defined by the procedure described in section 4.4.1.

Even though looking at the maximum volumetric strain or major principal strain as parameter for convergence is challenging because it tends to increase by decreasing element size in the FE model instead of stabilizing, the results from the convergence study, figure 5.1, showed a clear convergence for both parameters.

Previous studies published in literature used threshold for convergence between 2-5% [32], [33]. Therefore, in this work it was assumed that when the difference between the maximum volumetric strain or major principal strain obtained from meshes of consecutive refinements is less than 2%, the convergence criterion was fulfilled. In this way a mesh with 2'500'000 elements whose maximum volume was around 0.0162 mm^3 was considered appropriate for the study.

Histogram of mesh quality in fig 5.2a showed a good mesh quality because most of the elements have an aspect ratio close to 1 which means that elements are not stretched or distorted but keep their shape. Moreover, histogram of elements volume distribution in fig5.2b showed one peak centred in 1 μm^3 as result of a uniform mesh whose elements have quite similar volumes. These two results ensured a very refined mesh.

6.2 Development of a validation procedure based on interpolation of experimental data from Digital Volume Correlation

The development of the validation procedure had the aim to find a 1:1 relationship between measured and predicted values since a difference in the length scale of the basic unit for the analysis in DVC and in the finite element size was found. This way point-by-point validation was carried out and it was possible answering to the question: "Are high-deformation peaks revealed by μFE model localised in the same position of the DVC high strains?".

Noise effects had an important impact on the validation procedure and on the volumetric strain and displacement analysis. Especially, this was more visible on the volumetric strain map. This suggests that noise effect is strictly linked to the analysed parameter in the validation procedure. If the parameter is the volumetric strain, the spatial derivative showed in the eq. (1) section 4.2.6 causes an increasing of noise effects and this leads to further difficulties in finding a correspondence between measure and prediction.

Moreover, noise effects did not allow a clear distribution of volumetric strain: for instance, we can see that there are regions in tension immediately close to regions in compression (yellow and red regions close to blue regions – fig. 6.1a) and it can also be noted that these regions are not placed in the same position during all the load steps, but they are located differently from one load step to the following (fig. 6.1b).

Additionally, looking at the evolution of DVC images from load step 1 to 7, we can notice that noise intensity was the same from load step 1 to 4, and then increased at load step 5 and at the following ones. This is due to the fact that the sample was close to failure (load step 4-5) and failed (load 5-6-7) and the resulting μCT images were blurred because of the movement of the bone plug in the experiment setting.

Therefore, this suggests that, at this high-resolution (i.e., voxel size 3.6 x3.6x3.6 μm^3), the noise influences the analysis and the interpretation of the images substantially. Indeed all available DVC methods can provide reasonably accurate quantifications of strains only over much coarser resolution (i.e., 40-50 voxels) [29]. Moreover, at this resolution level, it seems like DVC allows only to distinguish crack-regions from non-crack regions. The result is that the obtained map shows only where local strains are very high (fig. 6.1 f-g). Even though the model allowed to predict where

fracture will finally occur, this feature is clearly crucial in limiting what is possible to validate and where it is possible to validate the model.

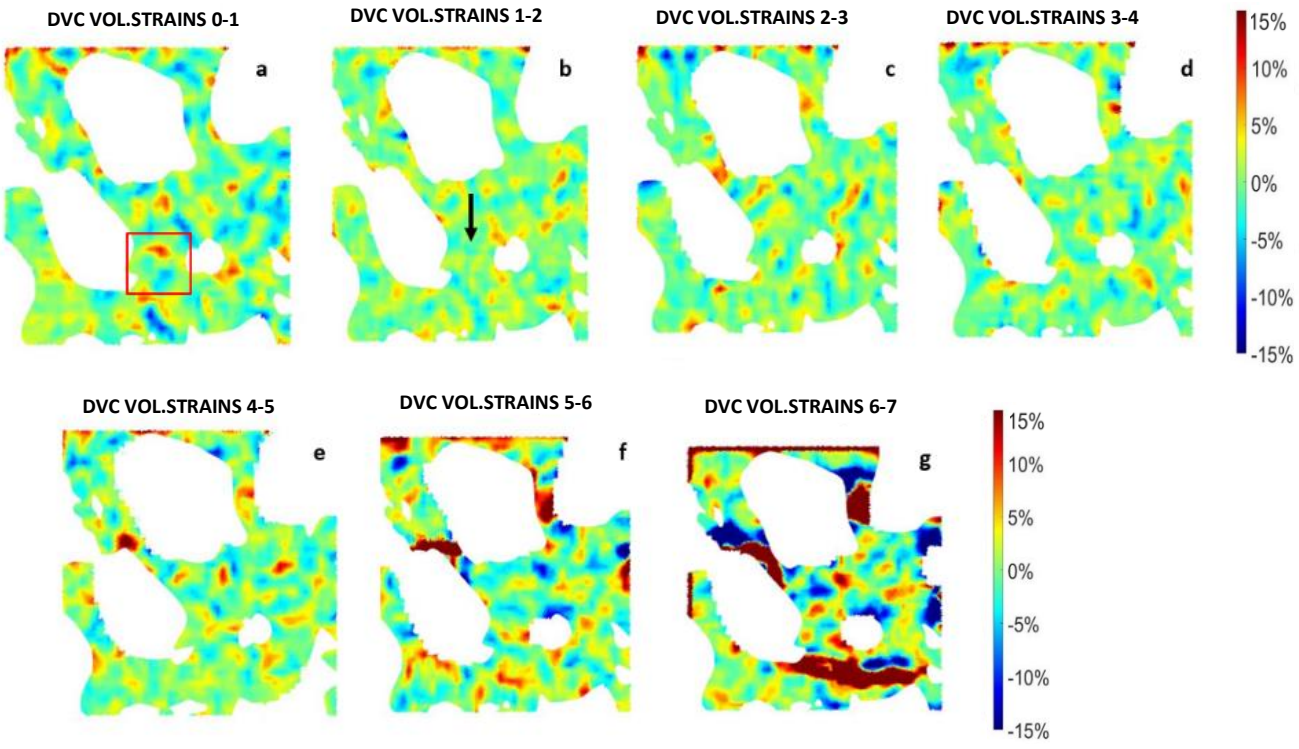

Figure 6.1. Evolution of loading steps during the experiment. Volumetric strain maps from DVC interpolated data are shown(a-g). Red square in (a) shows a compression region close to a tension region. Black arrow in (b) shows the previous regions moved.

It should be noted that so far, we have analysed images from high-resolution DVC data which are typically more susceptible to noise effects than the other levels of resolution. Indeed, DVC resolution is strictly related to sub-volume size: if the sub-volume is too small, it results in a good spatial resolution, but it is typically susceptible to noise effects and at the same time an excessively large sub-volume may result in an inadequate spatial resolution. This motivated the idea to extend the analysis to downscaled data. Indeed, by visual inspection, results from volumetric strain comparisons showed that noise effects decreased especially in load step 5 (fig. 5.11, 5.12, 5.13) providing a better correlation, even though spatial resolution decreased.

Analysis of displacement components provided better results than absolute displacement and volumetric strains as well. This corroborates the thesis that noise effects have a different impact according to the analysed parameter. An interesting thing is that a good agreement was found for only two displacement components both in high resolution and downscaled data. A similar trend with only two components well matched and with equal method to define boundary conditions was observed in a similar study [24]. The authors of the study suggested that this aspect was due to the applied boundary conditions which were simplified and not interpolated from the DVC fields.

These considerations are partially supported by statistical analysis (fig. 5.18, 5.19, 5.20). The best coefficient of determination between experimental and computational results of the displacement was found for the y direction for downscaled by 4 (R^2=0.58) and for the x-direction for downscaled by 8 data (R^2=0.71), even though the slope was around 0.30. Therefore, in the z-direction an inferior accuracy was achieved with respect to x and y directions. While for the volumetric strains similar trends were found for simple and confined compression with a coefficient of determination around 0.65. For downscaled by 8 a better correlation (R^2=0.53) was found compared to downscaled by 4. In general, the μFE analysed models predicted smaller deformations and displacements than measured using DVC (the slopes are smaller than one indicating that FE predictions were smaller than DVC measurements).

These results are consistent with those of Zauel et al. [34] and Zhu et al. [35]. According to the first study, finite element modelling of the strain and displacement in human cancellous bone can be accurate in one direction but this does not ensure accuracy for all displacements and strains. The authors attributed the difference between DVC and FE methods to the scanning technology. In Zhu et al., it is shown that not only in human bones, but also in bovine trabecular bones, strain fields differ greatly, even though displacement fields predicted by μFE compared reasonably well with that obtained from the DVC. This suggests that DVC method has a limitation in mapping strains. In this last case, the authors found a reason in the difference in the length scale of the basic unit for the analyses in both DVC and μFE methods (i.e., a sub-volume size of DVC compared to the element size in the μFE model).

6.3 Limitations

The main limitations in this thesis are divided in limitations regarding the micro-FE model and limitations regarding the analysis of DVC data and the validation procedure.

6.3.1 µFE model

A material parameters study was not performed: material properties were assumed linear, elastic, and isotropic with a uniform Young's modulus of 13 GPa. Literature reveals that trabecular bone is an orthotropic material with various behaviours in three anatomical directions [33] and it is also an heterogeneous material whose heterogeneity can have an effect on the micromechanical behaviour [10]. In this study, a simplified model was realised with the assumption of elastic and homogenous behaviour.

Moreover, only two different boundary conditions were applied: uniform compression loading and confined compression loading. The choice of applying a confined compression was motivated by the need to reproduce a condition as physiological as possible. In a confined compression, as explained in session 4.2.4, the back, front, right and left sides of the sub-volume were constrained in order to simulate the condition where sub-trabecular volume is affected by the pressure of the surrounding bone (fig. 6.2). This oversimplification plays an important effect in limiting the accuracy and the fidelity of the model in simulating bone failure and in capturing a correct strain distribution, as stated in some studies [36]. Indeed, the authors of the study [36] suggest to use BCs directly derived from experimental measurements (for example from DVC-measured values) instead of applying idealized BCs that are not exactly reproducing the real case.

In agreement with this finding is an other interesting study concerning the issue of BCs [24]. Kunnoth et al. in their work showed that using DVC interpolated displacement boundary conditions (IPBC) provided a good comparison of displacement components with a coefficient of determination between 0.84 and 0.99 for all displacement components. While, using simplified experimental-based boundary condition, as in the case of this project, could predict only lateral displacement and provided a poor correlation for the other components.

Indeed, it has been demonstrated that in order to obtain proper correlations between values measured with DVC and predicted with micro-FE model, the

boundary conditions in the models need to be interpolated from the DVC fields. In this way it is possible to correct for potential experimental artifacts in the mechanical testing [4].

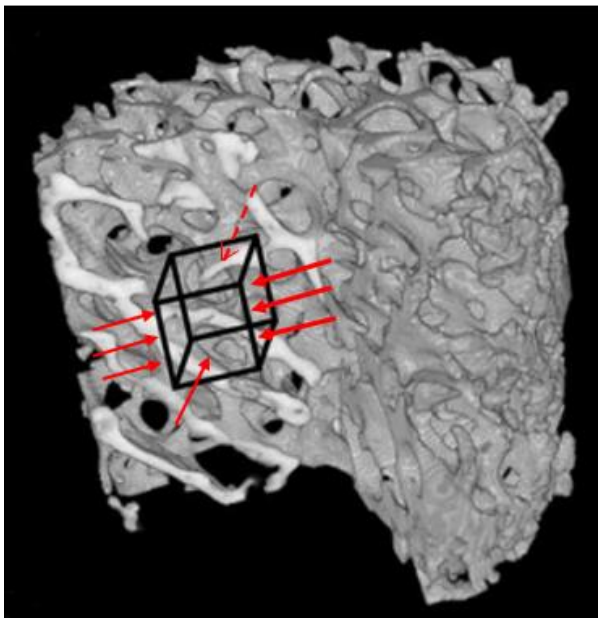

Figure 6.2. Location of the sub-region with respect to the whole sample. Red arrows indicate the pressure of the surrounding bone on the analysed volume. Image adapted from Turunen et al.,2020 [2].

Another aspect related to FE model should be considered: compared to a previous study [24], this study does not account for the frictional effects between the compression plates and the sample. These effects can be incorporated in BCs and can affect displacement patterns. Indeed, the mentioned study stated that the case where frictional effects were included in the BCs showed a good R^2 value for the lateral displacement component [24].

In summary, the implementation of a material parameters study and the incorporation of more sophisticated BCs could represent a partial solution to the mentioned issues.

Nevertheless, the goal of this study was not to optimize the modelling approach but to develop a procedure of validation μFE vs DVC.

6.3.2 DVC and validation procedure

Some imprecisions in the matching of DVC-measured and FE-computed data arose from the validation procedure.

As we know, DVC is a technique that, as is typical for image correlation methods, has several problems which can invalidate the quality of the acquired data. For instance, we can mention some of the ones related to the limitations of this work:

1. Several parameters within the DVC algorithm, as well as the microstructure of the investigated specimen, can influence the performance of this technique. Changes to the DVC parameters, such as DVC objective function, shape function, and image subset size, and changes in image contrast and voxel size, can affect the accuracy and precision of displacement and strain measurements, and the computation time required for each displacement calculation.
2. The amount of material within each sub-volume and therefore the sub-volume size affects DVC resolution [37], [38]. As is typical for image correlation methods, the magnitudes of the errors decrease with increasing subregion size. But we know also that if the sub-volume is too small, it is typically susceptible to noise effects and at the same time an excessively large sub-volume may result in an inadequate spatial resolution [39]. Indeed, in general, increasing the subregion size means decreasing the spatial resolution of strains and displacements, so there is generally a dependence between strain or displacement magnitude and image voxel size.
3. Several artefacts during X-ray tomographic imaging (e.g., the ring artifacts, beam hardening or the potential micro-movements of the loading plate) can seriously degrade the contrast, resolution, fidelity and stability of acquired volume images [40];

Even though a real solution to all these issues was not found yet, the development of new algorithms for voxel level DVC analysis and advanced scanning techniques could be one possibility.

6.4 Future perspectives

The ideal future step for this project should address the limitations mentioned in the section above with the aim to develop a more realistic μFE model. It would be interesting to explore if the predictive accuracy of the μFE model is further improved by a more accurate study of the material parameters. For instance, it could be beneficial:

1) *Addition of local heterogeneity*: instead of using a uniform elastic modulus value, it is evaluated based upon the map of the tissue mineral density of the bone.
2) *Addition of non-linearities* in order to simulate the local yielding of the trabecular bone structure.
3) *Introduction of more sophisticated and refined boundary conditions* which can be estimated by the values measured during the experiment ("experimentally matched loading") to accurately reproduce the loading condition. For instance, there are studies which use interpolated values from DVC results as boundary conditions [24],[4].

Chapter 7

Summary and Conclusions

In this thesis, a subject-specific μFE model based on high-resolution μCT images was created and a method for validation was implemented. Strain magnitudes, evolution and distribution at sub trabecular level were investigated by Digital Volume Correlation [1]. These measurements were used as experimental data to compare to μFE model predictions.

In summary the present study has provided a working method for quantitative validation of μFE models against DVC experimental data. By the means of this method, we have demonstrated that the presented μFE models were able to predict the locations of high volumetric strains where fracture and damage will occur in the bone plug, according to Turunen et al. findings. Moreover, displacement validation results revealed a good prediction in two directions, but this does not ensure accuracy for all displacements.

The results of this study show that:

- Simple and confined compression as boundary conditions in the μFE model do not provide clear differences in terms of strain and displacement predictions.
- The implemented working method to validate μFE model exhibits good results. Volumetric strain and displacement maps show a quite similar pattern compared to the original one from experimental measurements. Moreover, this is a flexible method which can be used with unstructured and structured meshes and it is able to balance spatial resolution gap between DVC data and FE element size.
- Noise represents an important limitation in DVC analysis especially for volumetric strains and at high-resolution level. It does not allow a clear interpretation of volumetric strain maps since random spots of high strains were immediately close to the low strain ones. This suggests that at this level of resolution, digital volume correlation can distinguish crack-regions from non-crack regions only.

- Image voxel size influences strain and displacement magnitudes: downscaled by 4 and 8 factor measurements show clearer distributions of volumetric strain and displacement than high-resolution data. Indeed, uniform maps of strain and displacement can be observed without random spots. This corroborates the fact that larger sub-volume size entails less susceptibility to noise effects, even though spatial resolution clearly decreases.
- Visual and statistical comparisons between μFE and DVC show that volumetric strain fields differ significantly between the two methods and that the μFE model can detect only high volumetric strain regions where cracks are about to occur. As regards displacement field, μFE model can be accurate in two directions. This suggests a challenge for further development in methods for both the DVC and the μFE model.

Appendix

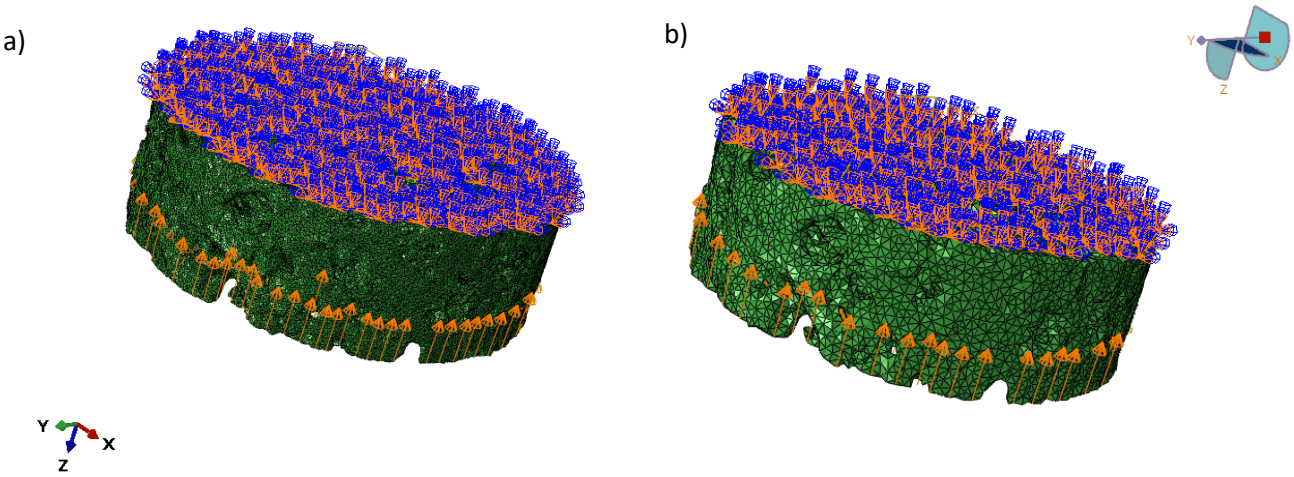

Figure A.1. Downscaled by 4 (a) and by 8 (b) mesh models with applied BCs

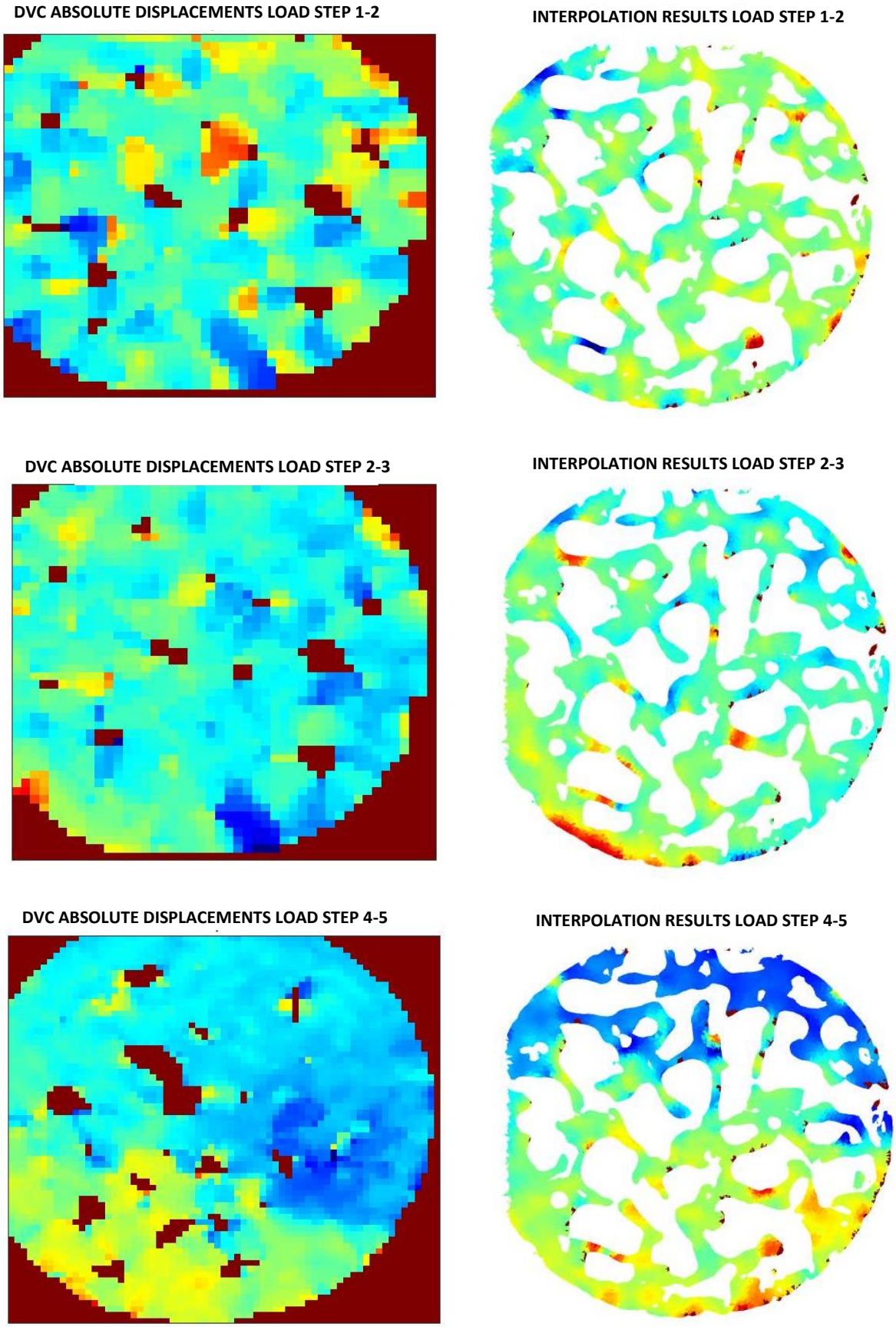

Figure A.2. Absolute displacement maps from Digital Volume Correlation of downscaled by 4 data (left) compared to the interpolated values to FE nodes (right) for load step 2, 3 and 5 respectively.

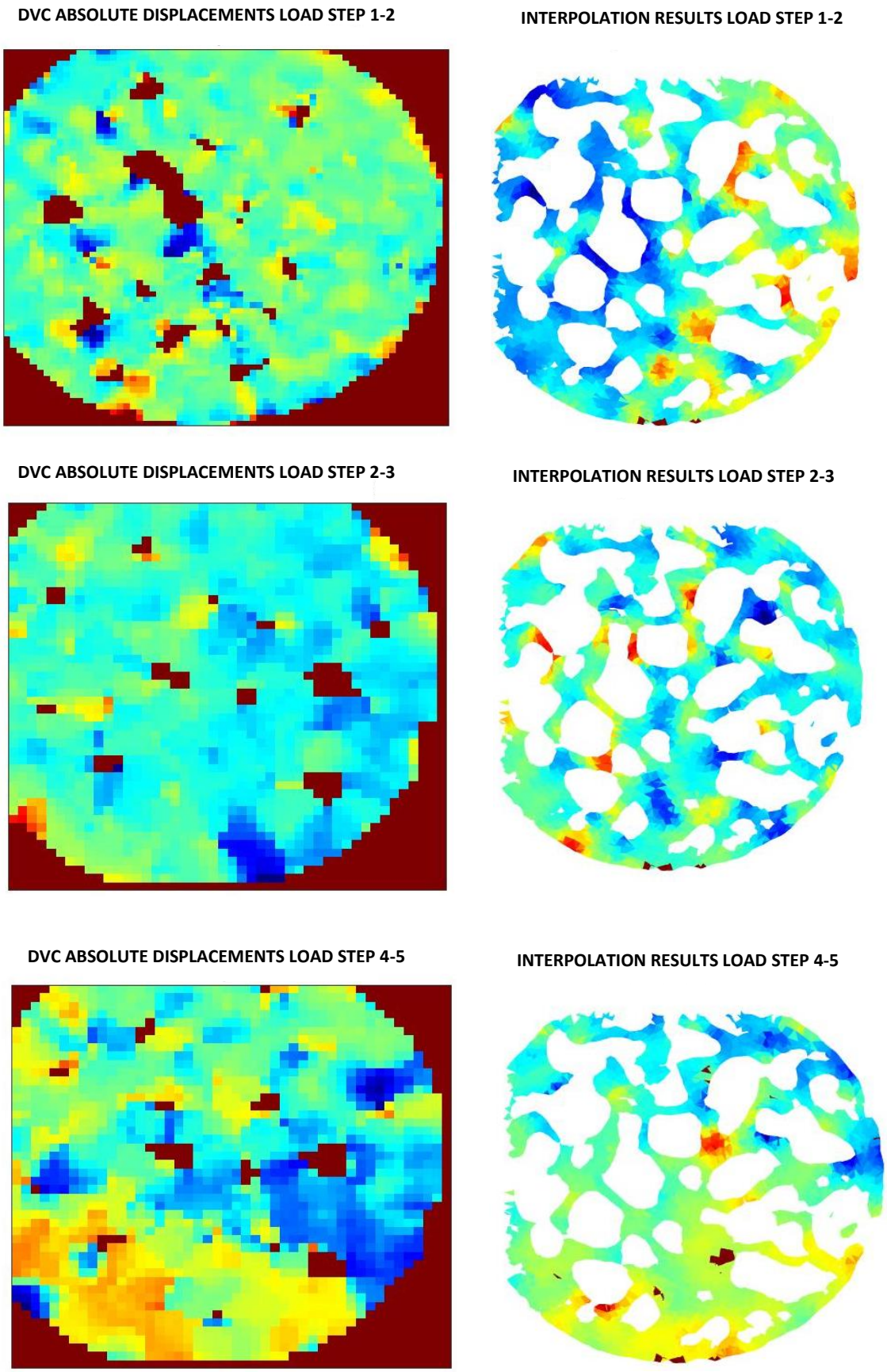

Figure A.3. Absolute displacement maps from Digital Volume Correlation of downscaled by 8 data (left) compared to the interpolated values to FE nodes (right) for load step 2, 3 and 5 respectively.

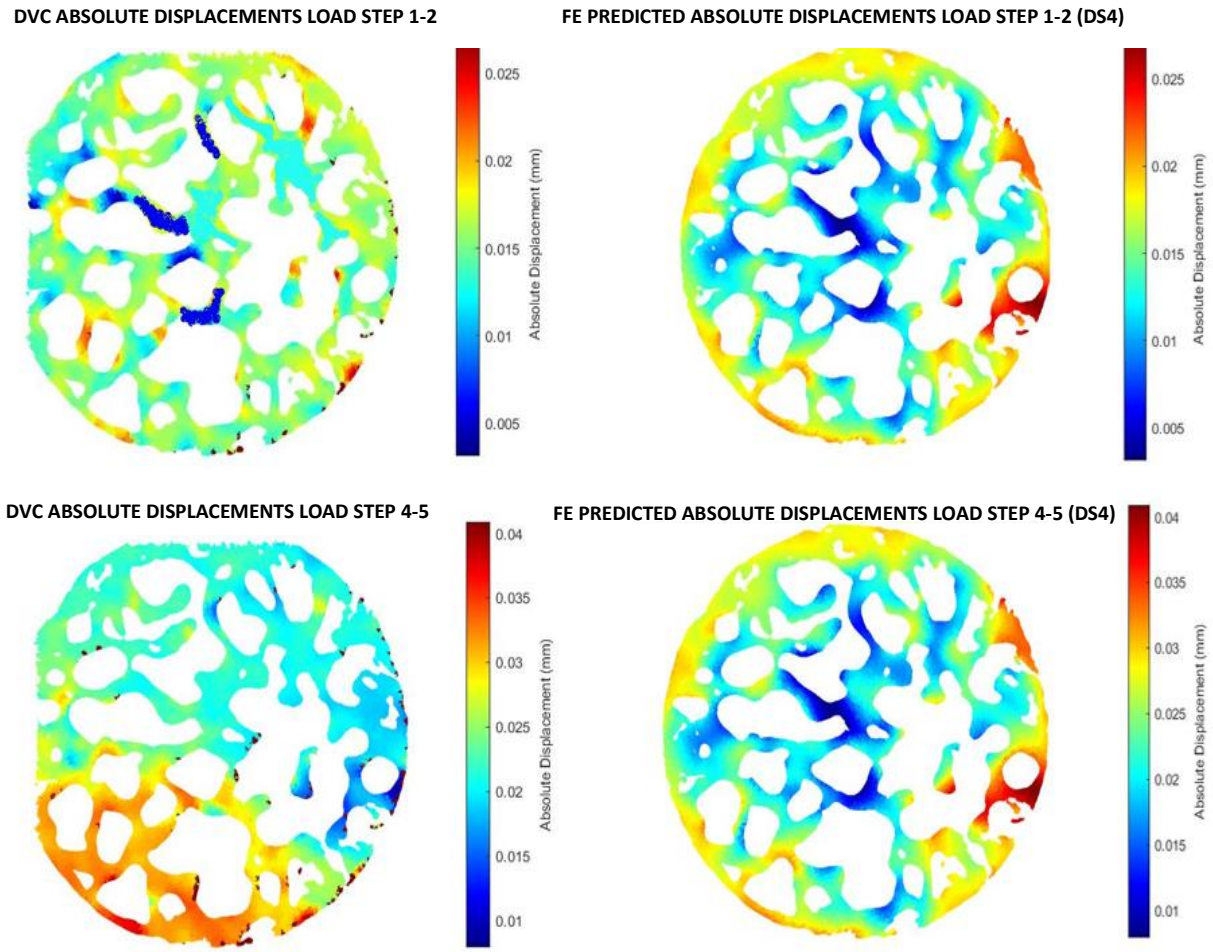

Figure A.4. DVC absolute displacement interpolated values to FE nodes (left) compared to FE predicted displacements for downscaled by 4 data for load step 2 (top row) and load step 5 (bottom row).

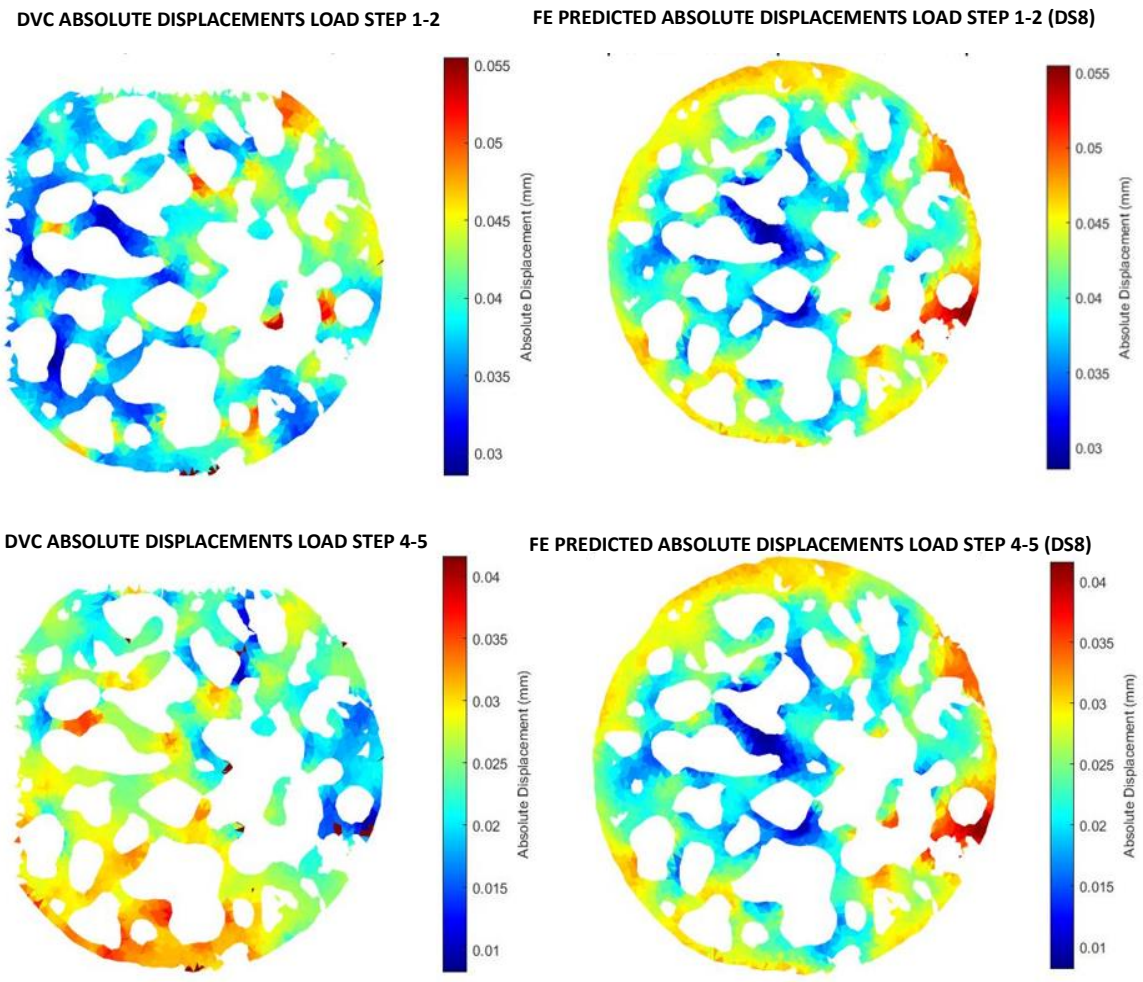

Figure A.5. DVC absolute displacement interpolated values to FE nodes (left) compared to FE predicted displacements for downscaled by 8 data for load step 2 (top row) and load step 5 (bottom row).

Bibliography

[1] M. J. Turunen *et al.*, 'Sub-trabecular strain evolution in human trabecular bone', *Sci Rep*, vol. 10, no. 1, p. 13788, Dec. 2020, doi: 10.1038/s41598-020-69850-x.

[2] Weltgesundheitsorganisation, Ed., *Prevention and management of osteoporosis: report of a WHO scientific group ; [WHO Scientific Group Meeting on Prevention and Management of Osteoporosis, Geneva, 7 - 10 April]*. Geneva: World Health Organization, 2003.

[3] T. Sozen, L. Ozisik, and N. Calik Basaran, 'An overview and management of osteoporosis', *Eur J Rheumatol*, vol. 4, no. 1, pp. 46–56, Mar. 2017, doi: 10.5152/eurjrheum.2016.048.

[4] M. C. Costa, G. Tozzi, L. Cristofolini, V. Danesi, M. Viceconti, and E. Dall'Ara, 'Micro Finite Element models of the vertebral body: Validation of local displacement predictions', *PLoS ONE*, vol. 12, no. 7, p. e0180151, Jul. 2017, doi: 10.1371/journal.pone.0180151.

[5] Y. Lee, N. Ogihara, and T. Lee, 'Assessment of finite element models for prediction of osteoporotic fracture', *Journal of the Mechanical Behavior of Biomedical Materials*, vol. 97, pp. 312–320, Sep. 2019, doi: 10.1016/j.jmbbm.2019.05.018.

[6] R. Oftadeh, M. Perez-Viloria, J. C. Villa-Camacho, A. Vaziri, and A. Nazarian, 'Biomechanics and Mechanobiology of Trabecular Bone: A Review', *Journal of Biomechanical Engineering*, vol. 137, no. 1, p. 010802, Jan. 2015, doi: 10.1115/1.4029176.

[7] J. Wolff, *The Law of Bone Remodelling*. Springer Science & Business Media, 2012.

[8] T. M. Keaveny, E. F. Morgan, G. L. Niebur, and O. C. Yeh, 'Biomechanics of Trabecular Bone', *Annu. Rev. Biomed. Eng.*, vol. 3, no. 1, pp. 307–333, Aug. 2001, doi: 10.1146/annurev.bioeng.3.1.307.

[9] F. Ozan, M. Pekedis, Ş. Koyuncu, T. Altay, H. Yıldız, and C. Kayalı, 'Micro-computed tomography and mechanical evaluation of trabecular bone structure in osteopenic and osteoporotic fractures', *J Orthop Surg (Hong Kong)*, vol. 25, no. 1, p. 230949901769271, Jan. 2017, doi: 10.1177/2309499017692718.

[10] J. Fu *et al.*, 'Effects of tissue heterogeneity on trabecular micromechanics examined by microCT-based finite element analysis and digital volume correlation', *Medicine in Novel Technology and Devices*, vol. 11, p. 100088, Sep. 2021, doi: 10.1016/j.medntd.2021.100088.

[11] E. F. Morgan, G. U. Unnikrisnan, and A. I. Hussein, ‘Bone Mechanical Properties in Healthy and Diseased States’, *Annu. Rev. Biomed. Eng.*, vol. 20, no. 1, pp. 119–143, Jun. 2018, doi: 10.1146/annurev-bioeng-062117-121139.
[12] ‘OSTEOPOROSIS - Risk assessment | International Osteoporosis Foundation’. https://www.osteoporosis.foundation/educational-hub/topic/osteoporosis-risk-assessment (accessed Apr. 06, 2022).
[13] L. J. Melton III, E. J. Atkinson, M. K. O’Connor, W. M. O’Fallon, and B. L. Riggs, ‘Bone Density and Fracture Risk in Men’, *Journal of Bone and Mineral Research*, vol. 13, no. 12, pp. 1915–1923, 1998, doi: 10.1359/jbmr.1998.13.12.1915.
[14] J. A. Kanis *et al.*, ‘Long-Term Risk of Osteoporotic Fracture in MalmoÈ’, p. 6.
[15] L. J. Melton, S. J. Achenbach, E. J. Atkinson, T. M. Therneau, and S. Amin, ‘Long-term mortality following fractures at different skeletal sites: a population-based cohort study’, *Osteoporos Int*, vol. 24, no. 5, pp. 1689–1696, May 2013, doi: 10.1007/s00198-012-2225-1.
[16] M. Viceconti, P. Hunter, and R. Hose, ‘Big Data, Big Knowledge: Big Data for Personalized Healthcare’, *IEEE Journal of Biomedical and Health Informatics*, vol. 19, no. 4, pp. 1209–1215, Jul. 2015, doi: 10.1109/JBHI.2015.2406883.
[17] E. S. Orwoll *et al.*, ‘Finite Element Analysis of the Proximal Femur and Hip Fracture Risk in Older Men’, *Journal of Bone and Mineral Research*, vol. 24, no. 3, pp. 475–483, 2009, doi: 10.1359/jbmr.081201.
[18] D. Ruffoni and G. H. van Lenthe, ‘3.10 Finite Element Analysis in Bone Research: A Computational Method Relating Structure to Mechanical Function ☆’, in *Comprehensive Biomaterials II*, Elsevier, 2017, pp. 169–196. doi: 10.1016/B978-0-12-803581-8.09798-8.
[19] J. Kok, ‘A biomechanical analysis of fracture strength prediction, prevention, and repair’, p. 95.
[20] G. H. van Lenthe and R. Müller, ‘Prediction of failure load using micro-finite element analysis models: Toward in vivo strength assessment’, *Drug Discovery Today: Technologies*, vol. 3, no. 2, pp. 221–229, Jun. 2006, doi: 10.1016/j.ddtec.2006.06.001.
[21] M. Salomé *et al.*, ‘A synchrotron radiation microtomography system for the analysis of trabecular bone samples’, *Medical Physics*, vol. 26, no. 10, pp. 2194–2204, 1999, doi: 10.1118/1.598736.
[22] H. D. Barth, M. E. Launey, A. A. MacDowell, J. W. Ager, and R. O. Ritchie, ‘On the effect of X-ray irradiation on the deformation and fracture behavior of human cortical bone’, *Bone*, vol. 46, no. 6, pp. 1475–1485, Jun. 2010, doi: 10.1016/j.bone.2010.02.025.

[23] K. Madi *et al.*, 'Computation of full-field displacements in a scaffold implant using digital volume correlation and finite element analysis', *Medical Engineering & Physics*, vol. 35, no. 9, pp. 1298–1312, Sep. 2013, doi: 10.1016/j.medengphy.2013.02.001.
[24] S. Kunnoth, P. Mahajan, S. Ahmad, and N. Bhatnagar, 'Compressive strain measurements in porous materials using micro-FE and digital volume correlation', *The Journal of Strain Analysis for Engineering Design*, p. 030932472110387, Aug. 2021, doi: 10.1177/03093247211038791.
[25] X. Zhang, G. Yang, J. Ye, R. Li, and P. Yang, 'Digital volume correlation using a spherical shell template and cubic element for large rotation measurement', *Appl. Opt.*, vol. 59, no. 35, p. 11123, Dec. 2020, doi: 10.1364/AO.408319.
[26] B. Wang and B. Pan, 'Incremental digital volume correlation method with nearest subvolume offset: An accurate and simple approach for large deformation measurement', *Advances in Engineering Software*, vol. 116, pp. 80–88, Feb. 2018, doi: 10.1016/j.advengsoft.2017.12.004.
[27] 'CGAL User and Reference Manual: Table of Contents'. https://doc.cgal.org/Manual/3.5/doc_html/cgal_manual/contents.html (accessed Apr. 04, 2022).
[28] A. Liu and B. Joe, 'Relationship between tetrahedron shape measures', p. 20.
[29] Y. Chen *et al.*, 'Micro-CT based finite element models of cancellous bone predict accurately displacement once the boundary condition is well replicated: A validation study', *Journal of the Mechanical Behavior of Biomedical Materials*, vol. 65, pp. 644–651, Jan. 2017, doi: 10.1016/j.jmbbm.2016.09.014.
[30] C. Corrado, S. Williams, R. Karim, G. Plank, M. O'Neill, and S. Niederer, 'A work flow to build and validate patient specific left atrium electrophysiology models from catheter measurements', *Med Image Anal*, vol. 47, pp. 153–163, Jul. 2018, doi: 10.1016/j.media.2018.04.005.
[31] S. Liu *et al.*, 'Application of multidimensional interpolation on nonhomogeneous cancellous bone', *Medicine*, vol. 97, no. 36, p. e12224, Sep. 2018, doi: 10.1097/MD.0000000000012224.
[32] M. Salem, L. Westover, S. Adeeb, and K. Duke, 'Prediction of failure in cancellous bone using extended finite element method', *Proc Inst Mech Eng H*, vol. 234, no. 9, pp. 988–999, Sep. 2020, doi: 10.1177/0954411920936057.
[33] M. Salem, L. Westover, S. Adeeb, and K. Duke, 'An Equivalent Constitutive Model of Cancellous Bone With Fracture Prediction', *Journal of Biomechanical Engineering*, vol. 142, no. 12, p. 121004, Dec. 2020, doi: 10.1115/1.4047080.

[34] R. Zauel, Y. N. Yeni, B. K. Bay, X. N. Dong, and D. P. Fyhrie, 'Comparison of the Linear Finite Element Prediction of Deformation and Strain of Human Cancellous Bone to 3D Digital Volume Correlation Measurements', *Journal of Biomechanical Engineering*, vol. 128, no. 1, pp. 1–6, Feb. 2006, doi: 10.1115/1.2146001.
[35] M.-L. Zhu, Q.-H. Zhang, C. Lupton, and J. Tong, 'Spatial resolution and measurement uncertainty of strains in bone and bone–cement interface using digital volume correlation', *Journal of the Mechanical Behavior of Biomedical Materials*, vol. 57, pp. 269–279, Apr. 2016, doi: 10.1016/j.jmbbm.2015.12.017.
[36] A. I. Hussein, D. T. Louzeiro, G. U. Unnikrishnan, and E. F. Morgan, 'Differences in Trabecular Microarchitecture and Simplified Boundary Conditions Limit the Accuracy of Quantitative Computed Tomography-Based Finite Element Models of Vertebral Failure', *J Biomech Eng*, vol. 140, no. 2, pp. 0210041–02100411, Feb. 2018, doi: 10.1115/1.4038609.
[37] M. Sutton, C. Mingqi, W. Peters, Y. Chao, and S. McNeill, 'Application of an optimized digital correlation method to planar deformation analysis', *Image and Vision Computing*, vol. 4, no. 3, pp. 143–150, Aug. 1986, doi: 10.1016/0262-8856(86)90057-0.
[38] L. Liu and E. F. Morgan, 'Accuracy and precision of digital volume correlation in quantifying displacements and strains in trabecular bone', *Journal of Biomechanics*, vol. 40, no. 15, pp. 3516–3520, Jan. 2007, doi: 10.1016/j.jbiomech.2007.04.019.
[39] S. Yaofeng and J. H. L. Pang, 'Study of optimal subset size in digital image correlation of speckle pattern images', *Optics and Lasers in Engineering*, vol. 45, no. 9, pp. 967–974, Sep. 2007, doi: 10.1016/j.optlaseng.2007.01.012.
[40] B. Pan and B. Wang, 'Some recent advances in digital volume correlation', *Optics and Lasers in Engineering*, vol. 135, p. 106189, Dec. 2020, doi: 10.1016/j.optlaseng.2020.106189.